Skolkovo Institute of Science and Technology

FLEXIBILITY CHARACTERIZATION IN POWER SYSTEMS

Doctoral Thesis

by

ALVARO JOSÉ GONZÁLEZ CASTELLANOS

DOCTORAL PROGRAM IN ENGINEERING SYSTEMS

Supervisor
Assistant Professor Aldo Bischi

Co-supervisor
Assistant Professor David Pozo

Moscow - 2021

I hereby declare that the work presented in this thesis was carried out by myself at Skolkovo Institute of Science and Technology, Moscow, except where due acknowledgement is made, and has not been submitted for any other degree.

Alvaro José González Castellanos

Assistant Prof. Aldo Bischi

Abstract

In electric power systems, the requested electricity from loads must be immediately balanced by the generation while maintaining secure network operation. Massive deployment of non-dispatchable renewable energy sources (RES) challenges power systems' operation by adding uncertainty in the generation side, leading to stochastic generation-load imbalances. Increasing RES penetration requires enhancing the power systems' flexibility, viz the ability to balance load and generation changes. There are several alternatives to improve power systems' flexibility, ranging from technological solutions, such as fast generators and storage technologies, to the redesign of electricity markets for the procurement of demand response and generation capacity reserves. It is utterly necessary for modern power systems operation to adequately characterize renewable generation uncertainty and flexibility solutions available for their efficient, secure and reliable operation.

This thesis investigates new mathematical modeling development of three flexibility measures: energy storage units, integration between heat and power sectors, and wholesale electricity markets for energy and balancing provision. Specifically, the original contributions of this thesis are as follows.

First, we provide a novel detailed convex mathematical model for electric energy storage units' operation. We demonstrate that the developed model improves batteries' characterization accuracy while preserving computational tractability through computational test cases against different storage models. The computational studies verify the operational reliability of the storage units, where ideal storage models lead to an 11% mismatch between scheduled and deliverable power.

Second, we propose a market for heat exchange between integrated heat-and-power microgrids. The designed market presents a convex decomposable structure, making it suitable for decentralized microgrids' coordination and dual pricing derivation. We analyze the influence of the microgrids' heat interconnection's efficiency, capacity, and topology on optimal heat exchange and pricing. The presented heat market reduces operational costs and electricity imports from the external network, increasing the microgrids' operational flexibility.

Finally, we generalize the existing chance-constrained energy and reserves market

designs to include the modeling of asymmetric forecast errors of renewable generation. The developed market can reduce demand payments while reflecting the uncertainty introduced by renewable generators in the balancing prices, i.e., renewable generators with worse forecasts have higher balancing prices. The derived energy and balancing prices constitute a competitive equilibrium and provide useful information for investors by reflecting the locations resulting in lower balancing compensation costs.

Thus, the main contribution of this thesis is the development, implementation, and analysis of new mathematical models for capturing flexibility from storage technology assets and new market designs. Computational tractability and economic interpretability are thoughtfully studied.

Publications

Journal Articles

J.2. **A. Gonzalez-Castellanos**, D. Pozo, and A. Bischi, "Detailed Li-ion Battery Operation Model for Day-ahead Economic Dispatch," *International Journal of Electrical Power & Energy Systems*, vol. 116, p. 105561, Mar. 2020.

J.1. **A. Gonzalez-Castellanos**, D. Pozo, and A. Bischi, "Non-ideal Linear Operation Model for Li-ion Batteries," *IEEE Transactions on Power Systems*, vol. 35, no. 1, pp. 672–682, Jan. 2020.

Submitted Journal Articles

S.J.2. **A. Gonzalez-Castellanos**, A. Hinneck, R. Mieth, D. Pozo, and Y. Dvorkin, "Electricity and Reserve Pricing in Chance-Constrained Electricity Markets with Asymmetric Balancing Reserve Policies," submitted to *IEEE Transactions on Power Systems.*

S.J.1. **A. Gonzalez-Castellanos**, and A. Bischi, "Heat market for interconnected multi-energy microgrids: a distributed optimization approach," submitted to *Energy Conversion & Management.*

Book Chapter

BC.1. A. González-Castellanos, D. Pozo, and A. Bischi, "Distribution System Operation with Energy Storage and Renewable Generation Uncertainty," in *Handbook of Optimization in Electric Power Distribution Systems*, M. Resener,S. Rebennack, P. M. Pardalos, and S. Haffner, Eds. Cham: Springer International Publishing, 2020, pp. 183–218.

Conferences (peer reviewed)

C.16. L. López, **A. Gonzalez-Castellanos**, D. Pozo, M. Roozbehani and M. Dahleh, "QuickFlex: a Fast Algorithm for Flexible Region Construction for the TSO-

DSO Coordination," Accepted in *SEST 2021*.

C.15. **A. Gonzalez-Castellanos**, and D. Pozo, "Optimal Scenario Reduction Method for Stochastic Power System Problems," accepted in *PowerTech 2021*.

C.14. A. Poddubny, D. Senchuk, **A. Gonzalez-Castellanos**, and D. Pozo, "Demand Response on the Russian Retail Market," accepted in *PowerTech 2021*.

C.13. K. Bubenchikov, **A. Gonzalez-Castellanos**, and D. Pozo, "Data-driven Inverse Optimization with Application to Dynamic Line Rating in Russian Power Grid," accepted in *PowerTech 2021*.

C.12. O. Oladimeji, **A. Gonzalez-Castellanos**, D. Pozo, Y. Dvorkin, and S. Acharya, "Impact of Electric Vehicle Routing with Stochastic Demand on Grid Operation," accepted in *PowerTech 2021*.

C.11. L. López, **A. Gonzalez-Castellanos**, and D. Pozo, "Empirical Analysis of Capacity Investment Solution in Distribution Grids," accepted in *PowerTech 2021*.

C.10. **A. Gonzalez-Castellanos**, P. Guha Takhurta, and A. Bischi, "Congestion management via increasing integration of electric and thermal energy infrastructures," in *100% Renewable Applied Energy Symposium 2020*, October 29-30, Pisa, Italy, 2020. [Online event]

C.9. **A. Gonzalez-Castellanos**, D. Pozo, and A. Bischi, "Pricing in Integrated Heat and Power Markets," in *MEDPOWER 2020*, Paphos, Cyprus, November 9-12, 2020. [Online event]

C.8. **A. Gonzalez-Castellanos**, D. Pozo, S. Martínez, L. López, and I. Oliveros, "Economic Impact of Wind Generation Penetration in the Colombian Electricity Market," in *MEDPOWER 2020*, Paphos, Cyprus, November 9-12, 2020. [Online event]

C.7. S. Ghimire, **A. Gonzalez-Castellanos**, I. Lukicheva, and D. Pozo, "State Estimation with Identification of Erroneous Network Parameters," in *3rd In-*

ternational Conference on Smart Energy Systems and Technology (SEST2020), Istanbul, Turkey, Sep 7-9, 2020. [Online event]

C.6. L. López, I. Oliveros, **A. Gonzalez-Castellanos**, and D. Pozo, "Distributed Generation Allocation Under Uncertainty," in *IEEE Power and Energy Society General Meeting*, Montreal, Canada, Aug 2-6, 2020. [Online event]

C.5. A. Sangadiev, A. Poddubny, **A. Gonzalez-Castellanos**, and D. Pozo, "Quasi-Newton Methods for Power Flow Calculation," in *2nd International Youth Conference on Radio Electronics, Electrical and Power Engineering (REEPE)*, Moscow, Russia, March 12-14, 2020.

C.4. K. Bubenchikov, **A. Gonzalez-Castellanos**, and D. Pozo, "Benefits of Dynamic Line Rating for the Russian Power Corridor between the European and Siberian Zones," in *2nd International Youth Conference on Radio Electronics, Electrical and Power Engineering (REEPE)*, Moscow, Russia, March 12-14, 2020.

C.3. **A. Gonzalez-Castellanos**, D. Pozo, and A. Bischi, "Stochastic Energy and Reserve Operation for Distribution Power System Operation with Renewable Generation and Non-ideal Energy Storage," in *2nd International Conference on Smart Energy Systems and Technology (SEST2019)*, Porto, Portugal, Sep 9 - 11, 2019.

C.2. **A. Gonzalez-Castellanos**, D. Pozo, and A. Bischi, "A Detailed Li-ion Battery Operation Model for Day-ahead Economic Dispatch," in *11th Mediterranean Conference on Power Generation, Transmission, Distribution and Energy Conversion (MEDPOWER)*, Dubrovnik, Croatia, November 12-15, 2018. *Awarded 3rd place (8/10).*

C.1. A. Grinchenko, **A. Gonzalez-Castellanos**, and A. Bischi, "Stochastic optimization of combined heat and power units: industrial facility in Russian Federation ," in *ECOS 2018 - the 31st International Conference on Efficiency, Cost, Optimization, Simulation and Environmental Impact of Energy Systems*, Guimarães, Portugal, June 17-22, 2018.

Acknowledgments

Firstly, I want to present my gratitude to my supervisors Prof. Aldo Bischi and Prof. David Pozo. They have transmitted their love for energy systems research and have been my scientific mentors and friends during this process. From them, I have learned to focus on scientific contributions rather than methodological details.

I would like to express my gratitude to my family, who has been my biggest support: my mother for her unconditional love and pushing me always forward, my father for his advice and being my role model, and Mami Rosa for her loving support. I want to thank my wife Tamara, who has been full of love and encouragement during my studies and many research-related marathons.

I also would like to thank Prof. Yury Dvorkin and Robert Mieth for their instruction in the field of stochastic power markets and for pushing me to increase the quality and formality of my work while also being super fun to collaborate with. My colleagues and friends Anton Hinneck and Luis Lopez, thank you for providing me with new ideas and ways of tackling optimization and computational challenges.

Last but not least, I want to thank the Skoltech Education Department who has been nothing but efficient and supportive during both my Masters and Ph.D. studies in this institute.

Contents

List of Figures

List of Tables

Chapter 1

Introduction

Future energy systems will be integrated among energy sectors, decarbonized, and geographically decentralized [1]. Electric power systems are at the center of the energy sector transformation. They can provide clean and efficient energy supply to the different energy sectors and consumers [2]. Renewable energy generation will provide the means for decarbonizing the heating and transportation sectors, reducing both emissions and operating costs. National governments recognize that the transition towards renewable generation technologies reduces the environmental impact of the energy sector and is also economically competitive with fuel-based generation [3]. The sustainability efforts and policies are supported by the fact that decrease in renewable generation costs are steadily falling to competitive levels [4], leading to an increase of renewable penetration in electric power systems. Consequently, renewable electricity capacity additions have been continuously increasing for the last 20 years [5]. An important benchmark in renewable capacity installation was crossed in 2012, when the worldwide new capacity installation of renewable energy capacity surpassed that of non-renewable generation plants. Since then, the gap between annual renewable capacity installation versus non-renewable technologies continues to widen [6].

Even though the growing use of variable renewable generation[1] provides environmental benefits; it presents challenges to the reliable and secure power system

[1]Renewable energy sources such as impoundment hydropower can have their power output controlled, while sources dependent on weather conditions like solar photovoltaic and wind turbines have variable generation profiles.

operation. Unlike water, gas, and heating utilities, where the supply networks can be used to store the demanded commodity partially, the electric demand must be continuously balanced. Therefore, electricity generation must always match its demand. The stochastic nature of renewable sources requires the availability of resources for load balancing through changes in renewable power generation.

Power system flexibility, defined as the ability to balance variations in the balance between its demand and generation, can cope with some of the abovementioned limitations [7]. Given the variable nature of some renewable energy sources (RES)[2], power systems must balance not only the changes on the users' demand, but also those derived from RES generation. Therefore, a flexible power system is one that balances changes in its net load, i.e., the difference between the users' demand and the RES generation.

Along this line, a general and adequate definition of flexibility is also given by Alizadeh *et al.*: "the ability of a system to deploy its resources to respond to changes in the net load, where the net load is defined as the remaining system load not served by variable generation" [8]. Additionally, Chicco *et al.* define the flexibility in multi-energy systems as "the technical ability of a system to regulate multi-energy supply, demand, and power flow subject to steady-state and dynamic constraints and while operating within predefined/desired boundary regions for certain energy vectors" [9]. This definition extends the electric net load balancing to include the management of the energy flows of the interconnected energy systems through space and time.

In the following sections be present an overview of the flexibility in power systems, the main flexibility masures, and how to measure the flexibility provision of the units in a system.

1.1 Flexibility in power systems: an overview

Given the increasing interest towards renewable energy sources, the International Energy Agency (IEA) was tasked by the 2005 Gleneagles G8 summit to study and provide a report on the necessary measures for the integration of renewable energy

[2]In this thesis we will refer as RES to variable renewable energy sources, unless explicitely stated otherwise.

sources in large scale power systems. The IEA's report titled *"Empowering Variable Renewables – Options for Flexible Electricity Systems"* provides a definition of a flexible power system: *"a flexible electricity system is one that can respond reliably, and rapidly, to large fluctuations in supply and demand"* [7]. The most important factor influencing the need for flexibility in a power system is the supply variations, i.e., variable renewable generation; since the changes in demand have been easier to predict and balance based on decades of industry experience [10].

We must now differenciate the terms of flexibility and reliability in power systems, since these two terms have been used interchangeably in the literature [8]. *Reliability* is a core function of power systems and relates to a system's ability to continuously and adequately supply electrical energy to its users [11]. On the other hand, *flexibility* pertains to a system's ability to respond to changes in net load [8]. Therefore, *flexibility* is a facet of a *reliable* power system's operation.

The RES variability impact can be assessed under the different time frames of interest for the power system, Figure 1.1, which can be classified in the following stages [12]:

- Regulation – seconds: unpredictable fast changes of net load are balanced.
- Balancing – hours: forecast errors on demand and RES generation are balanced.
- Scheduling – days-weeks: net load variability during the different periods of the day is balanced.
- Planning – months-years: the system's generation and network capacity is increased to balance seasonal and interannual changes in demand and RES generation levels. A special case in this stage is that of hydro-scheduling, for which the use of large impoundment hydro power plants is scheduled based on probabilistic information of the future climatological conditions affecting the reservoir levels.

Additionally, the study of power systems flexibility encompasses electric systems of diverse size which can range from the couple of meters (household level) to thou-

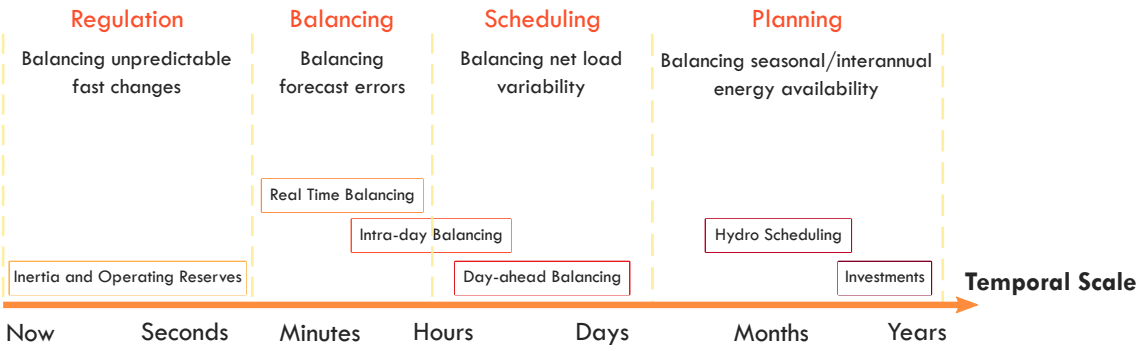

Figure 1.1: Flexibility measures available to power systems

sands of kilometers (continental level). The combination of the spatial and temporal characterization of power systems' flexibility creates a diverse field of problems, i.e., applications, on which it can be analyzed, Figure 1.2.

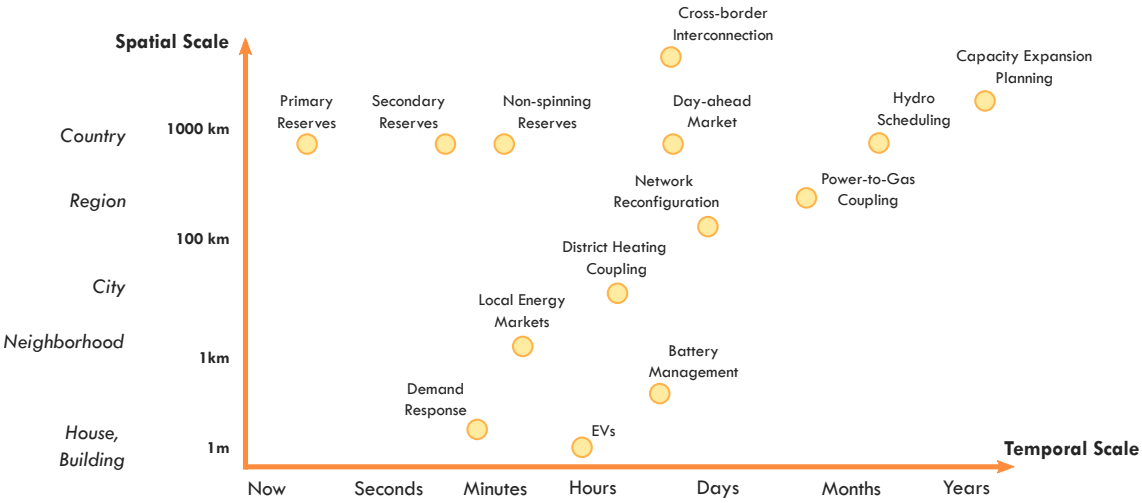

Figure 1.2: Spatio-temporal distribution of flexibility provision

One dimension through which flexibility can be analyzed and quantified is as the maximum change in power, also known as ramp rate, that a system can undergo in a given time frame, e.g., a battery changing its power output in milliseconds, a gas turbine ramping to full capacity in few of minutes, and a coal fired power plant that can ramp up few MWs per hour [10]. Generation plants that have higher ramp rates, i.e., can change their generation output faster, are preferred to balance changes in demand and renewable generation. This is why the faster generation units such as those with gas turbines are favored for load following over steam turbine power

plants, generally coal or nuclear fuelled, which can be used to cover the predicted base load [12]. Additional measures besides generation units can be employed for net load balancing. In the next section we present the main flexibility measures available for electric power systems and their main characteristics for flexibility provision.

1.2 Flexibility measures

For the optimal planning and operation of the power system, the installation and deployment of the available flexibility measures must be done cost-effectively, constrained by the technical limitations of the system [7]. The flexibility of a system can be enhanced by either the separate or combined use of measures, Figure 1.3, related to the use of generation units, electric energy storage, demand management, optimal network management, integration with other energy systems, and efficient market mechanisms; which are described in the following.

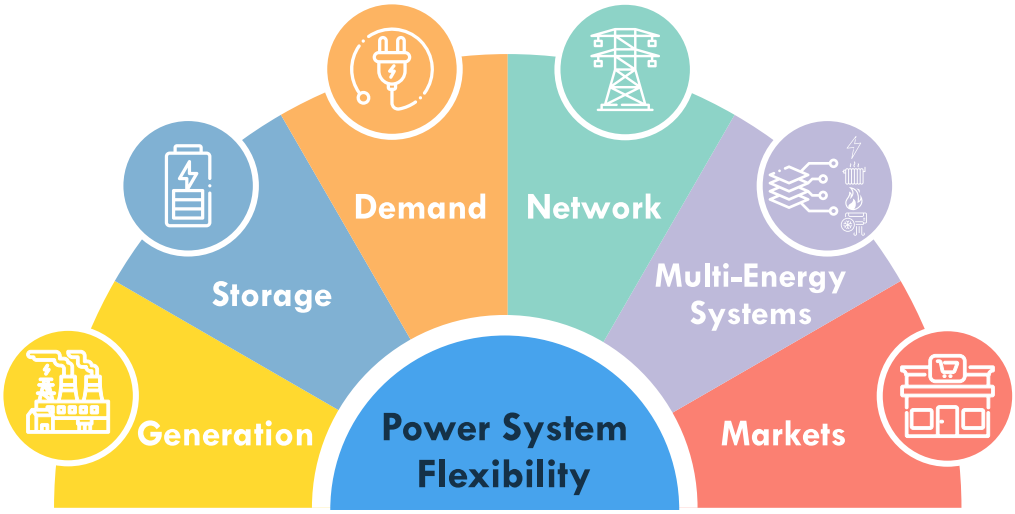

Figure 1.3: Flexibility measures available to power systems

1.2.1 Flexibility from the generation side

Technical flexibility

Electric generation technologies can have a wide array of technical characteristics based on their primary energy sources, underlying thermodynamic and mechanical

processes, and physical components used for power generation. These technical characteristics determine the available flexibility from power generation technologies. In this manner, we present now the main technical characteristics of the generation units related to flexibility provision.

- **Operating range:** based on their generation technology, power plants usually have a technical minimum load for electric power production. The difference between this technical minimum and the maximum generation capacity of the unit constitutes plant's operating range. Greater operating ranges and lower technical minimums allow for higher absorption of RES variability [13].

- **Ramp rates:** the maximum change in power generation, upwards and downwards, over a time range that a unit can undergo is known as the ramp rate [13]. Units with greater ramp rates provide the system with better response to sudden changes in RES production.

- **Startup/shut down times:** power plants require different amounts of time from being completely shutdown to become fully operational, and to perform the shut down process. A plant's startup and shut down times depend on the complexity of its electricity generation technology. The startup and shut down times of a power plant have a high influence on its cycling, i.e., how frequent are its startups during a day to balance load changes [14].

- **Minimum up and down times:** fuel-based generation units have a characteristic time in which it cannot be turned off once started, and one that restricts its switching on after a shut down process is completed [15]. Smaller minimum up and down times allow for the more frequent use of a generation unit to balance RES variability [13].

- **Fuel flexibility:** in fuel-based generation units, the aforementioned technical characteristics depend on the type of prime mover and its primary energy source, i.e., fuel. Therefore, in the selection of power plants for capacity installation, it is necessary to establish the type of fuel employed based on the system's flexibility requirements, such as maximum ramping [16]. Additionally,

some generation technologies allow, up to certain degree, for the combination of fuels, modifying the plant's technical characteristics, e.g., the blending of hydrogen with natural gas [17].

Scheduling flexibility

Generation units have their participation in the load-balancing dispatch based on their technical and economic characteristics [14]. For the flexible operation of a power system it is necessary to consider over a sufficiently long horizon: i) the marginal cost of generation, ii) startup and shut down costs, and iii) minimum operation times [18]. Units with higher startup costs and times are usually used to cover the system's base load for the entirety of the day, e.g., nuclear and coal power plants. Plants with low startup costs are employed for load-following, i.e., to switch on/off based on small demand variations. An example of load-following generation is hydropower. Finally, when demand peaks occur with higher ramping rates, more flexible generation units are employed, e.g., combustion engines.

1.2.2 Flexibility from electric energy storage

Electric energy storage can provide load balancing services to the power system by storing the excess energy produced by the RES, and by discharging its stored energy when there is a decrease in the RES output. Given the large variety of energy storage technologies, they can provide multiple services to the electric system based on their technical characteristics, ranging from instantaneous balancing services (in milliseconds) to seasonal shifting (several months) [19].

1.2.3 Flexibility from the demand side

Demand side management

Since the net demand must be balanced at any time in power grids, it is possible to reduce the generation requirements by adjusting the consumers demand to offset changes in RES, i.e., increase/decrease the demand for higher/lower RES output. For their participation in demand side management, the consumer loads require

controllability from its user, who in turn adjusts the load's demand based on the system operator's requests. Examples of controllable loads are heating, ventilation, and air conditioning (HVAC) systems and energy-intensive industrial processes such as pulp and paper production [20]. Load increase can be applied for valley filling and load growth, whereas demand decrease is applied for peak shaving, and conservation. Additionally, demand can be postponed or advanced through load shifting, i.e., modifying the schedule of a process such as the use of a dishwasher or a step in an assembly line. The modification of the demand could be financially compensated based on agreed contracts or the applicable regulation.

Electric vehicles (EVs)

Considering that EVs can act either as load or generators by changing the charging/discharging regime of their batteries, they can be used to provide short-term balancing to the power network during the hours in which they are idle and connected to a charging station [21]. EV owners can be compensated based on the utilized capacity and type of services provided, e.g., fast charging/discharging or charging interruption. Additionally, the mobile characteristic of electric vehicles could permits their use by system operators as movable batteries that can provide services at different locations in different times of the day.

Buildings' thermal inertia

Electricity consumption in buildings is not limited to powering consumer appliances but also accounts for the controlling of heat, ventilation and air conditioning (HVAC) systems that provide thermal comfort. HVAC systems are operated in a manner that regulates the spaces' temperature and air quality within an established comfort region. The change in temperature and air quality in buildings follows thermal processes defined by the physical characteristics of the HVAC system, the building and its surroundings. Thus, temperature gains/losses in a building are not inmediatly felt after the shut down of the HVAC system. Therefore, the smart connection/disconnection of HVAC systems permits the modification of the building's load, while maintaining the comfort conditions within the predefined boundaries

[22].

1.2.4 Flexibility from the electric network

Electric transmission lines can allow the unlocking of flexibility resources commonly "hidden" by conservative engineering limits and jurisdictional barriers for their operation. Being an investment-intensive resource, power networks require accurate assessment of the flexibility that can be extracted from them, delaying the installation of new lines and transmission equipment.

Dynamic line rating and FACTS devices

Electric energy transmission is performed through insulated conductors ranging from tens of meters to hundreds of kilometers. Each conductor has a rated transmission capacity, amperes (A), based on its thermal characteristics. Traditionally the lines' thermal rating is considered as a constant parameter, based on manufacturer information and the average temperature at the installation site. In reality, the transmission capacity of a power line changes with weather parameters, such as solar radiation, temperature, and wind speed; which, for example, would allow for the transmission of higher amounts of power when higher wind speeds occur [23].

An active approach to increase the power capacity of power lines with the use of Flexible AC Transmission Systems (FACTS). FACTS devices provide reactive power balancing along the power lines, thus reducing the total apparent power transmitted and increasing the active power holding capacity of the lines. Additionally, FACTS devices increase the power controllability of the line flow and and improve the stability of the power networks [24].

Topology reconfiguration

Electric power networks are built based on realibility and security standards that lead to generation and transmission overcapacity. The transmission capacity redundancy leads to higher operating costs due to increased losses in the conductors and the appearance of loop flows. Since the electricity flow through the network

follow Kirchhoff's laws based on the electric properties of the lines and nodal power balances, the electric power system could benefit from controllability of the power flow directions. The reconfiguration of the network topology aids to gain control over the network's power flow directions, and could be performed by changing the online/offline status of a power line, traditionally considered as a fixed parameter in power system operation models [25]. Network topology reconfiguration can thus help reduce network losses and line overloading, clearing the path for the flow of RES power for its greater integration in the load balance and for the more efficient disptach of flexibility measures for net load balancing. In this manner, the use of network reconfiguration in power system management can help improve system efficiency and increase its flexibiity.

Cross-border interconnection

Net load balancing must be achieved for the electric power system as a whole. However, it is possible to diminish the flexibility requirements for an area via its interconnection with adjacent ones [13]. The different load and RES profiles, as well as the flexibility resources, can be shared among the areas for load balancing while providing economic benefits for those that provide flexibility services. An example of large-scale aggregation of balancing areas is the NordPool market, which allows the transmission of cheaper Danish wind generation, balanced by controllable Norwegian hydroelectricity [7].

Analogous to the use of balancing areas, it is possible to increase a system's flexibility via electricity import and export. In the case of importing and exporting, the balancing of the area is not ensured by a centralized controller but instead aided by the transmission of electricity between two systems based on commercial contracts [26]. An example of the use of cross-border interconnection for load balancing is the future European balancing market in which over 40 transmission system operators (TSOs) of 35 countries will be able to exchange balancing services in the intraday market for different types of products, i.e., provision of balancing power with an associated activation time frames [27].

1.2.5 Flexibility from multi-energy systems

Electric power systems can be connected to other energy systems, such as district heating networks through cogeneration units, electric boilers, and heat pumps, district cooling through compression chillers, gas networks for fuel supply to the power plants and via power-to-gas technologies, among others. An multi-energy system is a system where multiple energy carriers can be converted, transported and stored for the supply of users' demand. The increase in the power system's flexibility is achieved through the synergy between the different subsystems and their characteristics, i.e., electricity and gas can be efficiently transmitted over long distances, gas and chemical carriers such as liquid fuels can be cheaply stored, and heating and cooling networks count with thermal inertia, which allows them to act as buffers for slow energy release [28].

Flexibility from thermal networks

Unlike electric power balance which occurs almost instantly, thermal systems have an intrinsic source of inertia in the form of thermal capacity [29]. Sources of inertia in thermal networks can be found in heat/cold carrier fluids, thermal energy storage units, and buildings. With the use of heat generation units linking the electricity and thermal systems, such as cogeneration plants, heat pumps and power-to-heat units, it is possible to transfer the variability of RES to the thermals systems. For example, during periods of high RES production, it is possible to produce more heat and less electricity, allowing the thermal inertia of the system to accumulate the extra heat and release it during hours where the RES is lower and more electricity is needed. Thus, not only increasing the system's flexibility, but also reducing its fuel-related costs and emissions.

Power-to-gas

Synthetic fuel gases, such as hydrogen and methane, can be produced by using the excess electricity generated during high RES periods, to be either locally consumed, transported through the gas network or stored for later consumption [30]. Addition-

ally, the synthetically generated fuel gases can be used to power balancing generation in periods of RES deficit. Due to its compressibility, natural gas pipelines can be used to store gas for its later use by controlling the internal pipeline pressure. Additional synthetic gas could also be injected in periods of excess electric renewable generation. Therefore, gas systems can be operated as temporary primary energy storage to balance net load fluctuations in the power system [31].

Power-to-fuel

An alternative to the conversion of excess RES electricity into gas fuels is its use for producing liquid fuels. Hydrogen produced from excess RES generation can be then converted into liquid hydrocarbons like diesel and gasoline for their use in auxiliary power generation units, transportation and base chemical materials [32]. Thus, providing not only increase flexibility to the electric network during periods of high RES generation, but also reducing the use of fossil fuels and their associated emissions.

1.2.6 Flexibility from markets

Proper electricity markets design can also enhance the flexibility of electric power systems by providing economic incentives to guarantee the capacity availability of flexibility providers. For instance, based on expected net load imbalances, market operators can schedule generation units to provide balancing reserves. The reserves are scheduled as stand-by generation capacity that can be used to balance net load variations. Multiple types of reserves can be then scheduled based on the required response time, prioritizing faster and dispatched generation (spinning reserve) while utilizing slower and offline generators (non-spinning reserve) for imbalance events of significant duration or magnitude.

The role of electricity markets in the flexibility provision is thus that of maximizing the participation of RES generation in the electric dispatch, while minimizing the reserves required for its balancing [33].

1.2.7 Renewable generation curtailment

A last resort option for balancing excess renewable generation is to curtail the RES, i.e., their power output is reduced. RES curtailment usually follows transmission congestion or excess production during periods of low demand. Overinvestement in renewables to meet to renewable penetration and emission goals could lead to excessive use of RES curtailment as a flexibility measure [34]. In this manner, RES curtailment acts as a measure of how inflexible a system is.

1.3 Flexibility quantification

The flexibility contribution of technical measures such as generators, load management and energy storage units can be characterized by their power capacity π in MW, maximum ramp rate ρ in MW/min, energy provision capacity ε in MWh, and ramp duration τ in min [35]. Since the ramp duration can be derived from the selected time horizon and the energy provision capacity, the characterization of a flexibility measure can be performed solely by π, ρ, and ε. Additionally, each flexibility dimension can be set with a minimum and a maximum value. $\pi^{+/-}$ represent the minimum and maximum power generation levels (of negative value if power consumption is present), $\rho^{+/-}$ represent the upward and downward ramp rates, and $\varepsilon^{+/-}$ the maximum energy that a measure can produce (positive) and receive (negative). Based on this flexibility metrics, it is possible to quantify a system's flexibility capability, the flexibility required by a variable resource and event, and the remaining flexibility after the requirements are satisfied [36].

An initial approach for calculating the aggregated flexibility of a system is by a Minkowski sum of its flexibility metrics [36].. The Minkowski sum is calculated by adding component by component the system units' values of both positive and negative . For example, the aggregated system ramps are calculated by

$$\rho^{+}_{\text{total}} = \sum_{g \in \text{Units}} \rho^{+}_{g}, \tag{1.1}$$

$$\rho^{-}_{\text{total}} = \sum_{g \in \text{Units}} \rho^{-}_{g}. \tag{1.2}$$

The Minkowski sum is used analogously for estimating π and ε. By being able to represent the flexibility characteristics of a given measure in a three-dimensional space, it is possible to easily compare the strengths and weaknesses among measures. This type of comparison between a storage and a conventional generation unit is presented in Fig. 1.4. For instance, in the figure it can be seen how the generation unit is more suitable for balancing events that require higher amounts of energy, while the storage unit can provide a faster response, for both up and down ramps.

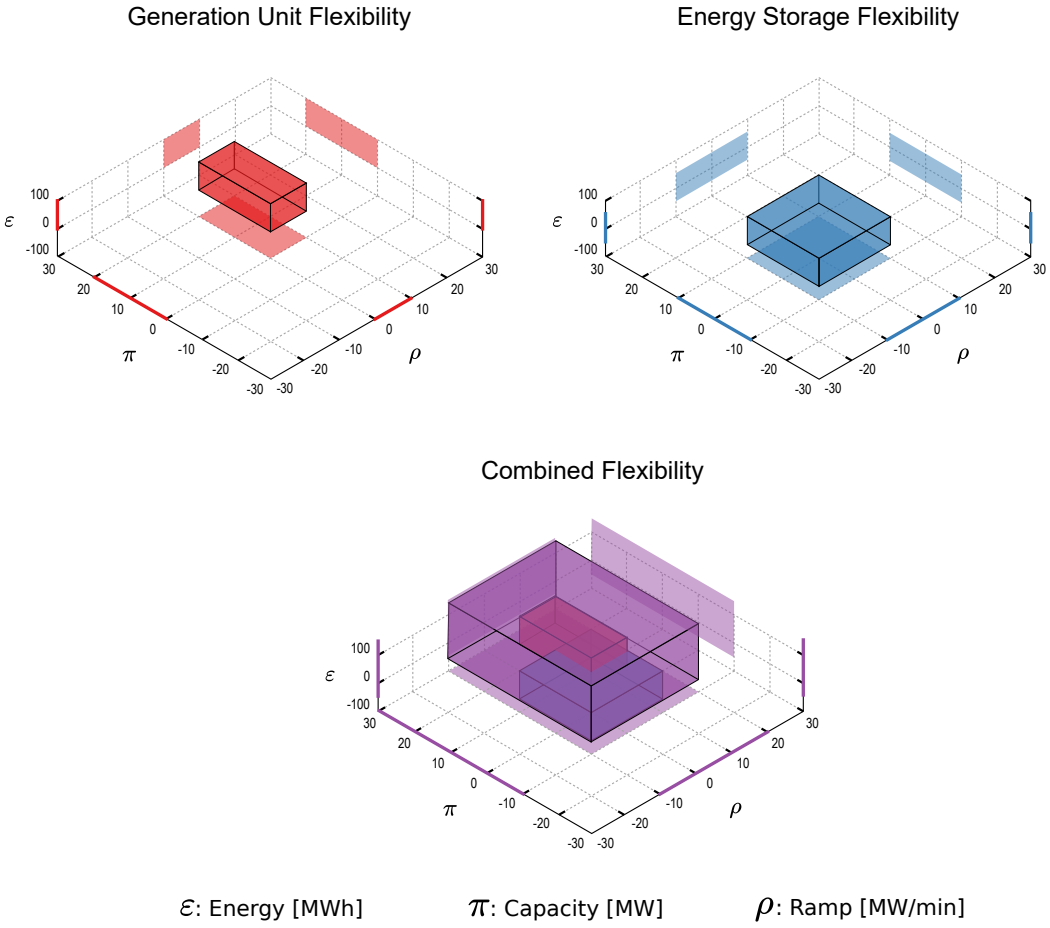

Figure 1.4: Flexibility volumes for a conventional generation unit (red), energy storage unit (blue), and their combined operation (purple).

However, the Mikonswski summ does not consider the effect of the network on the flexibility provision. A steady-state approach for represent the feasible operation of generation units is to represent it through steady-state security regions [37]. In a

steady-state security region each node of the power system has an associated set of active and reactive power injections for which the power flow equations and security constraints are satified. The use of steady-state security regions can be expanded to represent the feasible operating region for flexibility provision by including changes in the system net load, and the energy and ramp capabilities of the installed flexibility measures.

An example for the derivation of the feasible operating region for a generator unit is presented in Figure 1.5[3]. The electric generator is connected by a transmission line to a demand in a generic two-node system as shown in Figure 1.5(a). The generator feasible operating region, highlighted in purple in Figure 1.5(b), is obtained by introducing the limits on the generation output based on the network and generator constraints. The generator capability curve (green) presents the generation limits based on the current and power limits in the electric generator. For this illustrative example a synchronous generator is depicted in Figure 1.5(b). Additionally, a minimum power generation limit can be introduced to represent the technical minimum load for the generator. Steady-state voltage limits (yellow) and the power transmission limit related to the line's thermal capacity (red) relate the generator's output with the satisfaction of the power flow equations and the secure system operation. Finally, the generator's ramp rate (brown) delimits the power decrease of the generation unit based on the current operating point (teal). Note that the generator operating point (teal) indicates higher power generation that that requested by the demand (orange) to account for the losses in the transmission line.

As seen in the example presented in Figure 1.5, the incorporation of the network and generation contraints could have a great impact on the flexibility provision.

1.4 Research gaps and thesis aim

Electric power systems require significant capital investments in flexible and efficient energy technologies for the clean energy transition, as highlighted in the vision for the European energy system by 2050 developed by the European Technology and

[3]The presented limits have been simulated in a tightly constrained system to highlight the effect of network constraints on the generator's feasible operation region.

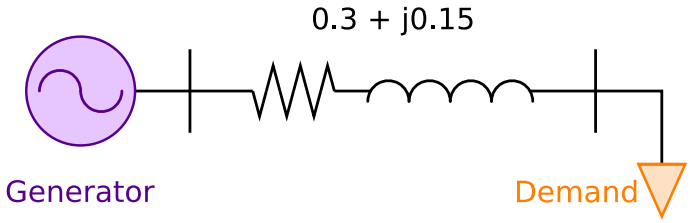

(a) Sample two-node power system.

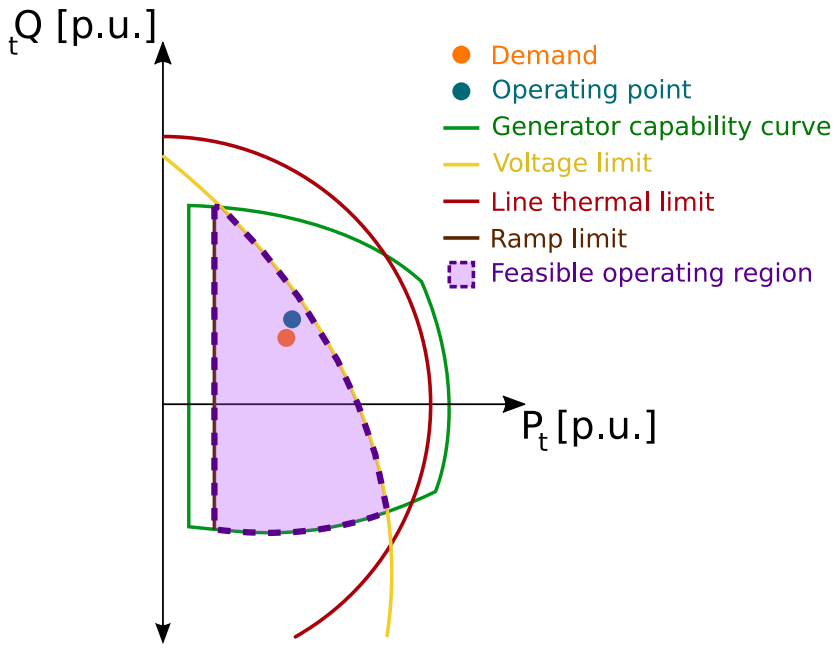

(b) Generator feasible operating region after the application of network limits.

Figure 1.5: Effect of network constraints on flexibility provision: (a) two-node system, and (b) generator feasible operating region.

Innovation Platform for Smart Networks for the Energy Transition (ETIP SNET) [2]. However, such investments are usually misled by improper characterization of the currently available flexibility measures. The proper assessment of the existing technical resources, the efficient coordination with other energy infrastructures, and the creation of market structures with adequate price signals can deter substantial investments in redundant flexible equipment. Therefore, we consider that a better mathematical representation of the technologies, coordination strategies, and markets that affect the flexible electricity supply must be considered for the development and operation of future power systems. This thesis aims to provide mathematical tools for the accurate representation of flexibility measures in electric power systems. In this work, we center our attention on three primary measures to provide

flexibility to future electric power systems: electric energy storage, integration with the heating sector, and bundled energy-and-reserves electricity markets.

We decided to establish as our subject of study the operational flexibility of electric power systems, more specifically, the operational flexibility related to the scheduling of the generation and storage resources in day-ahead dispatch and energy markets, since it is in this time frame where the bulk of the operation scheduling and economic interactions are settled. In this manner, our interest relates to the system operation for fixed intra-day time steps spanning up to weekly time horizons.

The adopted modeling framework is that of convex optimization. The convex optimization framework provides the following benefits for our work:

1. Convex optimization is more computationally efficient that its non-convex counterpart.

2. Unlike non-convex optimization, convex optimization models guarantee the existence of a unique (global) optimal solution. Thus, the obtained results are reproducible on any device and optimization solver.

3. The uniqueness of the optimal solution makes convex models suitable for economic interpretation, since it guarantees the existence of a unique price when using a dual-pricing for market formulations.

4. Finally, convex optimization is the standard methodology employed in most of the electric power systems in the world.

We describe the challenges related to the power system's flexibility facets of electric energy storage, integration with the heating sector, and bundled energy-and-reserves electricity markets in the following sections.

1.4.1 Energy storage for renewable balancing

Energy storage systems (ESS) are an attractive measure for the flexibility enhancement of power systems since they can provide instantaneous load balancing, in the order of milliseconds, preventing the use of slower fuel-based generation [38].

Among the different types of ESS, battery energy storage (BES) is gaining significant interest in the provision of grid support, and load shifting [39]. The advantages of employing BES include their good modular configurability, fast response times, and high energy efficiency, e.g., Li-ion has a cycle of efficiency of 70-95%. BES finds applications in the smoothing of the power fluctuations from renewable energy sources [40], frequency support to low-inertia distributed generators [41], participation in demand response programs [42], fast-charging stations for electric vehicles [43], vehicle-to-grid operation [21], power system restoration [44], among others.

Due to their high energy density, high efficiency, long life cycle, and low maintenance, Li-ion batteries currently dominate the battery storage market with a 55% market share [45]. The increasing deployment of electric vehicles and battery systems has led to a rapid decrease in Li-ion battery pack prices, falling about 85% from 2010 to 2020, reaching a volume-weighted average of 176 $/kWh [46]. The quick adoption of Li-ion batteries makes them a representative technology for analyzing the characterization of BES, which can be subsequently adapted to other technologies.

The fast response of BES increases the power system's reliability [47]. However, it is necessary to accurately model their operation to efficiently quantify the flexibility they can provide to the electric network. This analysis is necessary since their efficiency and maximum power delivery change depending on the stored energy [48]. In this thesis, we propose a new model for Li-ion battery systems that increases the characterization accuracy of their efficiency and power limits for their use in power systems operational problems. The proposed model provides a better representation of the flexibility provided by electric energy storage units while remaining computationally tractable.

1.4.2 Coordinated operation of integrated heat–and–power systems

The operational integration of energy systems allows increasing flexibility through the use of existing synergies [49]. The most studied integration is that between

electric and heating networks, given that the use of cogeneration units, electric boilers, and heat pumps in district heating systems links the heat and electricity systems [50]. The coordinated operation of the heat and power systems enhances the electric flexibility by: i) providing supply redundancy in the heating sector with power-to-heat devices, ii) storing excess renewable generation as thermal energy in thermal energy storage devices and district heating pipelines [51], and iii) decoupling generation and demand with the use of the thermal inertia, e.g., by pre-heating the network [52].

To properly exploit the flexibility gained from the integration of heat and power systems, it is necessary to provide economic stimuli for their efficient coordination beyond the possibility of selling back to the electric network the unused electric energy generated from cogeneration units. From a market perspective, the integration of heat and electricity systems has been analyzed through dispatch coordination [53, 54], energy trading [55], and in entirely integrated markets [56, 57]. These works proposed market and coordination mechanisms to trade both electricity and heat within integrated heat-and-power systems. Additional works have developed operational models that would allow the trading of electricity between integrated heat-and-power microgrids [58]. However, the exciting possibility of heat exchange between microgrids for flexibility enhancement has yet to be adequately analyzed in the power systems literature.

The thermal interconnection of microgrids' heating networks has been studied for its ability to reduce operational costs by increasing the revenue of industrial sites that could transfer their high-temperature waste heat to others that require extra capacity to fulfill their peak loads [59]. The heat exchange between microgrids could reduce their operation costs, deter the installation of additional heating capacity that would otherwise be under-used, and liberate cogeneration and storage units to provide electric flexibility. The optimal coordination of heat exchange between microgrids has been studied for both the operation and planning stages [60, 61]. However, to increase the attractiveness of such coordination schemes between microgrids, it is necessary to establish a framework that minimizes participants' costs, establishes fair pricing of the exchanged energy, and preserves their independent

operation and privacy. This thesis investigates the economic interaction of integrated heat-and-power microgrids participating in a heat exchange market. For this purpose, we formulate a market design based on convex optimization suitable for decentralized microgrids coordination. Based on the developed formulation, we analyze the effect of interconnection capacity, efficiency, and topology on heat exchange and price formation.

1.4.3 Market design for power systems with high RES penetration

Not all aspects of flexibility provision are technical. A flexible power system must only count on the technical resources necessary to overcome load imbalances, but also it must ensure the *reliable* deployment of those flexibility measures. Electric markets can and do generate financial incentives for the availability and use of generation and demand resources as flexibility measures. These types of incentives are evidenced in power markets for reserves and balancing services. Balancing markets allocate explicitly and implicitly resources for load balancing. Based on forecasted load imbalances determined using stochastic and security studies, a portion of the generation capacity is committed to providing balancing services to the system [62, 63].

A common explicit and suboptimal approach for the commitment of automatic generation reserve are to set a fixed fraction of the generators' capacity as in the Italian market, where participant generators are required to be available to provide frequency containment reserve of at least ±1.5% (upwards/downward) of their capacity [64], or to determine the system reserve based on security criteria such as the N-1 as in the Colombian system where the reserve capacity corresponds to the maximum value between 5% of the hourly demand and the largest available generation capacity [65]. In this type of market design, with fixed reserves levels, balancing payments are typically made based on generation bids. The explicit determination of reserve requirements can be inefficient since it under-dispatches a more efficient generation to provide balancing services that may not require the entirety of the

reserved capacity. Additionally, the price paid for reserves' provision does not reflect additional costs incurred by the renewable generation balancing. Therefore, the revenue paid out in the energy market will be unrelated to the planning reserves, and could not guarantee revenue sufficiency [66].

Stochastic information of renewable generation can be considered for determining ex-ante the flexibility requirements at the different regulation intervals to be explicitly represented in the markets [62]. Another approach is to implicitly characterize the stochastic nature of the renewable generation in the bundled dispatch of energy and balancing provision in the wholesale electricity markets. Thus, energy and reserves are jointly optimized. The implicit representation of reserves in the market clearing process reduces the costs during real-time operation [63]. Common approaches for the representation of renewable stochastic information in reserves markets include the uncertainty representation by stochastic scenarios [67], the use of worst-case scenario approaches via robust optimization [68], and the use of probabilistic constraints for the risk-aware fulfillment of reserve requirements [69]. The use of risk-aware probabilistic constraints, i.e., chance constraints, provides an efficient convex approach for determining reserve levels while reflecting the risk profile of the systems operator [70]. The main drawback of the existing chance-constrained market formulations is their representation of renewable forecast errors as symmetric and system-wide Gaussian errors, i.e., the considered forecasted errors are summed for the entire system and are represented by a normal distribution [71, 72]. The normality assumption misrepresents the empirical measurements by system operators that reflect the tendency of asymmetry of forecast errors [73], resulting in the overestimation of the required reserves by following symmetric balancing provision policies. Additionally, the aggregation of forecast errors as a balancing requirement on the system level and its consequent unique price obscures the correlation between the uncertainty sources, leading to an inefficient allocation of balancing reserves. Electricity markets must provide proper reserves and balancing price signals to: i) accurately represent the uncertainty introduced by the renewable energy sources, ii) optimize the allocation of flexible balancing resources, and iii) indicate the best location for installing future renewable generation projects. Thus,

traditional Gaussian-system-wide approaches for balancing scheduling fall short in optimizing the levels and costs of reserve provision.

This thesis presents a stochastic electricity market design for the better representation of renewable generation uncertainty and the determination of generation balancing services. The proposed energy and balancing market extends the characterization of renewable generation to include asymmetrically estimated and empirical forecast distributions, providing asymmetrical and nodal generation balancing.

1.5 Thesis Objectives

The general objective of this thesis is to provide an enhanced characterization of flexibility measures available to electric power systems.

The specific objectives of this thesis are the following:

1. To develop a detailed characterization model of electric energy storage devices that increases the representation accuracy of their operation performance while being computationally efficient.

2. To provide a market design that allows the exchange of heat between thermal networks, providing the efficient pricing of the transferred heat and preserving the operational independence and privacy of its participants.

3. To formulate an energy and reserves market to represent and balance asymmetric errors in forecasted renewable generation.

1.6 Thesis Structure

This thesis is organized into four additional chapters. An independent nomenclature to describe the extensive mathematical expressions and formulated models is presented in each chapter. Additionally, the structure of each chapter allows for its self-contained reading and understanding. The structure of the remaining chapter is outlined as follows:

Chapter 2 develops a linear programming characterization model for Lithium-ion battery storage systems. The model allows representing non-constant battery efficiencies and power limits. First, we present an equivalent circuit representation for the electrochemical behavior of Li-ion batteries. We then introduce a detailed linear model extended from the described equivalent circuit for the state-dependent charge and discharge processes of Li-ion batteries based on the characterization of battery efficiencies and power limits. Lastly, we integrate our proposed Li-ion battery model in both a day-ahead economic dispatch and a stochastic unit commitment to illustrate the benefits of a detailed linear battery model compared to existing literature models.

Chapter 3 proposes a market design for the heat transfer between integrated heat-and-power microgrids. Motivated by the increasing integration of heat and electricity energy sectors, we present a basic market structure for exchanging heat between sites, which reduces operational costs, improves operational flexibility, and increases generation usage. The proposed market structure can be managed in both a centralized and decentralized manner, preserving the independence and privacy of the participating microgrids. We provide an analysis of the formation of the heat transfer price and its dependency on the technical interconnection features affecting its value. The market is formulated as a convex model, whose decomposition into a decentralized optimization approach is presented and guaranteed to achieve optimal convergence.

Chapter 4 introduces in chance-constrained energy and reserves electricity markets the concept of asymmetric balancing provision to renewable generation imbalances. Electricity markets must optimize the generation dispatch, ensuring that the dispatched generation can absorb deviations from renewable generation forecasts. Unlike the existing literature, we propose a market design that allows the differentiated generation response to both positive and negative forecast deviation for renewable generation, i.e., for both surplus and deficit generation. The developed market structure reduces consumers' payments, showing more significant savings for systems with high renewable penetration.

Chapter 5 presents the thesis' conclusions, discussion and recommendation for

future research.

Appendix B describes the stochastic unit commitment model with renewable generation and energy storage for the second case study in Chapter 2.

Appendix C derives the expected generation costs under the asymmetric balancing framework developed in Chapter 4.

1.7 Thesis Contributions

This doctoral thesis contributes to the power system's state of the art by providing new mathematical methods for the flexibility characterization of future power systems with high renewable penetration. In particular, we approach three main flexibility measures in power systems and develop detailed representation models under the framework of convex optimization theory. Below we present the general and specific contributions of this thesis. The general contributions of this thesis are described as the methodological contributions, whereas the specific contributions are described as the steps taken to achieve the general ones.

1.7.1 General Contributions

The general contributions of the doctoral research summarized in this thesis are:

I. We provide a detailed convex characterization model for electric energy storage units. Through computational test cases, we demonstrated that the developed model allows improving the characterization accuracy of non-ideal batteries while preserving computational tractability and ensuring operational feasibility of the resultant scheduling. - Chapter 2

II. We propose a convex and decomposable market design for the heat exchange between integrated heat-and-power microgrids. To the authors best knowledge, this is the first market model that allows the analysis of the price formation for the heat exchange between microgrids. The proposed market and its derived prices result in a competitive equilibrium, resulting in an efficient heat exchange. - Chapter 3

III. We extend the chance-constrained energy and reserves' market design present in the literature to include the modeling and balancing of asymmetric probabilistic forecast errors of renewable generation. The developed asymmetric balancing market reduces both demand payments while reflecting the uncertainty introduced by the renewable generators in the balancing prices, i.e., renewable generators with worse forecasts have higher balancing prices. - Chapter 4

1.7.2 Specific Contributions

The specific contributions of the technical chapters of this thesis are:

Chapter 2

i) Develop a convex detailed model for Li-ion battery characterization: we introduce a convex non-constant efficiency characterization of Li-ion batteries by lifting its operational variables, power, and energy into a three-dimensional space. The introduced linear model allows representing the efficiency changes in the battery operation by using sampling points of its operational region while maintaining its characterization computationally efficient.

ii) Introduce non-constant battery power limits: additionally, to improving the state-dependent efficiency representation, the developed model characterizes the non-constant efficiency, charge and discharge, as a function of the battery's state of charge. The use of state-dependent power limits prevents the overestimation of the battery's flexibility provision. Thus, preventing a shortage of energy delivery during the real-time operation.

Chapter 3

i) Design of a convex heat market between heat-and-power microgrids: we propose the formulation of a convex market that achieves the optimal heat exchange between microgrids while being decomposable for decentralized implementation. By using the properties of the convex coordination market, we derive its heat transfer prices, proving that they constitute a competitive equilibrium,

where each participant maximizes its profits and has no incentive to deviate from the market outcome.

ii) Sensitivity analysis of the key drivers of heat transfer quantities and prices: the analytically derived heat exchange prices are dependent on the interconnection capacity and transfer efficiency. We analyze the effects that the interconnection parameters have on the heat exchange and economic interaction between microgrids.

iii) Presentation of a decentralized model for the heat market: to support the practical implementation of the proposed heat exchange market, we present an equivalent formulation that enables decentralized microgrid coordination with a distributed optimization algorithm. The presented algorithm is based on the alternating direction method of multipliers (ADMM), and unlike the ADMM, it provides optimality guarantees for the coordination of three or more microgrids.

Chapter 4

i) Extension of the chance-constrained power market designs: we propose an energy and reserve market that considers both the asymmetric and node-to-node reserve provision for the balancing of renewable energy sources. The proposed market structure incorporates the probabilistic information characterizing the renewable energy sources and the correlation between their energy generation.

ii) Derivation of efficient energy and reserve prices: we derive analytically the energy and reserve prices paid to the generators. The derived prices are proved to form a competitive equilibrium. Additionally, we obtain the penalty prices that the renewable generators must pay as a function of their introduced forecast error.

iii) Comparison of chance-constrained balancing frameworks: we prove that existing models in the literature represent particulars cases of the presented renewable balancing framework after symmetry in reserve provision and uncertainty

aggregation are assumed. The comparison with the existing framework is employed to draw relations between the symmetric and asymmetric pricing and the node-to-node and system-wide pricing.

THIS PAGE INTENTIONALLY LEFT BLANK

Chapter 2

A Non-Ideal Linear Model for Electric Energy Storage

Currently, the characterization of electric energy storage units used for power system operation and planning models relies on two major assumptions: charge and discharge efficiencies, and power limits are constant and independent of the electric energy storage state of charge; misestimating the available storage flexibility.

This chapter proposes a detailed model for the characterization of steady-state operation of Li-ion batteries in optimization problems. The model characterizes the battery performance, including non-linear charge and discharge power limits and efficiencies, as a function of the state of charge and requested power. We then derive a linear reformulation of the model without introducing binary variables, which achieves high computational efficiency while providing high approximation accuracy. The proposed model characterizes Li-ion batteries' performance and operational limits more accurately than those present in classical ideal models.

The primary contribution of this study is the development of a detailed linear Li-ion battery model for its use in the operation optimization of power systems. This work takes into account the use of energy storage for economic operations in which the time steps considered are in the order of minutes/hours. Therefore the transient characterization of the batteries is assumed negligible. The proposed methodology models the operation limits and efficiencies of Li-ion batteries based on their characteristic charging and discharging curves. These characteristic curves

can be obtained based on either computational simulations or by direct measurements, which allows the proposed model to be adapted to different energy storage technologies and updated when new simulated/measured data is available.

The contents of this chapter are partially based on a paper published in the *IEEE Transactions on Power Systems* [74] and a chapter published in the book *Handbook of Optimization in Electric Power Distribution Systems* [75].

This chapter is organized as follows. Section 2.2 presents an equivalent circuit representation for the electrochemical behavior of Li-ion batteries, inspired by the work of *Berrueta et al.* [76]. In Section 2.3 we introduce a detailed non-linear model extended from the described equivalent circuit for the state-dependent charge and discharge processes of Li-ion batteries based on the characterization of battery efficiencies and power limits. Thirdly, in Section 2.4, we propose a linear approach for battery operation by defining the convex curves of detailed non-linear battery models. Lastly, Section 2.5 and 2.6 respectively integrate our proposed Li-ion battery model into a day-ahead economic dispatch and stochastic unit commitment, illustrating the benefits of a detailed linear battery model compared with: the non-convex formulation of Section 2.2, existing ideal model approaches (see, e.g., [77]), and the approximation of non-convex curves through piecewise linearization based on mixed-integer programming. The computational and reliability benefits of implementing the developed model are also quantified. We observed approximately 12% of energy mismatches between schedules that use an ideal model versus those that use our proposed battery model.

Nomenclature

The mathematical symbols used in this chapter are described in the table below. Given that there are several optimization models presented in this chapter with similar variables, the variables are listed next to their corresponding models.

Indexes

g	Generation unit.
l	Power line.

n	Power node.	
t	Time step.	
j, k	Indexes for characterization sample sets J and K.	

Parameters

A_k	Interaction parameters for Redlich-Kister equation	$[\mathrm{J}\cdot \mathrm{mol}^{-1}]$
A_{nl}	Line-to-node incidence matrix	
A_{SEI}	Area of solid-electrolyte interface	$[\mathrm{m}^2]$
C	Cost	[\$/Wh]
$\chi_{and/ctd}$	Anode/catode molar fraction	
Δ	Size of time step	[h]
$\underline{\delta}/\overline{\delta}$	Minimum/Maximum angle allowed	[rad]
E_{A}	Activation energy	$[\mathrm{kJ}\cdot \mathrm{mol}^{-1}]$
η_c	Coulombic efficiency	
$\eta^{\mathrm{cha/dis}}$	Charge/discharge efficiency	
$\overline{E}$	Battery energy capacity	[Wh]
$\overline{F}$	Maximum power flow	[W]
F	Faraday constant	$[\mathrm{s}\cdot \mathrm{A}\cdot \mathrm{mol}^{-1}]$
$\Gamma_{s,n}$	Battery-to-node incidence matrix	
i	Current	[A]
k_0	Reaction rate constant	$[\mathrm{m}\cdot \mathrm{s}^{-1}]$
$\Omega_{g,n}$	Generator-to-node incidence matrix	
P	Power	[W]
$\underline{P}/\overline{P}$	Minimum/maximum power	[W]
R	Gas constant	$[\mathrm{J}\cdot \mathrm{mol}^{-1}\mathrm{K}^{-1}]$
R_{ct}	Charge transfer equivalent resistance	$[\Omega]$
$R_{dif,elec/mem}$	Electrode/Membrane diffusion equivalent resistance	$[\Omega]$
R_{ohm}	Ohmic losses equivalent resistance	$[\Omega]$
SOC	State of charge	[p.u.]
SOC_{sur}	State of charge at electrodes' surface	[p.u.]
T	Temperature	[K]

$U_{bat,0}$	Reference equilibrium potential	[V]
v_{eq}	Equilibrium voltage	[V]
v_{INT}	Non-ideal interaction voltage	[V]
$v_{INT,and/ctd}$	Non-ideal anode/catode interaction voltage	[V]
X_l	Series reactance in the line l	[p.u.]

2.1 Introduction

The need for a secure and flexible operation of electric power systems and the falling prices of batteries has made large-scale Electric Energy Storage (EES) systems a viable and widely studied option. In particular, Li-ion battery systems have gained considerable attention because of their high energy density, power ratings, efficiency, and long lifetime [78]. As an example, in South Italy and South Australia, 40 MW and 100 MW storage systems have been installed, respectively [79, 80]. The introduction of EES, alongside renewable energy generation, compels the development of tools that can manage these systems optimally for maximum grid reliability and profitability [81].

The two major applications of EES that help achieve higher profit potential include frequency regulation and load shifting [82]. Multiple market mechanisms have been proposed for providing services to the power grid from EES: bulk energy storage, vehicle-to-grid (V2G), and distributed battery networks. V2G enables the use of electric vehicles to provide the aforementioned services, in addition to demand shifting via the smart charging of vehicles [21]. Domestic batteries can also be used for grid-scale services through their aggregation [83]. Given the fast response needed for primary frequency control applications (in the range of seconds), battery systems would require the modeling of their dynamic processes. On the other hand, load shifting applications assume steady state behavior, i.e., constant parameters during the operational time steps considered, from minutes to hours.

Battery models can be divided into mathematical, electrochemical, and equivalent circuit [84] models. The first category, *mathematical models*, describes battery behavior based on the state of charge - *SOC* (i.e., the ratio between stored energy

and battery capacity), state of health (the battery's ability to perform in comparison to manufacturer specifications), and other macroscopic properties. Computational methods are used to derive mathematical models with a small number of variables, resulting in low computational costs, but without reflecting the internal processes in the cells, e.g., the changes on the equivalent voltage as a function of the stored energy. The second category, *electrochemical models*, describes the chemical behavior of battery cells based on the physical and chemical processes that occur in the battery cells. Because of their accuracy, electrochemical models can be applied to the optimization of processes that are related to the design of the cell's physical parameters. Additionally, reduced-order electrochemical models allow the accurate modelling of the electrochemical processes in the battery, while providing a computationally efficient storage characterization for online control applications [84]. However, dynamic models are not suitable for their use in optimization applications which require the analysis of large time horizons. The third category, *equivalent circuit models*, provides an equivalent representation of the battery cell based on laboratory measurements. The electric elements in the circuit can be denoted by a combination of linear and exponential models to attune for the dynamic processes in the battery. The resultant circuits provide computationally efficient models, without requiring time-consuming laboratory measurements for the estimation of battery parameters [85].

Vagropoulos et al. developed a linear optimization model for the optimal operation of an electric vehicle aggregator [86]. The model is based on battery charging processes at constant efficiency, which are divided into two stages: constant current and constant voltage charge. *Pandžić* et al., provided piecewise linearized charging limits based on the battery's stored energy levels [87]. Their model is based on a constant-current-constant-voltage charging cycle and validated based on laboratory experiments. The effect of the requested current in storage efficiency is modeled by *Wang et al.* [88]. A concave and monotonically increasing function is provided to represent battery efficiency in terms of deviations from the system's reference current.

A detailed characterization of the loss mechanisms prevalent in both battery and

power electronics is provided by *Schimpe et al.* [78]. An analysis of the efficiency changes as a function of the stored energy level and power request is provided by *Morstyn et al.* [89]. The energy storage system characterization is approximated as a second-order model for its application in model predictive control for distributed microgrids with photovoltaic generation.

Ali et al. developed a methodology for the non-linear estimation of Li-ion battery parameters in an equivalent circuit model [85]. The estimated parameters reflect the dynamic processes by characterizing the elements in the equivalent circuit model as a function of the *SOC*. *Berrueta et al.* developed an equivalent circuit model for a Li-ion battery based on experimental data and the underlying electrochemical phenomena that characterize its performance [76]. The proposed model achieves high accuracy while being computationally simple to implement. Additionally, the model characterizes the battery by the use of its state variables: cell temperature, current, and SOC. An efficiency-based equivalent circuit model has been proposed by *Rampazzo et al.* [90]. The model simulates the battery performance based on the battery state during the operation, as in [76]. A Mixed Integer Linear Programming (MILP) model for representing the behavior of a Li-ion battery pack based on the battery's electrochemical behavior was developed by *Sakti et al.* [48]. In this MILP model, the power limits and battery efficiency are expressed as a function of the *SOC* and the power output. The nonlinearities present in the characterization are addressed through piecewise linearization based on simulated sample points.

2.2 Battery Electrochemical Model

A Li-ion battery reversibly stores electric energy as electrochemical energy. The positive electrode, cathode, of a Li-ion battery is composed of metal oxide materials, usually transition metals, and the negative electrode, anode, is made of graphite. When the battery is being charged, the Li ions flow from the cathode to the anode, where they combine with the incoming electrons and are later stored in the graphite layers [91]. During the discharge process, electrons are transferred from

the battery cell, and the Li ions flow through the electrolyte back to the cathode. After its dynamic processes have stabilized, a Li-ion battery can be represented as an equivalent resistive circuit (Fig. 2.1). The equivalent circuit representation consists of a voltage source associated with the electrochemical equilibrium voltage and three resistors that represent different electrochemical processes: ohmic losses, charge transfer, and membrane diffusion. In this section we describe each of the elements and its correspondence with the underlying electrochemical phenomena based on the experimentally validated model of *Berrueta et al.* [76].

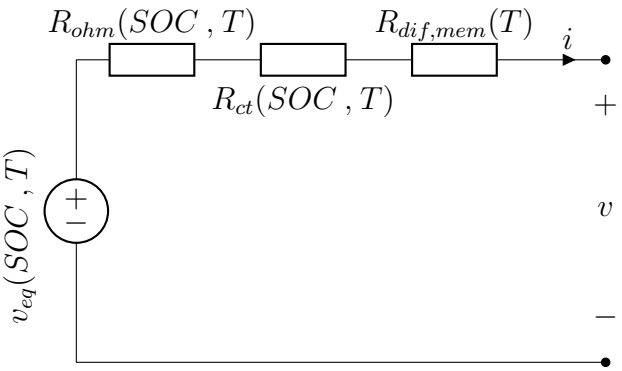

Figure 2.1: Steady-state battery equivalent circuit

2.2.1 Equilibrium voltage

The equilibrium voltage, v_{eq}, indicates the difference in electrochemical potential (voltage) between the electrodes after the charge transfer dynamic processes have reached a steady state. Battery equilibrium voltages can be expressed as a summation of the three processes inside the cell, (2.1). The cell reference potential is defined by $U_{bat,0}$, which indicates the cell potential at standard concentrations. The concentration, i.e., molar fraction χ, of the reactants on the electrodes changes with the amount of stored energy, which is captured by expressions (2.1a) and (2.1b). Therefore, there is a change in the cell potential for nonstandard concentrations obtained by the second term in the summation. The combination of the first two terms gives the Nernst equation for nonstandard conditions (reactions not occurring at $298.15K$, 1 atmosphere, or a cathode and anode molarity of $1.0M$). The third

term, v_{INT}, reflects the non-ideal interactions between Li ions and the host matrix. The non-ideal interactions can be calculated based on a Redlich-Kister polynomial equation of seventh order, (2.1d).

$$v_{\text{eq}}(SOC,T)=U_{\text{bat},0}+\frac{RT}{F}\cdot ln\left(\frac{(1-\chi_{\text{ctd}})\cdot\chi_{\text{and}}}{\chi_{\text{ctd}}\cdot(1-\chi_{\text{and}})}\right)+v_{\text{INT}} \tag{2.1}$$

where

$$\chi_{\text{and}} = 0.083 + 0.917\cdot SOC, \tag{2.1a}$$

$$\chi_{\text{ctd}} = 1 - 0.7\cdot SOC, \tag{2.1b}$$

$$v_{\text{INT}} = v_{\text{INT,ctd}} - v_{\text{INT,and}}, \tag{2.1c}$$

and

$$v_{\text{INT},j}=\sum_{k=1}^{7} A_k\left[(2\chi_j-1)^k-\frac{2\chi_j(k-1)(1-\chi_j)}{(2\chi_j-1)^{2-k}}\right], \qquad j=\text{and, ctd.} \tag{2.1d}$$

2.2.2 Resistive elements

The resistive elements R_{ohm} and R_{ct} indicate fast-dynamic processes. The former is associated with the *ohmic phenomena* that represents the losses related to the movement of electrons and ions during charging and discharging processes; it depends linearly on the SOC and temperature, (2.2). The latter, R_{ct}, models *charge transfer* through the solid-electrolyte interface (SEI), (2.3). The SEI serves as a barrier between the electrodes and the electrolyte solution, preventing their spontaneous reaction (short-circuit) and enabling battery charge reversibility.

$$R_{\text{ohm}}(SOC,T) = R_{\text{ohm},0} + R_{\text{ohm,T}}\cdot T + R_{\text{ohm,SOC}}\cdot SOC \tag{2.2}$$

$$R_{ct}(SOC,T)=\frac{1}{(\chi_{\alpha,and}\cdot\chi_{\alpha,ctd})^{0.5}}\cdot\left[\frac{R\cdot T\cdot e^{E_A/R\cdot T}}{F^2\cdot A_{SEI}\cdot k_0}\right]. \tag{2.3}$$

The last resistive element of the equivalent circuit model is related to the diffusion of Li ions through the membrane. The diffusion process causes a voltage drop in the battery cell and is inversely proportional to the operating temperature (2.4). Similar to the membrane diffusion process, there exists an *electrode diffusion* mechanism

(2.5).

$$R_{dif,mem}(T) = K_{dif,mem} \cdot \exp\left(\frac{b_{dif,mem}}{T - T_{0,dif,mem}}\right) \tag{2.4}$$

$$R_{dif,elec}(T) = K_{dif,elec} \cdot \exp\left(\frac{b_{dif,elec}}{T - T_{0,dif,elec}}\right). \tag{2.5}$$

Changes in the concentration of lithium on the electrodes results in a new perceived state of charge at the cell's electrode surface, SOC_{sur}. The difference between the SOC and SOC_{sur} results in a voltage drop that can be obtained in terms of the electrode diffusion process, (2.6).

$$SOC_{sur} = SOC - R_{dif,elec} \cdot i \cdot \eta_c \tag{2.6}$$

where the coulombic efficiency, η_c, is given by

$$\eta_c = \eta_{c,0} + \eta_{c,T} \cdot T + \eta_{c,i} \cdot i. \tag{2.7}$$

In summary, all of the components present in the equivalent steady-state circuit model depend either on the temperature, T, the state of charge, SOC, the current, i, or a combination of all factors.

For the calculations presented in the following sections, the battery modeled will be that presented in [76], with 40 Ah and 133 V. A constant battery temperature of 25°C will be assumed. The SOC and the current will be considered control variables because they directly relate to the stored energy and the power requested from the battery. The values and the characterization of the battery parameters presented in this section, and used in the rest of the work, can be found in [76].

2.3 Mathematical Battery Characterization

In this section, we present an alternative formulation to the classical ideal battery model used in the operation optimization of power systems (see e.g., [77]) by incorporating features that represent the internal electrochemical processes at the

battery cell level. Consequently, we provide a more accurate description of battery behavior that can be used for power system economic operation. In doing so, charging and discharging power and SOC limits must be derived. However, instead of providing independent limits, as in [77], we derive the limits from internal battery processes. The resulting mathematical battery model is of higher-dimension (more variables are needed), and it is non-linear and non-convex (a non-desired property for power system optimization models). On the other hand, it provides a more accurate mathematical description of the battery that is useful for power system optimization models. In this section, we gradually introduce the model, while in the next section, we propose a convex (linear) approach for the battery model.

2.3.1 Power Limits

The SOC at the electrode surface, SOC_{sur}, is modeled based on (2.6) and (2.7) as:

$$SOC_{sur} = SOC - R_{dif,elec} \cdot i \cdot [\eta_{c,0} + \eta_{c,T} \cdot T + \eta_{c,i} \cdot i], \tag{2.8}$$

where

$$0 \leq SOC_{sur} \leq 1. \tag{2.9}$$

During the discharging process, the state of charge at the electrodes' surface SOC_{sur} decreases; whereas in the charging one, it increases. Therefore the SOC_{sur} lower bound is active during the discharge (but not its upper bound). Similarly, the SOC_{sur} upper bound is active during the charge. The calculation of the discharging limits is then derived as follows

$$0 \leq SOC_{sur}^{\text{cha}}, \tag{2.10}$$

where the maximum discharging current $\overline{I}_0^{\text{dis}}$ is the solution of the equation

$$SOC_{sur}^{\text{cha}}\left(\overline{I}_0^{\text{dis}}\right) = 0. \tag{2.11}$$

We can obtain an explicit solution, in closed form, derived for the maximum discharging and charging current, $\overline{I}_0^{\text{dis}}$ and $\overline{I}_0^{\text{cha}}$, from the second-order polynomial resul-

tant of solving (2.11). The maximum discharge current can be obtained by solving the following quadratic expression:

$$0 = a_{dis} \cdot \left(\overline{I}_0^{\text{dis}}\right)^2 + b_{dis} \cdot \overline{I}_0^{\text{dis}} + c_{dis}, \tag{2.12}$$

with

$$a_{dis} = -R_{dif,elec} \cdot \eta_{c,i}, \tag{2.12a}$$

$$b_{dis} = -R_{dif,elec}[\eta_{c,0} + \eta_{c,T} \cdot T], \tag{2.12b}$$

$$c_{dis} = SOC. \tag{2.12c}$$

Analogously, by bounding the SOC_{sur} in (2.9) by its upper limit, the maximum charging power can be obtained with the following quadratic expressions:

$$0 = a_{cha} \cdot \left(\overline{I}_0^{\text{cha}}\right)^2 + b_{cha} \cdot \overline{I}_0^{\text{cha}} + c_{cha}, \tag{2.13}$$

with

$$a_{cha} = -R_{dif,elec} \cdot \eta_{c,i}, \tag{2.13a}$$

$$b_{cha} = -R_{dif,elec}[\eta_{c,0} + \eta_{c,T} \cdot T], \tag{2.13b}$$

$$c_{cha} = SOC - 1. \tag{2.13c}$$

The current limits $\overline{I}_0^{\text{cha/dis}}$ refer to the limitations in the charge transfer process. To consider the manufacturer limits which prevent cell damage, the parameter $\overline{I}_{c-rate}^{\text{cha/dis}}$ is introduced. Thus, the maximum permissible current for a battery can be calculated based on $\overline{I}_0^{\text{cha/dis}}$ and $\overline{I}_{c-rate}^{\text{cha/dis}}$ by:

$$\overline{I}^{\text{cha/dis}} = min\{\overline{I}_0^{\text{cha/dis}}, \overline{I}_{c-rate}^{\text{cha/dis}}\}. \tag{2.14}$$

From expressions (2.12)–(2.14), it is now possible to calculate the maximum permissible current as a function of the energy stored. The maximum permissible C-rates for the discharge and charge current, $\overline{I}_{c-rate}^{\text{dis/cha}}$, have been set to $5C$[1] and $1C$ to match the typical manufacturer limits used in [76]. Accordingly, we have plotted the max-

[1] A C-rate of $5C$ indicates 5 times the nominal current for discharging according to typical manufacturer specifications.

imum feasible working points for discharging and charging currents vs. the SOC in Figs 2.2(a) and 2.2(b).

As shown in Fig. 2.2(a) for low SOC, the maximum current for discharging decreases. At low SOC, the internal battery resistance, $R_{tot} = R_{ohm} + R_{ct} + R_{dif,mem}$, increases considerably, decreasing the equivalent voltage, v_{eq}, below zero, which indicates an erroneous sense of battery depletion. This behavior corresponds to the voltage cut-off in the battery cells, which would result in a battery shut down by the management system [92].

The charging current limits deviate from the $1C$ rating for higher values of SOC, which is greater than 0.93, Fig. 2.2(b). The physical limitations for cell charging correspond to a greater rate of voltage rise, when compared with the rate of charge absorption. This results in the saturation of electrochemical cells and an increase in stresses within the cells.

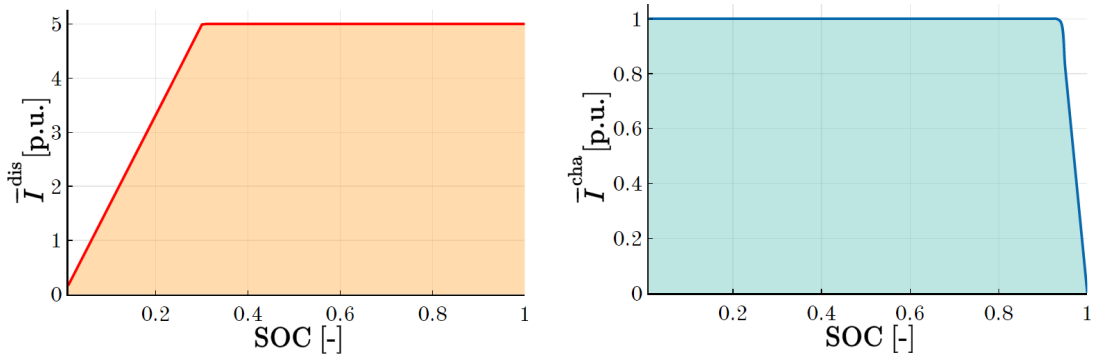

(a) Discharge current (b) Charge current

Figure 2.2: Maximum current normalized to the battery capacity, as a function of the SOC. Shadow areas indicate feasible operation.

The expressions for calculating *discharging power limits* (2.15a), $\overline{P}^{\text{dis}}$, and *charging power limits* (2.15b), $\overline{P}^{\text{cha}}$, are derived using the circuit-equivalent battery model and currents limits.

$$\overline{P}^{\text{dis}} = v_{eq} \cdot \overline{I}^{dis} - \left(\overline{I}^{dis}\right)^2 \cdot R_{tot} \tag{2.15a}$$

$$\overline{P}^{\text{cha}} = v_{eq} \cdot \overline{I}^{cha} + \left(\overline{I}^{cha}\right)^2 \cdot R_{tot}. \tag{2.15b}$$

2.3.2 Charging and Discharging Battery Efficiencies

To characterize battery usage on an operation optimization model, it is necessary to derive an expression for the battery's performance, both for charging and discharging regimes. The battery *discharging efficiency* is given by (2.16). The symbol p^{dis} denotes the power discharged to the electric grid, and so $p^{\text{dis}} = v \cdot i$. The symbol p^{out} denotes outgoing power from the battery cells, $p^{\text{out}} = v_{eq} \cdot i$. Applying Kirchoff's Voltage Law on the circuit in Fig. 2.1, we can derive the discharging efficiency of the battery.

$$\eta^{\text{dis}} = \frac{p^{\text{dis}}}{p^{\text{out}}} = 1 - \frac{i \cdot R_{tot}}{v_{eq}}. \tag{2.16}$$

Similar to discharging efficiency, we can derive a *charging efficiency* expression as follows

$$\eta^{\text{cha}} = \frac{p^{\text{in}}}{p^{\text{cha}}} = \frac{v_{eq}}{v_{eq} + i \cdot R_{tot}}. \tag{2.17}$$

As seen in Fig. 2.3(a) and 2.3(b), the efficiency of a battery improves for higher SOC and C-rates closer to $1C$. This result corresponds to previous experimental analyses performed in [48, 78, 90]. The discharging efficiency lowers for higher current values and low SOC, dropping as much as 33% from its maximum value. The charging efficiency presents a similar behavior, with a smaller efficiency drop correspondent to the smaller operating region, $0 - 1C$.

2.3.3 Non-Linear Battery Model

By considering the aforementioned charging and discharging power limits and efficiencies, we can derive a new detailed battery model that is similar to conventional methodologies [77]. The approach is presented in Model 1. Equations (2.18a) and (2.18b) indicate the discharging and charging power limits. Contrary to conventional models, the limits are SOC-dependent. Equation (2.18c) denotes the energy balance along the time steps. The energy stored in the battery at time t is calculated as the sum of the energy stored in the previous time step $t-1$ and the energy entering the

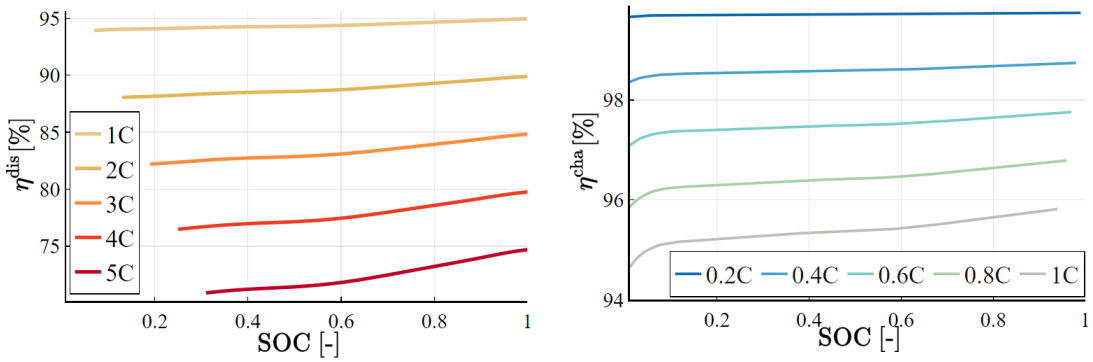

(a) Discharge efficiency (b) Charge efficiency

Figure 2.3: Discharging and charging efficiencies vs. the SOC and discharging and charging power

battery cell in the previous time-step. It is given by the product of $p^{\text{cha}}_{t-1}\eta_{t-1}\Delta$ minus the energy exiting the cell, which is represented by the term $p^{\text{dis}}_{t-1}\frac{1}{\eta^{\text{dis}}_{t-1}}\Delta$. The parameter Δ is the size of time steps as an hourly fraction; employed to transform the use of power into energy. Battery energy capacity limits are described by (2.18d). The battery state of charge, SOC_t, in p.u., is calculated as a function of the stored energy, e_t, by (2.18e). Finally, efficiencies and power limits are included in (2.18f).

Model 1 NLP Li-ion battery model

Variables:

$p^{\text{dis}}_t, p^{\text{cha}}_t$	discharging and charging power	[W]
$\overline{P}^{\text{dis}}_t, \overline{P}^{\text{cha}}_t$	maximum discharging and charging power	[W]
$\eta^{\text{dis}}_t, \eta^{\text{cha}}_t$	discharging and charging efficiency	[–]
e_t, SOC_t	battery energy level (absolute and relative values)	[Wh,–]

Constraints:

$$0 \leq p^{\text{dis}}_t \leq \overline{P}^{\text{dis}}_t, \qquad \forall t \qquad (2.18a)$$

$$0 \leq p^{\text{cha}}_t \leq \overline{P}^{\text{cha}}_t, \qquad \forall t \qquad (2.18b)$$

$$e_t = e_{t-1} + p^{\text{cha}}_{t-1}\eta^{\text{cha}}_{t-1}\Delta - p^{\text{dis}}_{t-1}\frac{1}{\eta^{\text{dis}}_{t-1}}\Delta, \qquad \forall t \qquad (2.18c)$$

$$0 \leq e_t \leq \overline{E}, \qquad \forall t \qquad (2.18d)$$

$$SOC_t = e_t/\overline{E}, \qquad \forall t \qquad (2.18e)$$

$$(2.15) - (2.17). \qquad (2.18f)$$

2.4 Linear Reformulation Approach

In the aforementioned non-linear MODEL 1, non-convexities arise from discharging and charging power limits and efficiencies (2.18f), including bilinear products in the energy balance constraint (2.18c). In this section, we propose a linear approach through a convex envelope for the characterization of battery charge and discharge.

To handle the bilinear products in the battery energy balance equation, we add two new variables, incoming and outgoing power from battery cells, p^{in} and p^{out}, respectively. They are introduced in equations (2.16) and (2.17) and given by:

$$p^{\text{out}} = p^{\text{dis}} \frac{1}{\eta^{\text{dis}}} \tag{2.19a}$$

$$p^{\text{in}} = p^{\text{cha}} \eta^{\text{cha}}. \tag{2.19b}$$

Expressions in (2.19) allow us to define the energy balance equation as an affine function of p^{out} and p^{in}

$$e_t = e_{t-1} + p^{\text{in}}_{t-1}\Delta - p^{\text{out}}_{t-1}\Delta. \tag{2.20}$$

This substitution can be done without the need for evaluating the bilinear products of (2.19) because η^{out} is dependent on the power provided by the battery, p^{dis}, and the SOC, e.g. a function of i and v_{eq}, see (2.16). Therefore, the values of p^{out} can be obtained in terms of p^{dis} and SOC, which are the variables of interest in operation models implementing electric energy storage through batteries.

The outgoing power from the battery cells, p^{out}, can be approximated by a convex combination of sampling points. That is, we can construct a polyhedral envelope of the p^{out} by sampling from the model given in Section 2.2, or alternatively, by experiments like in [76]. Therefore, for every tuple $[p^{\text{dis}}, SOC, p^{\text{out}}]^\top$, we draw J samples through simulations, represented by $[\widehat{P}^{\text{dis}}_j, \widehat{SOC}_j, \widehat{P}^{\text{out}}_j]^\top$. The linear convex envelope is formulated in (2.21). A 3-dimensional representation of p^{dis} vs. SOC and p^{out} is presented in Fig. 2.4(a), where the solid areas indicate the simulated values based on Eq. (2.19a). The sampled points $j \in J$ are highlighted as black dots, and the convex envelope connecting the sampled points is shown by the connecting lines

between the points. As it can be observed, the proposed approach based on the convex envelope for a feasible set points is very close to the non-linear mathematical definition.

$$p^{\text{out}} = \sum_j \widehat{P}_j^{\text{out}} \cdot x_j \tag{2.21a}$$

$$p^{\text{dis}} = \sum_j \widehat{P}_j^{\text{dis}} \cdot x_j \tag{2.21b}$$

$$SOC = \sum_j \widehat{SOC}_j \cdot x_j \tag{2.21c}$$

$$1 = \sum_j x_j \tag{2.21d}$$

$$0 \leq x_j, \qquad \forall j \in J. \tag{2.21e}$$

Analogously, p^{in} can be approached by the convex envelope defined in (2.22). Similarly, it is also compared with the non-linear definition in Fig. 2.4(b).

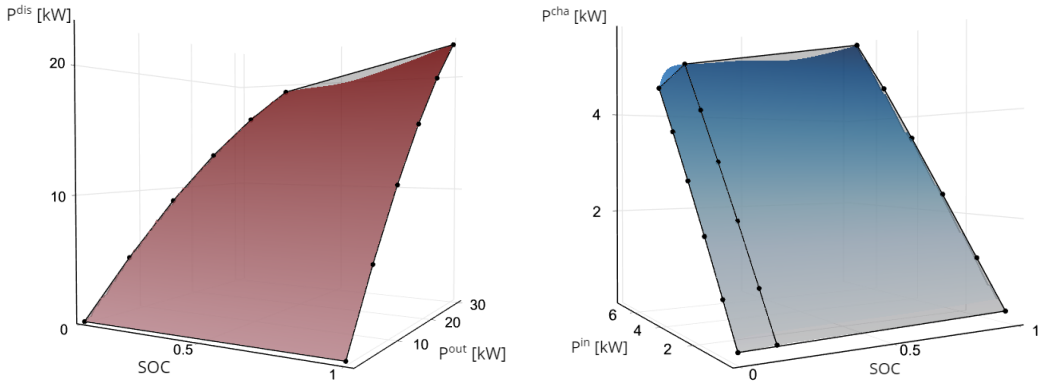

(a) Discharging power (b) Charging power

Figure 2.4: Operating region of Li-ion battery in variable space of (a) $[p^{\text{dis}}, SOC, p^{\text{out}}]^\top$, and (b) $[p^{\text{cha}}, SOC, p^{\text{in}}]^\top$. The curve indicates non-linear dependence, black dots denote sampled points, and the lines between the sampled points define the convex envelope of the sampled points.

$$p^{\text{in}} = \sum_k \widehat{P}_k^{\text{in}} y_k \tag{2.22a}$$

$$p^{\text{cha}} = \sum_k \widehat{P}_k^{\text{cha}} y_k \tag{2.22b}$$

$$SOC = \sum_k \widehat{SOC}_k y_k \tag{2.22c}$$

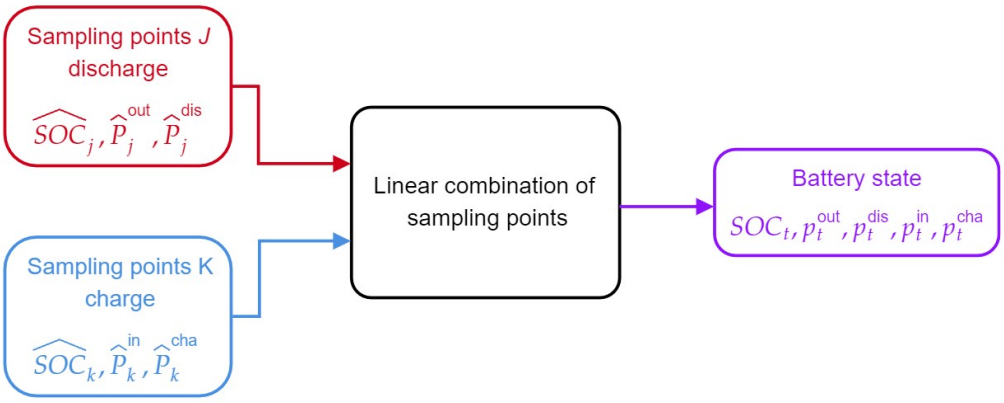

Figure 2.5: Block diagram representing the proposed battery characterization model.

$$1 = \sum_k y_k \tag{2.22d}$$

$$0 \leq y_k, \qquad \forall k \in K. \tag{2.22e}$$

The expressions for battery characterization are given as a function of the SOC as a consequence of the dependence of the v_{eq} and power limits on it, including the computational advantages of employing a normalized parameter. The resultant linear model for battery characterization is presented in Model 2and represented in Fig. 2.5. As seen in Figure 2.5, the proposed battery characterization model receives as an input the sampling point for the discharging and charging processes derived from the employed exact battery model and by their linear combination, derives the battery power and energy state.

The SOC is characterized by (2.21c) and (2.22c). If both expressions were jointly considered, the battery would appear to be charging and discharging at the same time. This corresponds to the fact that to guarantee an approximation through a convex combination of sampling points, constraints (2.21d) and (2.22d) require that at least one x_j and one y_j be greater than zero, simultaneously making p^{dis} and p^{cha} non zero. In Model 1, this does not occur because the energy balance, (2.18c), uses efficiencies η^{dis} and η^{cha} that are lower than one. Therefore, simultaneously charging and discharging would go against the economic objective of minimizing the cost of power system operations because energy would be lost during the imperfect (and simultaneous) charge and discharge processes. This behavior is ensured for a majority of power system applications where the power balance constraints can be satisfied

within the technical limits of the generators and demand, i.e., when the demand can be fulfilled without recurring load shedding or generation curtailment. An exception to this case is when there exist economic incentives for the use of a particular type of generation, e.g., renewable energy generation, or when the cost of simultaneous changing/discharging losses are too small in comparison to the total system costs. If simultaneous charging and discharging is possible in the storage application, the proposed method could be combined with the use of a binary variable to represent the state of the battery, i.e., charging or discharging.

Based on convex combination constraints and the economic use of the battery, constraints (2.21c) and (2.22c) can be combined through a summation in (2.23f). For this constraint to allow a discernment of the charging and discharging processes without the introduction of binary variables, an additional condition is introduced: each sampling set must have at least two sampling points equal to $[0,0,0]^\top$ and $[1,0,0]^\top$; which respectively represent the cases when the battery is not active $p=0$, but is fully discharged or fully charged. Consequently, for a discharge $p^{\text{dis}} > 0$, $x_{j_0} = 0$ and then $p^{\text{cha}} = 0$, since $y_{j_0} = 1$; an analogous relationship would follow for the charging cycle.

For the considered discharging convex approximation by our proposed method we have a maximum approximation error of 9.03%, a mean error of 1.21%, and a standard deviation of 1.39%, when 14 sampling points are considered. For the charging process sampled with 20 points, we have a maximum approximation error is of 1.12%, with a mean error of 0.22% and a standard deviation of 0.18%. The greater approximation error for the discharging curve can be explained by the greater changes in current that the sampling points in the y-axis (6 points for both the charge and discharge) must approximate, when compared to the charging range.

2.5 Test Case 1: Network-Constrained Economic Dispatch

To evaluate the effect of the proposed characterization on battery operation, we compare four energy storage models under a network-constrained economic dispatch.

The following storage modeling approaches were compared:

- CASE NLP: the storage systems is modeled as described in MODEL 1, resulting a non-linear non-convex (NLP) problem.
- CASE LP–IDEAL: an ideal battery was considered, i.e., MODEL 1 is employed, but the parameters $\overline{P}^{\text{cha}}$, $\overline{P}^{\text{dis}}$, η_t^{cha}, and η_t^{dis} were assumed to be constant.
- CASE LP–APPROX: the battery is modeled as described in MODEL 2, employing a convex piecewise linearization of its characteristic curve.
- CASE MILP: for the representation of the non-convex nature of the characteristic curves, Fig. 2.4, a piecewise linearization using binary variables is employed [93]. The resultant model is a mixed-integer linear programming (MILP) one and is presnted in Appendix A.

A conventional economic dispatch, based on a lossless DC approximation, with linear costs is modeled by MODEL 3. The scheduled cost of energy generation is given by (2.24). Equation (2.24a) represents the power balance at every node n of the system for every time step. The power entering the node from each connected line, f_{lt}, is equal to the nodal demand, P_{nt}^{D}, minus the power generated at the node, p_{gt}, minus the discharging power of the battery connected to this node, p_{st}^{dis}, plus its charging power, p_{st}^{cha}. The power flowing in line l is modeled by (2.24b) using line-to-node incidence matrix, A_{nl}. Equations (2.24c), (2.24d), and (2.24e) establish the technical limits of the generators g, power lines l and voltage angle at node n, respectively. The reference voltage angle is set by (2.24f). Battery energy level at the end of a dispatch horizon is set to be equal to the initial battery energy level (2.24g).

The computational tests were performed using a modified version of the IEEE Reliability Test System (IEEE RTS) [94]. The generator technical data, the line parameters, the load profile, including the battery parameters, are given in the online dataset [95]. The optimization horizon was set to 24 hours, with 10-minute intervals. The load data was scaled to the IEEE RTS system based on the demand data from the Iberian Electricity Market on June 20, 2018 [96]. The simulations are

performed using the modeling software Julia [97], JuMP [71], with Gurobi [98] and IPOpt [99] as solvers. A summary of the characteristics and results of the evaluated cases is provided in Table 2.1. As seen in Table 2.1, the employed battery models result in comparable objective values. However, the selection of different modeling approaches has an impact on the optimization problem structure and its solution time. The non-linear non-convex programming (NLP) model at 231.3 seconds is solved a hundred times slower than its linear counterparts, while the mixed-integer linear programming (MILP) model requires 143.3 seconds for its solution. The fastest model is the ideal linear programming (LP-ideal) one, where the power limits and efficiencies are considered constant. However, as discussed in Section 2.5.2, the reliability of the derived battery scheduling for the LP model is compromised by its assumptions. It must be noted that even though the proposed linear approximation (LP-Approx) model introduces additional variables and linear constraints to represent more accurately the battery performance across it operating region, it provides optimal solutions considerably faster, 3.4 seconds, than the NLP and MILP models.

Table 2.1: Summary of optimization results

	NLP	LP–Ideal	MILP	LP–Approx
Objective value	57 305	57 312	57 307	57 308
Δ [%]	-	0.01	0.01	0.01
Time [s]	231.3	1.2	143.3	3.4
Constraints	10 657	9 937	24 049	10 369
Continuous variables	18 576	11 088	20 592	16 272
Binary variables	-	-	13 824	-

2.5.1 Results

Case NLP- Non-linear programming model

The general non-linear programming (NLP) model, Model 1, has been evaluated to provide a reference for the battery operation. The scheduled battery operation is presented for both charge and discharge in Fig. 2.6(a) and Fig. 2.6(b), respectively. The real maximum charging and discharging power limits have been calculated based

on (2.15a)–(2.15b) and represented by the red dashed line in the figures. Battery usage follows charging cycles for periods of lower demand, to subsequently discharge during higher load request. Power limits for both charge and discharge change throughout the day as a function of the stored energy, as described in Section 2.3.1.

Case LP–Ideal– Ideal battery model

In this case, the battery model is based on [77]. For doing so, we considered Model 1, where power limits and efficiencies have constant values. The current limits, (2.14), are set to 1C and 5C. The voltage at the battery terminals is set constant at the rated value of $133V$. For the ideal battery model, the efficiencies are set to constant values, $\eta_t^{\text{cha}} = 0.972$ and $\eta_t^{\text{dis}} = 0.868$. The constant efficiencies were calculated as the mean of the values given by (2.16) and (2.17).
As a result of the economic dispatch defined in Model 3, the battery was scheduled to charge from and discharge to the network as shown in Fig. 2.6(c) and 2.6(d), respectively. As it can be seen, the scheduled operation of the ideal battery violates the calculated limits during peak charge and discharge.

Case LP–Approx- Proposed linear battery model

The scheduled operation of the proposed model is given in Fig. 2.7(a) and Fig. 2.7(b), characterized by its higher use, i.e., during more time steps. For this battery model, the efficiencies depend on the state of charge and the power request, i.e., higher efficiency for higher SOC and lower power charge/discharge. Consequently, the battery use in this case must balance the power delivered with the efficiency and the system's marginal cost of generation. For this purpose, the battery is used at lower power levels, when compared to the ideal model with constant efficiency, to operate at higher efficiency. This change in scheduling can be observed in more time steps used for charge and discharge. Greater use of the non-ideal battery allows the objective value of this test case to be the same as that obtained for the ideal battery, even though the battery has a varying efficiency.

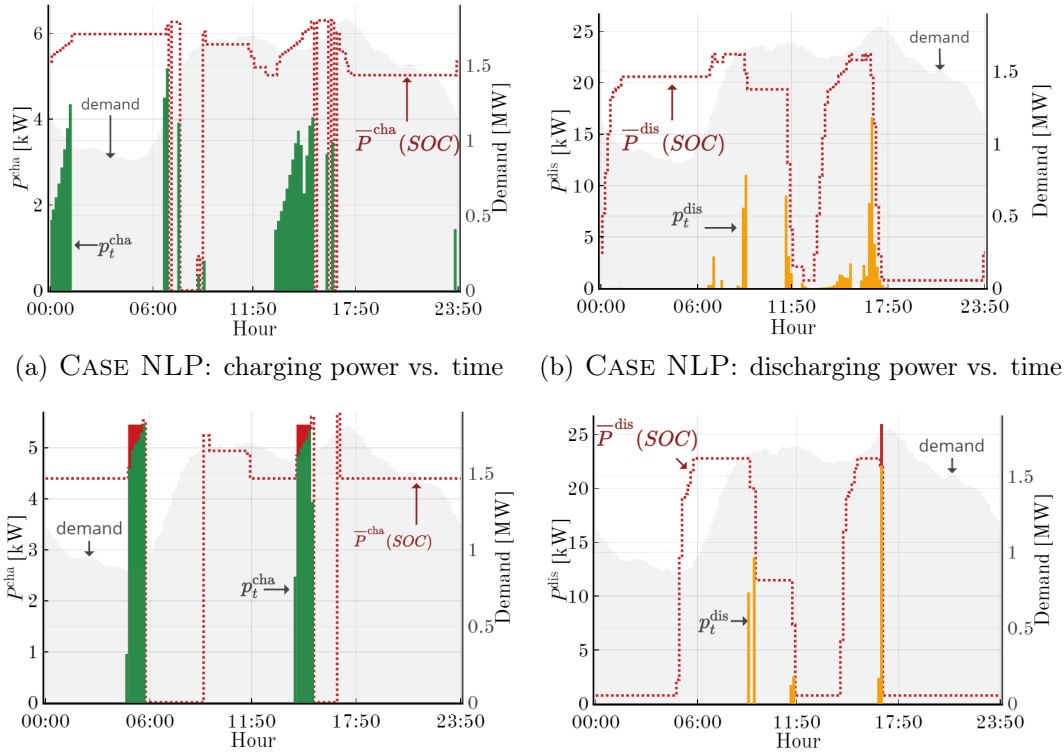

(a) Case NLP: charging power vs. time (b) Case NLP: discharging power vs. time

(c) Case LP–Ideal: charging power vs. time (d) Case LP–Ideal: discharging power vs. time

Figure 2.6: Scheduling of the battery charge and discharge processes for (a)-(b) Case NLP, and (c)-(d) Case LP–Ideal. The dotted line denotes the maximum power as a function of the SOC based on Model 1. The red areas indicate infeasible operation.

Case MILP- Mixed-integer linear programming model

With the aim of comparing the proposed convex model with one that captures the non convexity nature of the battery characteristic curves, a mixed-integer programming model (MILP) has been used to represent the non convex piecewise linearization of the curve through the triangle method [93]. The charging and discharging curves have been each represented with 15 sampling points, taking a base of 5 points for the SOC- and 3 for the $p^{out/cha}$-axis. The higher number of points in the SOC-axis allows a better representation of the power limits as a function of the stored energy.

The results of the MILP model are presented in Fig. 2.7(c) and Fig. 2.7(d). This case employs the battery in two charging and discharging cycle with greater intensity, shorter time of use and higher requested power. The objective value resultant

of the MILP model is the closest one, albeit by a small margin, to that provided by the complete non-convex formulation (NLP). Nonetheless, its computational cost is considerably higher than that of the proposed model, correspondent to the exponential increase of its solution time in relation to the number of binary variables. This makes it unsuitable for real life applications where the amount of batteries and size of the time horizon of interest is considerably larger.

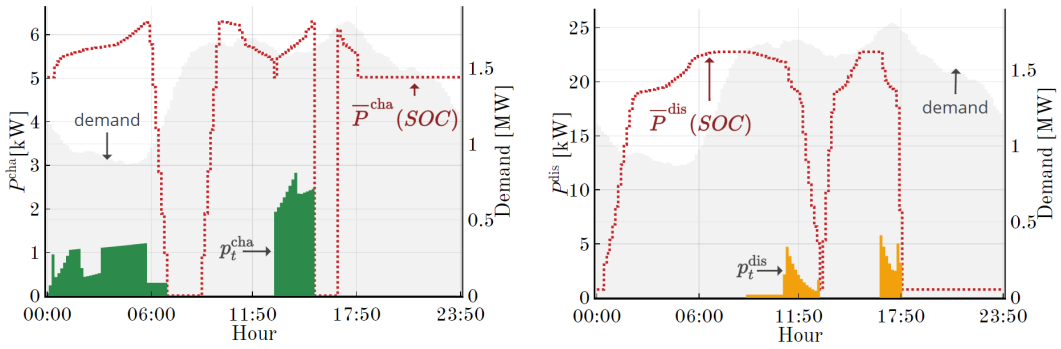

(a) Case LP–Approx: charging power vs. time (b) Case LP–Approx: discharging power vs. time

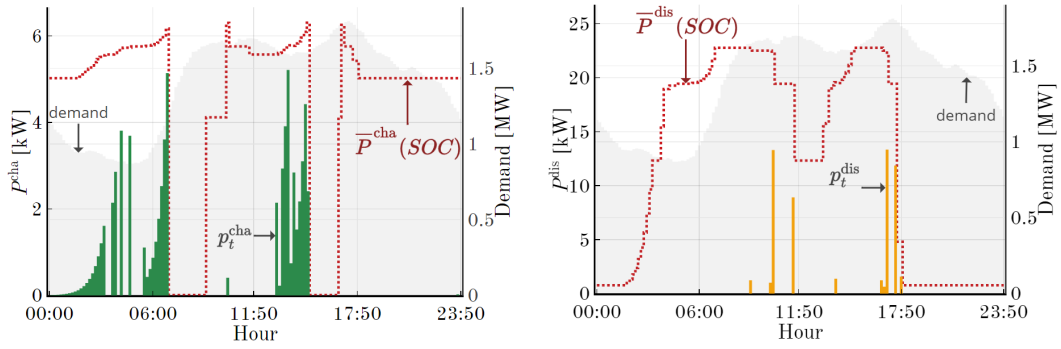

(c) Case MILP: charging power vs. time (d) Case MILP: discharging power vs. time

Figure 2.7: Scheduling of the battery charge and discharge processes for (a)-(b) Case LP–Approx, and (c)-(d) Case MILP. The dotted line denotes the maximum power as a function of the *SOC* based on Model 1. The red areas indicate infeasible operation.

2.5.2 Reliability Model Assessment

The schedule of an ideal battery model for power charging and discharging is possible in unfeasible regions of battery operation. Therefore, it is expected that there will be situations in which the battery cannot provide the power/energy required by the schedule. To calculate this mismatch, we introduce a reliability metric obtained as

follows:

1. For the time steps in which p_t^{cha} or p_t^{dis} consider values outside of the regions defined by (2.21)–(2.22), we set their values to be equal to the maximum power attainable for the given SOC.

2. The realized (corrected) charging and discharging schedule for the battery is used for updating new energy levels, e_t^{real}, based on (2.18c).

3. The energy imbalance/deviation is then calculated as the sum of the differences between the scheduled and the realized energy levels, as follows:

$$\text{Imbalance} = \sum_t \left(e_t^{\text{real}} - e_t\right) \tag{2.25}$$

Fig. 2.8 presents the scheduled SOC for an ideal battery and the realized levels resulting from this analysis. It can be observed that there exists not only a discrepancy between the scheduled and the realized values, but the battery would also reach negative energy levels, i.e., selling more energy than the available one. The energy deviation calculated by (2.25) accounts for 12.2% of the scheduled energy to be stored in the battery, resulting not only in a profit detriment for the owner but also on an overestimation of the system reliability that leads to a false sense of flexibility.

2.6 Test Case 2: Battery Modeling Impact on Stochastic Operation

A modified IEEE 33-bus system is used to test different aspects of the distribution system operation under uncertainty [100]. The formulated unit commitment problem is presented as a two-stage stochastic optimization model with solar generation and a battery system. For brevity, the detailed model formulation is given in Appendix B.

The radial distribution system, represented in Fig. 2.9, operates at 12.66 kV, with an aggregated peak demand of 4.37 MVA. The system counts with a connection

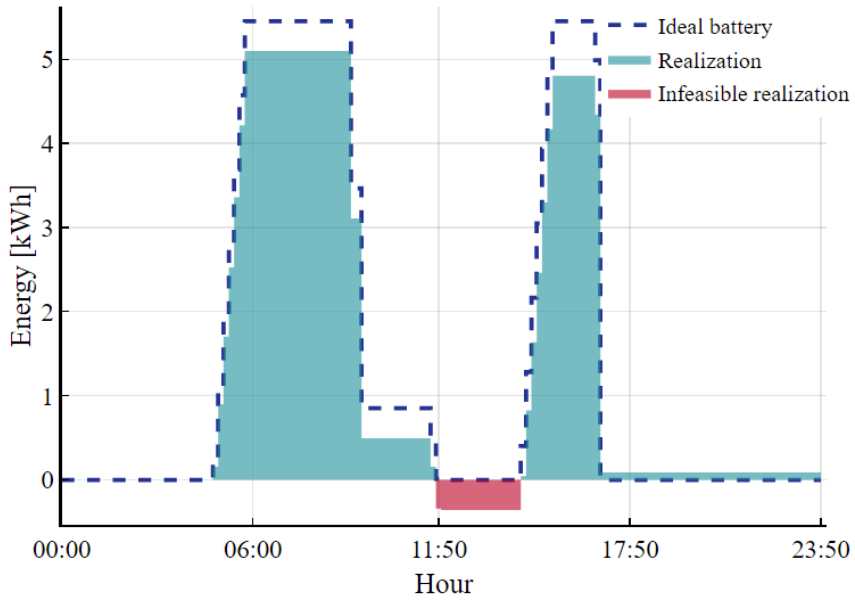

Figure 2.8: Analysis of deviations and unfeasible scheduling for an ideal battery

to the main transmission grid at node 1, two fuel-based generators at nodes 22 and 33, and a photovoltaic system of 1.5 MW at node 18. The capacity of the generators 1 and 2 are respectively 1.5 and 3 MW, and their marginal cost of generation Φ_g^{fuel} is 150 and 120 €/MWh, respectively. A lithium-ion energy storage system with a 3 MWh (power rate of 3MW, 15MW at 5C) has been placed at node 18. The network, generation and demand data, as well as the sampling point of the storage system, are available in the online appendix [101].

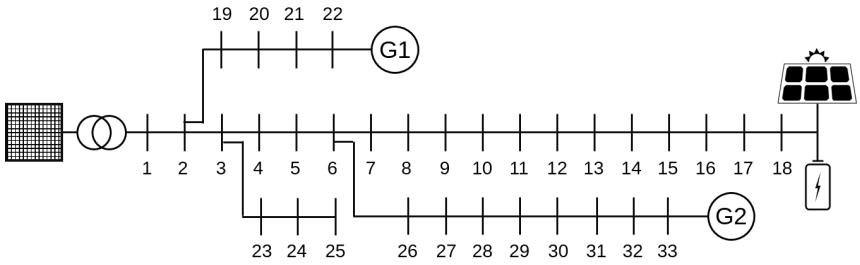

Figure 2.9: 33-bus test system

In order to simplify the analysis, only three scenarios for the stochastic RES generation will be considered. The scenarios were generated through a forecast using a seasonal ARIMA model based on surface radiation data corresponding to the first month of the year 2017 on Desert Rock, Nevada, USA [102]. The ARIMA method was chosen to produce a more accurate forecast, resulting in a non-smooth

generation curve for the 24 hours of study (see in Fig. 2.10). The probabilities associated with scenarios 1, 2, and 3 have been manually set respectively at 25, 50, and 25%.

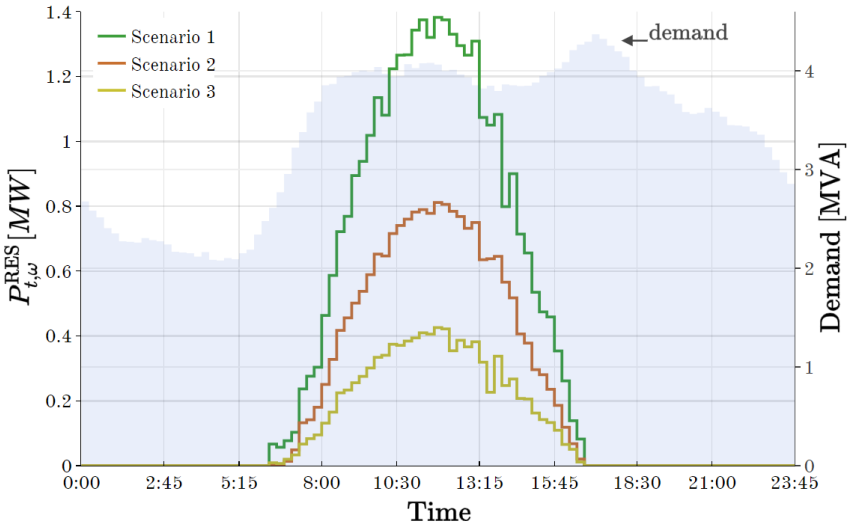

Figure 2.10: Total demand per time step and scenario of solar energy generation.

We have tested the proposed electric distribution operation with energy storage models in four cases described as follows:

- Case 1–D: optimal system's operation is solved by adopting an ideal energy storage model (2.18) in a deterministic unit commitment. The RES generation is taken as the average forecast, i.e., the mean value between the three scenarios. The average discharge and charge battery efficiencies are set to 86.8% and 97.2%, respectively.

- Case 1–S: an ideal energy storage model (2.18), and a stochastic unit commitment model (Model 10) are employed.

- Case 2–D: the solution is based on the proposed non-ideal energy storage model (Model 2) while using the deterministic unit commitment version for optimal operation model of the distribution grid.

- Case 2–S: the system is optimized with the developed a non-ideal energy storage (Model 2), and a stochastic unit commitment model (Model 10).

Table 2.2: Results summary for computational test cases.

	Case NLP	Case LP–Ideal	Case LP–Approx	Case MILP
Battery model	Ideal		Non-ideal	
Type	Deterministic	Stochastic	Deterministic	Stochastic
Total costs [€]	7 909.5	7 954.4	7 906.2	7 952.6
Computational time [s]	141.6	501.8	119.7	733.2
Total imports [MWh]	19.0	16.6	19.0	16.7
Total export [MWh]	0.0	0.0	0.0	0.0
Total realized up-reserve (ω_1) [MWh]	–	0.64	–	0.44
Total realized up-reserve (ω_2) [MWh]	–	3.0	–	3.0
Total realized up-reserve (ω_3) [MWh]	–	3.1	–	3.1
Total realized down-reserve (ω_1) [MWh]	–	0.5	–	0.4
Total realized down-reserve (ω_2) [MWh]	–	0.0	–	0.1
Total realized down-reserve (ω_3) [MWh]	–	0.0	–	0.1

2.6.1 Scheduling results

The results summary for the different test cases is presented in Table 2.2. As seen in the table, the total costs remained almost the same for all the cases. However, it is important to note that there is also a reduction in cost by using a detailed battery model instead of the ideal one; explained by the use of the battery in regions of higher efficiency.

Model 2 Linear Li-ion battery model

Variables:

e_t, SOC_t	battery energy level (absolute and relative values)	[Wh,–]
$p_t^{\text{dis}}, p_t^{\text{cha}}$	discharging and charging power	[W]
$p_t^{\text{out}}, p_t^{\text{in}}$	power outgoing and incoming at the cells	[W]
x_{jt}, y_{kt}	auxiliary variables related to the characterization sets J and K	[–]

Constraints:

$$e_t = e_{t-1} + \left(p_{t-1}^{\text{in}} - p_{t-1}^{\text{out}}\right)\Delta, \qquad \forall t \tag{2.23a}$$

$$p_t^{\text{out}} = \sum_j \widehat{P}_{jt}^{\text{out}} x_{jt}, \qquad \forall t \tag{2.23b}$$

$$p_t^{\text{dis}} = \sum_j \widehat{P}_{jt}^{\text{dis}} x_{jt}, \qquad \forall t \tag{2.23c}$$

$$p^{\text{in}} = \sum_k \widehat{P}_{kt}^{\text{in}} y_{kt}, \qquad \forall t \tag{2.23d}$$

$$p^{\text{cha}} = \sum_k \widehat{P}_{kt}^{\text{cha}} y_{kt}, \qquad \forall t \tag{2.23e}$$

$$SOC_t = \sum_j \widehat{SOC}_{jt} x_{jt} + \sum_k \widehat{SOC}_{kt} y_{kt}, \qquad \forall t \tag{2.23f}$$

$$SOC_t = e_t / \overline{E}, \qquad \forall t \tag{2.23g}$$

$$1 = \sum_j x_{jt}, \qquad \forall t \tag{2.23h}$$

$$1 = \sum_k y_{kt}, \qquad \forall t \tag{2.23i}$$

$$0 \leq x_{jt}, \qquad \forall j, t \tag{2.23j}$$

$$0 \leq y_{kt}, \qquad \forall k, t. \tag{2.23k}$$

Model 3 Network-Constrained Economic Dispatch with EES

Variables:

p_{gt}	generated power by g during t	[W]
f_{lt}	line power flow through l on t	[W]
δ_{nt}	voltage phase angle at n on t	[rad]

Objective:

$$\text{min.} \qquad \Delta \cdot \sum_{g,t} C_g p_{g,t} \tag{2.24}$$

Constraints:

$$\sum_l A_{nl} f_{lt} = P_{nt}^{\mathrm{D}} - \sum_g \Omega_{gn} \cdot p_{gt} - \sum_s \Gamma_{sn} [p_{st}^{\mathrm{dis}} - p_{st}^{\mathrm{cha}}], \qquad \forall n, t \tag{2.24a}$$

$$f_{lt} = S_{base} \frac{1}{X_l} \sum_n A_{nl} \cdot \delta_{nt}, \qquad \forall l \tag{2.24b}$$

$$\underline{P}_g \leq p_{gt} \leq \overline{P}_g, \qquad \forall i, t \tag{2.24c}$$

$$-\overline{F}_l \leq f_{lt} \leq \overline{F}_l, \qquad \forall l \tag{2.24d}$$

$$\underline{\delta}_n \leq \delta_{n,t} \leq \overline{\delta}_n, \qquad \forall n \tag{2.24e}$$

$$\delta_{n=n_0,t} = 0, \qquad \forall t \tag{2.24f}$$

$$e_{t=1} = e_{t=|T|} \tag{2.24g}$$

Battery model (Model 2): (2.23). (2.24h)

The purchase of energy from the main grid for the four test cases is displayed in Fig. 2.11. The solar production is presented normalized to their maximum value, i.e., its capacity factor. Similarly, energy import prices are represented in the background. As it can be seen from the figure, the import of energy for the test cases follows the demand throughout the day. The presence of higher radiation between 10:00 and 15:00 allows to complement the use of the fuel-based generation, reducing the need for energy import. The import reduction around the noon hours is greater for the test cases that considered the probabilistic scenarios, Case LP–Ideal and Case MILP; given their consideration of the weighted effect from higher RES generation.

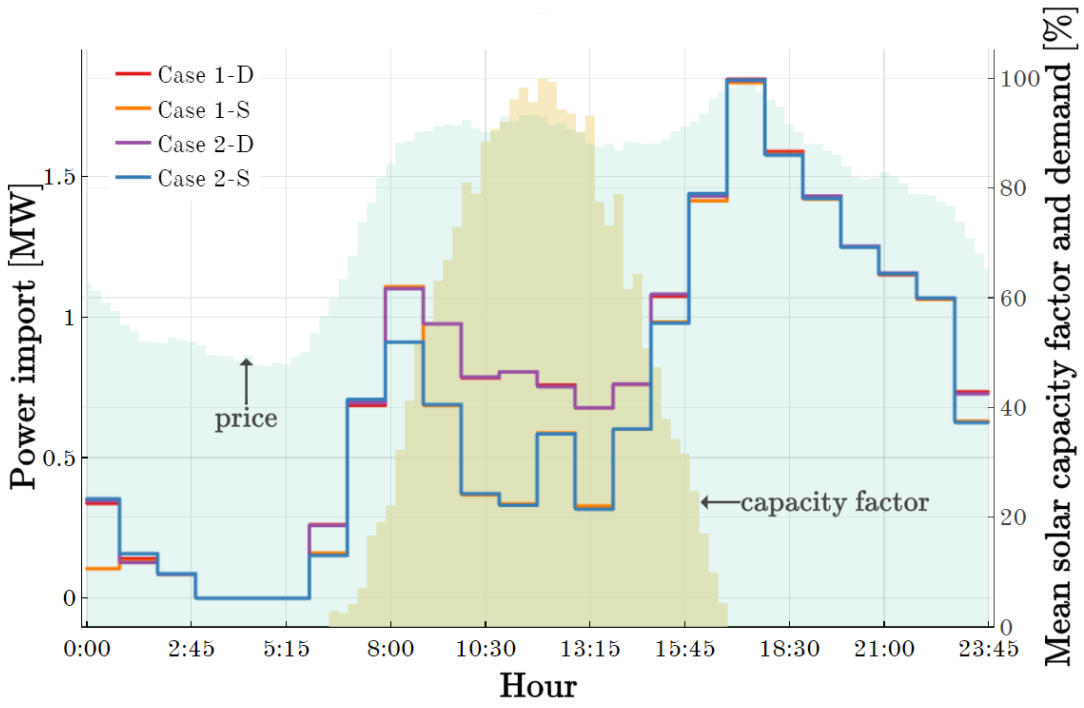

Figure 2.11: Power import per case, in comparison with the normalized solar radiation and energy import price.

Fig. 2.12 presents the energy storage operation for Case MILP. The use of the storage system for each scenario follows a similar pattern, except around the noon hours. During this time frame, the use of the storage has a direct relationship with the amount of RES generation of each scenario; for scenario 1 there is an intense storage usage, greater than, for instance, scenario 2. Whereas around the noon hours, the energy storage is discharged at (almost zero) constant power in

scenario 3. The difference in the storage usage between the scenarios highlights the importance of pairing RES with energy storage systems since they allow to balance the power generation from RES sources.

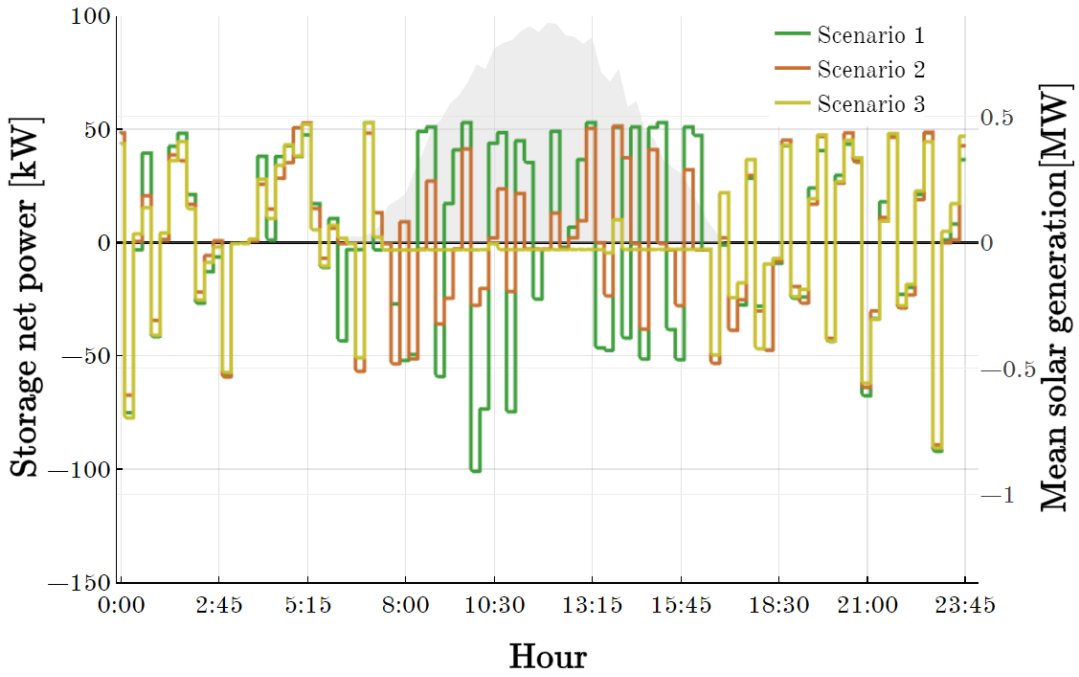

Figure 2.12: Storage usage for Case 2–S. Each trace represents the operation of the energy storage system for a different stochastic scenario. In the background, average solar generation.

2.6.2 Operation Reliability

Even though the total cost obtained, the amount of imported energy and employed reserves are similar through the four test cases, the ideal energy storage model employed in Case 1–D and Case 1–S does not take into account the variation of the maximum power that a storage system can charge and discharge as a function of its state of charge. The use of constant power limits could lead to infeasible operation of the battery, resulting in situations where the scheduled power falls outside the feasible region of operation. Fig. 2.13 presents the differences between the scheduled battery energy level for each scenario and the corrected operation, i.e., with the requested power being limited by the control system when the scheduled storage usage surpasses the technical limits presented in Section 2.3. The energy

deviation (scheduled minus corrected) for scenarios 1 to 3 was of 78.8, 113.4, and 24.7kWh, respectively representing 3.6%, 6.2%, and 1.0% of the scheduled energy to be stored with the battery. Such scheduling imbalances could produce violations of the system constraints and must be covered by the distribution system operator by purchasing more energy in the real-time market or utilizing the backup generation, incurring in additional operating expenses. Therefore, it becomes of the utmost importance not only the accurate modeling of the network and generation technical limits but also those of the energy storage system that provides additional flexibility and reserve for supporting reliable operation under uncertain and intermittent RES generation.

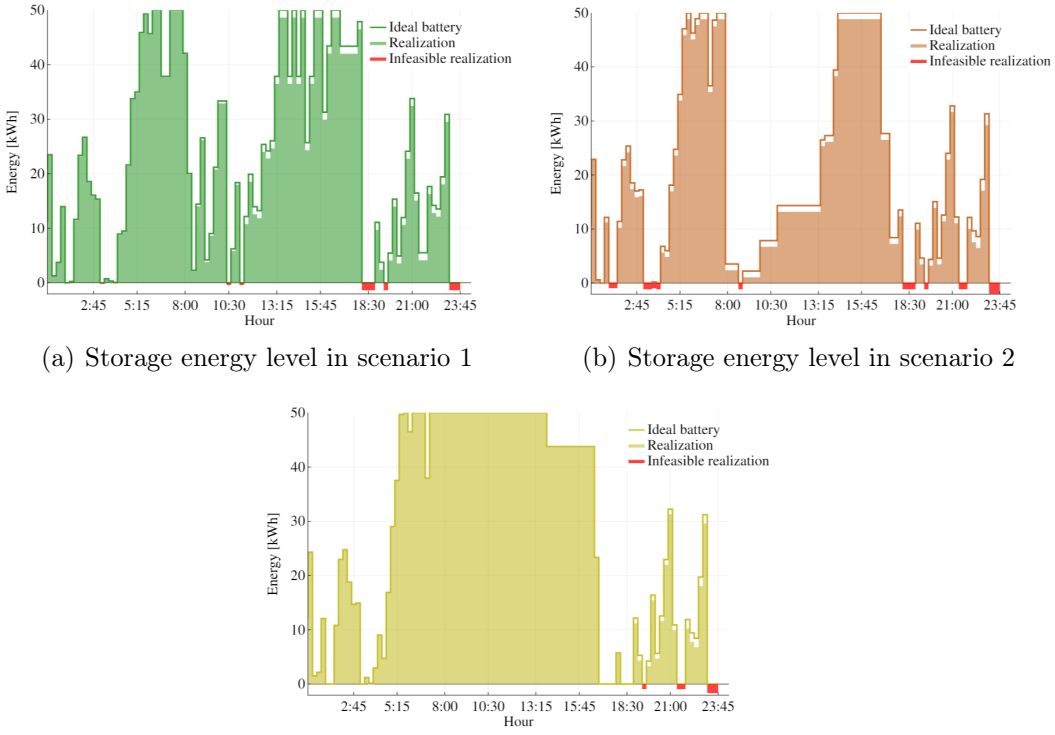

(a) Storage energy level in scenario 1

(b) Storage energy level in scenario 2

(c) Storage energy level in scenario 3

Figure 2.13: Storage energy level for Case 1–S. The solid line represents the scheduled level, while the shaded area displays the realized energy level after accounting for operation infeasibilities, i.e., limiting the power discharge to a function of the *SOC*. The red area represents negative realized values.

2.7 Conclusions

This chapter proposes a detailed model for battery characterization in optimization problems. The model is built based on a Li-ion battery, where the relationship between the state of charge, the charging and discharging efficiencies, and the power limits are described. Based on the battery's equivalent circuit representation, a linear reformulation is then proposed based on a convex envelope for all feasible operation set-points. The energy storage model is convexified providing an accurate and simple set of linear constraints that models the storage behavior with no compromise of the computational time. Although the model is constructed from a Li-ion battery data, it is general enough to cope with a variety of different technologies.

Two test cases has been presented to evaluate the benefits of employing the proposed model. In the first test case, a deterministic network-constrained economic dispatch, the performance of the developed model is compared against non-ideal (NLP), ideal (LP), and mixed-integer linear programming (MILP) models commonly used in the power systems literature. The ideal model presents violations of the technical battery power limits, accounted for a 12% deviation from the scheduled battery usage, highlighting the importance of such a detailed model to avoid wrong estimations of attainable flexibility and risking damaging the storage system. Even though the NLP and MILP models accurately represent the battery's performance and feasible operating region, their computational burden is considerably higher than that of the developed model. In the second test case, the stochastic unit commitment with renewable generation, energy storage and reserves provision is modeled. For this test case, the system scheduling, and reserves purchase and deployment is compared for the ideal and the proposed storage models. The scheduling results shows that there does not exist an increase in operation costs by utilizing the developed linearized model with a more constrained operation with state-dependent efficiency. Finally, under the different stochastic scenarios, the battery usage and its scheduling imbalances increase with renewable generation levels.

Given the increasing need for flexibility and reliability in energy systems, the proposed linear model allows characterizing the operation and technical limits of

electric battery systems through a computationally-efficient approach. The introduced battery characterization has been successfully applied in combination with online state-of-charge and state-of-health estimators, to monitor the battery performance and its capacity fading [103]. These systems could provide a continuously updating version of the battery capacity and performance, allowing to update the characteristic operation curves for charge and discharge presented in Section 2.4. We advocate, then, for the use of more detailed battery models like the one proposed in this chapter for consideration in existing power systems operation and planning problems that involve electric energy storage devices.

Chapter 3

A Heat Market for Interconnected Multi-energy Microgrids

Thermal networks, part of heat-and-power multi-energy microgrids, may face capacity issues, generation and distribution ones, either due to the increase in the requested demand or capacity underused, which is sized for peak hours. Under-capacity issues may be addressed with generation and pipeline capacity expansion, resulting in considerable capital costs and extra maintenance costs. In the case of over-capacity, better usage of the existing assets may bring further revenues and increase the multi-energy microgrid's overall energy efficiency. In the electricity sector, it is being considered the interconnection of microgrids via the distribution system network, since microgrids can operate in both islanded and network-connected modes. In this chapter, in a similar fashion, we propose the interconnection of adjacent thermal networks enabling direct heat trading among them to increase the micro-grids' supply flexibility, help meeting demand peaks, and reduce operational costs. Examples of integrated heat-and-power microgrids that could benefit from thermal interconnections are industrial parks, university campuses, hospitals, and even residential complexes with a shared heat generator.

This chapter presents a market model for the optimal heat transfer between thermally interconnected heat-and-power microgrids. The resulting model is a convex quadratic programming model that enables the derivation of heat transfer prices that guarantee a competitive equilibrium. Heat transfer between microgrids resulted

in thermal energy price reductions of about 2.4% for the presented case study. We performed numerical tests to exhibit the impact of connection topology, thermal power transfer capacity, and interconnection efficiency on transferred energy and prices.

The contents of this chapter are partially based on a paper submitted to the journal *Energy Conversion and Management*.

This chapter is organized as follows. Section 3.2 introduces the thermal coordination market, that models the operation of each integrated microgrid and the heat transfer between them as a convex quadratic optimization model. In Section 3.3, we derive the heat transfer prices and analytically prove that they establish a competitive equilibrium for the coordination market. The modeling of the coordination market as an equivalent decentralized optimization problem is presented in Section 3.4. Lastly, in Section 3.5, we realize the computational tests and sensitivity analysis that highlight the impact on the transferred quantities and their prices by the difference in area prices, transfer capacity, and efficiency, as well as interconnection topology.

Nomenclature

The mathematical symbols used in this chapter are described in the table below:

Indexes

a	Integrated heat-and-powers areas (microgrids)
$b \in \mathcal{T}_a$	Areas with direct thermal connection to a

Parameters

$C^{(\cdot)}_{(\cdot),a}$	Area generation cost coefficients	[–]
$K^{(\cdot)}_{a,l}$	Area coefficients for generation operation boundaries l	[–]
H^{D}_a	Area heat demand	[MWh]
$\overline{H}^{\mathrm{tr}}_{ab}$	Heat transfer capacity between areas a and b	[MWh]
P^{D}_a	Area electricity demand	[MWh]
$\overline{P}_a$	Area electricity exchange capacity with the external grid	[MWh]

η_{ab}^{tr}	Transfer efficiency of the pipeline between areas a and b	[–]
$\pi_a^{\text{imp/exp}}$	Area electricity import/export price	[€/MWh]

Variables

c_a	Area generation costs	[€/MWh]
c_a^{exch}	Area electricity exchange costs with external grid	[€/MWh]
$h_{ab}^{(a)}$	Area a's local variable of the heat transferred from a to b	[MWh]
h_a	Area heat generation	[MWh]
p_a	Area electricity generation	[MWh]
$p_a^{\text{imp/exp}}$	Area imported/exported electric energy	[MWh]
γ_a	Area marginal heat cost	[€/MWh]
γ_a^{eff}	Perceived export price at area b after the interconnection losses has been considered	[€/MWh]
$\overline{\kappa}_a$	Marginal cost savings that would be derived from increasing the export capacity for the interconnection a–b	[€/MWh]
λ_a	Area marginal electricity cost	[€/MWh]
μ_{al}	Area marginal generation cost increment of area a for reaching the generation operational boundary l	[€/MWh]
$\overline{\phi}_{ab}$	Marginal costs savings incurred by increasing the electricity import capacity for area a	[€/MWh]
χ_{ab}	Marginal heat export cost from area a to area b	[€/MWh]
$\overline{\psi}_{ab}$	Marginal costs savings incurred by increasing the electricity export capacity for area a	[€/MWh]

3.1 Introduction

Heat-and-power microgrids[1], i.e., systems with local generation that are connected to external networks and can operate either in a network-connected or islanded modes, are often present in urban areas independently of whether a district heating system is present or not; this is the case of hospitals, university campuses, shopping

[1]For simplicity and to improve readability, we will use the terms microgrid and area interchangeably for the remainder of the chapter.

malls, sports centers, or even residential areas with shared heating system, including building blocks. The design and management of such microgrids could be a challenging task, having to deal with under- and over-capacity issues while seeking for flexible operation. The adequacy of operational flexibility and under-capacity in supply of thermal energy including generation and distribution, may be addressed with a set of possible solutions, such as supply temperature increase, pipeline expansion, additional generation capacity installation, and via more modern solutions like thermal storage deployment [104]. These measures, mainly design ones, could result in generation, distribution, or storage capacity redundancy or under-use, with the microgrid units being used at rated capacity for low period of time.

The implementation of a heat market between microgrids could reduce operational costs by diversifying revenue streams and increase generation efficiency with the an operation of the microgrid units closer to their nominal value [105]. Thus, leading to enhanced flexibility and reduction of primary energy consumption, helping to achieve emission reduction goals. Heat transfer between areas would be especially beneficial in cases when the demand peaks of each microgrid are not simultaneous, or when one of the areas possesses either underused capacity or energy storage to produce internal load-shifting. These area characteristics would enhance the economic benefits derived from a heat market without the need of increasing the installed generation capacities. Furthermore, such market can be used to enhance flexibility for the fulfillment of electric loads or making profit out of the electric market. An example of these cases is when the thermal loads are met by energy conversion units interconnected with the electric grid, e.g., combined heat and power (CHP) cogenerating heat and electricity or power-to-heat (P2H) units converting electricity into heat via heat pumps or electric boilers. P2H is becoming more common with the progressive electrification of the heating systems. The dimensions of connected microgrids can range from smaller ones such as building blocks provided with shared heat generation units and their own heat network, to clusters of building blocks or other kind of buildings, like hotels, shopping malls, hospitals and university campuses that may reach the size of a town district as small DH networks. A general area configuration representing the previously described heat-and-power microgrids

is presented in Figure 3.1 with a basic interconnection topology for the heat transfer between the microgrids.

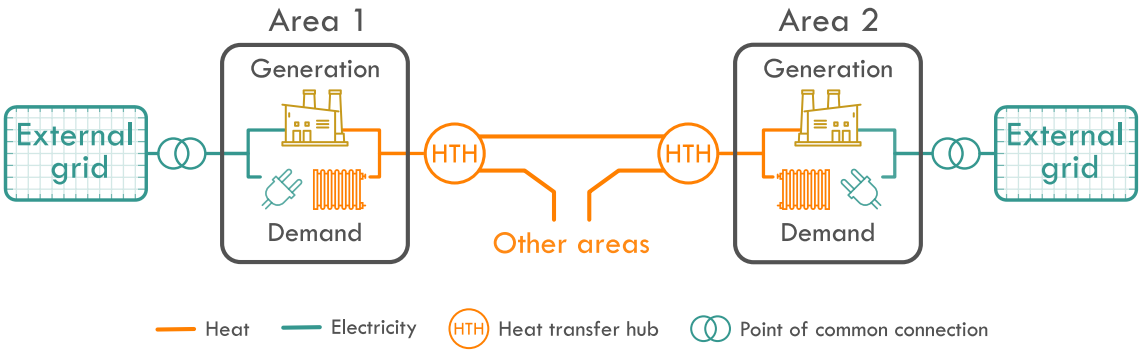

Figure 3.1: General configuration of heat-and-power areas with heat interconnection.

In the following Section 3.1.1 we describe the main characteristics of a heat trading system between microgrids. On Section 3.1.2 we discuss the existing approaches for coordination of energy exchange between multi-energy microgrids.

3.1.1 Heat market implementation

Heat trade between microgrids can be performed by interconnecting areas directly via pipelines through which heat transfer fluid from one grid flows directly to the other, or indirectly via heat transfer hubs (HTHs) [106]. In the first case fluid pressure balance needs to be accurately monitored and controlled so as to enable safe and effective exchange of heat, leveraging upon the experience of district heating networks management. In the second case, the HTH is a heat exchanging substation between two or more areas that brings the exchanging temperature to lower levels with the use of heat exchangers. In the HTHs, energy exchange is allowed through the interconnection of the supply and return circuits of the areas [60]. The use of HTHs suits better the scenario where the networks operate at different temperatures and unidirectional flow is required. Such a scenario is when one area is fed by a CHP with pressurized water above 100°C or just below (2nd and 3rd generation DH), and the other one works with heat pumps and water at 50–60 °C suitable for renewable energy integration (4th generation DH).

Interconnected heating networks have been studied under the paradigm of energy

hubs (EHs) and interplant interconnection. A multi-objective optimization model for the heat and electricity transfer between energy hubs with emissions and cost reduction was presented by Maroufmashat *et al.* [107]. This work was expanded by including the optimal design and planning of interconnected EHs [108]. These works presented the multi-energy balance for the interconnected microgrid systems, showing an increase in the microgrids' operational flexibility and cost reduction by transferring heat between locations. Ayele *et al.* developed an extended multi-carrier multi-site energy hub model. The presented model allows for the calculation of the electricity and heat flows between the microgrids, while accounting for the network losses and flow directions derived from hydraulic balances. The heat transfer through interplant integration was studied by Chang *et al.* [60]. In this work, a mixed-integer non-linear programming (MINLP) model is introduced to design a system that would allow the plants' coordination while minimizing the total annual costs. The proposed MINLP model allowed the design of the heat transfer mechanisms in a centralized interplant heat transfer hub, which reduces costs when compared to a direct interplant transfer through long pipelines. A model for the planning of heat integration between industrial plants is presented in [61]. The objective of the resultant mixed-integer linear programming (MILP) model is the minimization of the total operational costs, including the costs of pipeline installation. The authors presented computational scenarios with industrial plants with different generation units and energy requirements. It was observed that for low investment budgets, the preferred solution is the interconnection via above-ground pipelines with high-pressure steam. For larger budgets, the optimal solution is to utilize underground pipelines, given their lower heat losses, and with lower steam pressure. The conducted tests report that the heat integration of industrial plants would allow at least a 20% reduction of operational costs, pipeline invested included.

Even though the previously referred models allow for the transfer of heat among locations, along with electricity, and gas, they explore the systems operation but do not consider the economic interaction between them. This is due to the fact that in the operational stage the costs' minimization was performed in a centralized manner and the payment allocation between the different microgrids (plants or hubs) was

not analyzed. To the authors' best knowledge, thermal EHs interconnection with an analysis of the market structure, i.e., price derivation and price-dependence analysis on technical aspects, has not been performed. Therefore, the market design for the heat trade between interconnected multi-energy microgrids represents an interesting flexibility measure to analyze and gain insights into its economic benefits.

3.1.2 Market coordination

As previously mentioned, a heat market implementation can be economically and technically advantageous for its participants. Nevertheless, it is needed to find a way for it to be performed effectively, which will also affect the business model to adopt. The market coordination could be centralized, where the market operator must have full knowledge of the participating areas' technical and economic parameters, and control, directly or indirectly the decision variables. In this case, the net heat import payments are collected by the market operator and redistributed to the net heat exporters based on the exchanged energy and its price. A centralized market operation raises concerns about both the practical implementation and privacy preservation of its participants. Consequently, there is an increasing interest in the use of decentralized algorithms to represent multi-agent optimization problems [109]. In this way, the exchanged heat quantity and price is iteratively and independently calculated by each microgrid to optimize its economic operation based on the offered trading volumes and prices. This approach is thus characterized by the bilateral agreement between microgrids for the exchange of heat and does not require a third-party for the payments settlement. The requirements for decentralized coordination methodologies are: i) assurance of convergence to the global optimum, ii) preservation of private area information, iii) rapid convergence, and iv) recoverability of optimum transfer quantities and their exchange prices.

The coordination of the electric power system and the district heating system was modeled in a decentralized manner through a combined heat and power dispatch model using Bender's decomposition [110]. In this work, the operators of the electric and thermal subsystems optimize their sub-problems and transfer boundary variables, and operation bounds iteratively until convergence to the optimal solution.

However, the focus of this work was on the coordination of the electric and heating subsystems (utilities), rather than that of independent multi-energy microgrids. The pricing for the energy exchange between electric microgrids was investigated by Lu *et al.* [111]. The trading mechanism divides the microgrids into supply and demand pools, and iteratively verifying the feasibility of the optimal decentralized exchange quantities based on the bids of the microgrids. Given that in [111] the trading was performed based on genetic algorithms with binary variables, the methodology does not guarantee solution optimality and cannot be scaled to larger systems. Cheng *et al.* presented a game-theoretical approach for the heat integration of industrial plants [59]. The optimal interconnection topology, transfer flows, and transfer prices were derived with a MILP model. This design methodology considered the presence of thermal-only plants. However, a MILP formulation does not allow the the exact problem decomposition for decentralized operation. The decentralized coordination of heat-and-power energy hubs with the electric distribution network was presented in [58]. The alternating direction method of multipliers (ADMM) was used to electricity exchange between the EHs and the external distribution network. In the ADMM, the microgrids iteratively exchange the amount of power that they would prefer to exchange, i.e., each agent optimizes its operation. If there is a disagreement between the desired exchange quantities, the exchange is penalized, and every agent must optimize its operation once again with the new penalty value. A decentralized direct-current energy exchange network (EEN) composed of microgrids (MGs) was proposed by Liu *et al.* [112]. The EEN allows the electricity trade with the alternating direction method of multipliers (ADMM), preserving the private information of the participating MGs.

The interconnection of heating areas requires the design of a heat transfer market. An efficient market operation guarantees the optimal heat exchange between areas and its adequate pricing. Thus, ensuring that the market outcomes are beneficial for all of its participants. Performing a market analysis would allow network owners to understand the economic benefits of interconnecting with neighboring networks and through investment studies assess its viability. This chapter studies the basic structure of a heat market for interconnected thermal networks. We model

these thermal networks as heat-and-power microgrids where heat and electricity are locally generated and distributed to serve the demand. The inclusion of electricity generation is due to the high total efficiency of CHP plants (considering both electric and thermal energy generated), which therefore is utilized to produce about four-fifths of the thermal energy in current district heating systems [113]. Due to ambitious decarbonization targets, the interconnection between thermal and electric energy vectors is indeed expected to increase [51]. Current regulations and technical challenges related to responsibilities on system stability and security do not allow the bidirectional electricity transfer between microgrids through the external distribution network. Therefore, we assume that the electricity exchange is not performed bilaterally among microgrids, but between the microgrids and the external distribution network that acts as an infinite capacity source/sink of electric energy. The contributions of this chapter are fourfold:

i) Design of a convex heat market between heat-and-power microgrids. Such a market, to the authors' best knowledge, is yet to be analyzed in the literature that mainly focuses on electricity and gas interconnections.

ii) Sensitivity analysis of the key drivers of heat transfer quantities and prices: transfer capacity, transfer efficiency, and interconnection topology.

iii) Leveraging the properties of the convex coordination market, we derive its heat transfer prices, proving that they guarantee a competitive equilibrium, where each participant maximizes its profits and has no incentive to deviate from the market outcome.

iv) Presentation of an equivalent decentralized coordination model for the heat transfer between microgrids that preserves operation independence and privacy. Therefore, increasing the implementation applicability of the proposed market in real-world scenarios.

3.2 Heat market formulation

The purpose of the coordination market is the calculation of the optimal heat transfer between integrated multi-energy heat-and-power microgrids. This section presents the units performance and operation region characterization, the heat transfer between areas, and the model for the electricity exchange with the external gird. The full model is summarized at the end of the section.

3.2.1 Assumptions

The following assumptions were made in order to simplify the presented analysis:

i) **Only thermal interconnection:** the considered areas can only transfer thermal energy between them through short-distance, i.e., hundreds of meters, heating pipelines.

ii) **Aggregated generation and demand:** each area is modeled as if a single unit and user represent respectively all the internal generation and demand. Therefore, no network constraints in neither the thermal nor electric systems are considered. The generation and demand clustering is done to simplify the analysis and reduce the model size, considering that the aim is to assess the proposed market operation.

iii) **Operation scheduling:** short-term phenomena such as thermal inertia and stochastic demand are not considered.

iv) **Single time-step:** the heat market operation is analyzed considering individual time steps in the scheduling regime, e.g., one hour. Therefore, ramp constraints, as well as energy storage units, are not considered.

Given that this work describes the basic operation of a market for the coordination of heat transfer between microgrids, the underlying area characterization is simple but comprehensive enough to include the relevant features of integrated heat and power microgrids. The considered assumptions could be easily adjusted to represent a more detailed operation of the interconnected areas, without affecting the economic and technical principles discussed in this work.

3.2.2 Operational costs

In a multi-area dispatch, the operational costs can be classified as: i) generation costs, and ii) electricity exchange costs.

Generation costs

The generation costs for an area that can produce both electricity and heat can be modelled as a second-degree polynomial of its thermal, h_a, and electric, p_a, output:

$$c_a = C^{\mathrm{p}}_{2,a} p_a^2 + C^{\mathrm{p}}_{1,a} p_a + C^{\mathrm{h}}_{2,a} h_a^2 + C^{\mathrm{h}}_{1,a} h_a + C^{\mathrm{hp}}_{a} h_a p_a + C_{0,a}, \ \forall a \tag{3.1}$$

where $C^{\mathrm{p}}_{2,a}, C^{\mathrm{p}}_{1,a}, C^{\mathrm{h}}_{2,a}, C^{\mathrm{h}}_{1,a}, C^{\mathrm{hp}}_{a},$ and $C_{0,a}$ are cost coefficients. These coefficients can be fitted based on the electric and thermal energy conversion efficiencies of the generation units throughout the operating region. A thermal-only microgrid can be modelled by setting to zero the value of the appropriate coefficients, related to electric generation.

Electricity exchange costs

The cost of electricity exchange with the external grid can be calculated based on the imported, p^{imp}_a, or exported, p^{exp}_a, energy:

$$c^{\mathrm{exch}}_a = \pi^{\mathrm{imp}}_a p^{\mathrm{imp}}_a - \pi^{\mathrm{exp}}_a p^{\mathrm{exp}}_a, \quad \forall a \tag{3.2}$$

where π^{imp}_a and π^{exp}_a are the given values for the electricity import and export prices for each area.

3.2.3 Area generation characterization

The area representing the multi-energy microgrid, capable to generate heat and power is modelled as a single cogeneration unit. In this manner, several electric-only, heat-only and cogeneration units are clustered as a single generation unit.

The relationship between the generated heat and power in each area can be described as a convex operation region, Figure 3.2. In this way it was possible

to be as much general as possible, aiming at representing any kind of heat and power generation unit, consistently with the high level scope of this chapter, while for specific studies ad hoc cost functions could be identified and implemented. This region can be characterized as the area between the inequalities describing the edges by [57]:

$$p_a K^{\mathrm{p}}_{al} + h_a K^{\mathrm{h}}_{al} \leq K^{0}_{al}, \qquad \forall a, l. \tag{3.3}$$

The signs of the coefficients $K^{\mathrm{p}}_{al}, K^{\mathrm{h}}_{al}$, and K^{0}_{al} define the type of bound l of the

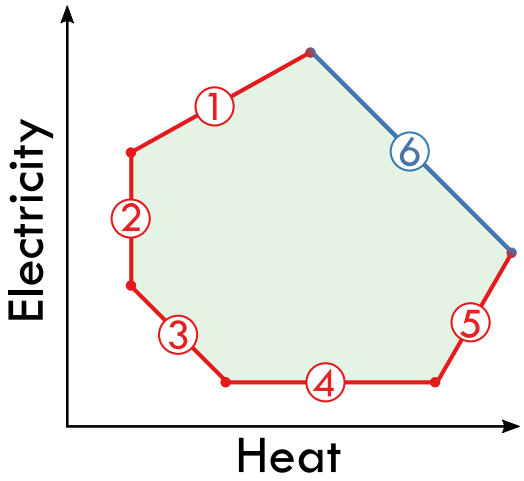

	K^{p}_{al}	K^{h}_{al}
①	>0	<0
②	=0	<0
③	<0	<0
④	<0	=0
⑤	<0	>0
⑥	>0	>0

Figure 3.2: General convex operation region for a cogeneration area. The sign of the boundary parameters depend on the type of boundaries, 1–6.

polygon. Convex polygons represent units with two independent variables for its electricity and heat generation, e.g., fuel and the valve opening in a extraction condensing steam turbine, as well as units with one independent variable coupled with thermal energy storage. Units with one independent variable, (fuel) are represented by two inequalities, a combination of lines ① and ⑤, that represent a line segment, e.g., back-pressure turbines. Note that heat-only areas can be described with (3.3), by fixing the appropriate coefficients to zero, resulting in a horizontal line shifted to zero of value of the y axes. Electricity-only areas are analogously defined by a vertical line set at zero on the x axes.

3.2.4 Heat transfer between areas

We consider an energy-based steady-state operation, as per assumption, to coordinate the heat transfer between areas, i.e., temperature dynamics and time delays along the pipeline are neglected. The heat carrier, namely water, mass flow and temperature at the connection pipelines are assumed to be such that could ensure the transfer of the scheduled amount of thermal energy. The heat flow between two areas can be mathematically modelled either with 1) a heat transfer as a centralized value, or 2) through a heat transfer with local copies. Both approaches and their mathematical properties will be examined in this subsection.

Heat transfer as a centralized value

The thermal energy flow between two areas, 1 and 2 in Figure 3.3(a), can be described in terms of the heat sent/received at the ends of the pipeline and its transfer efficiency η_{12}^{tr}. The relationship between the heat sent from area 1, and that received at area 2 from area 1 can be described by:

$$h_{12}^{\text{sent}} = h_{12} \tag{3.4a}$$

$$h_{21}^{\text{received}} = \eta_{12}^{\text{tr}} h_{12} = \eta_{12}^{\text{tr}} h_{12}^{\text{sent}}. \tag{3.4b}$$

For the two-area case, expressions (3.4) allow us to include the heat export and import in the areas' heat balances as:

$$H_1^{\text{D}} = h_1 + \eta_{21}^{\text{tr}} h_{21} - h_{12}, \tag{3.5a}$$

$$H_2^{\text{D}} = h_2 + \eta_{12}^{\text{tr}} h_{12} - h_{21}, \tag{3.5b}$$

$$h_{12} \cdot h_{21} = 0, \tag{3.5c}$$

$$h_{12}, h_{21} \geq 0, \tag{3.5d}$$

where H_a^{D} and h_a are respectively the total areal heat demand and generation. The quantities h_{12} and h_{21} represent the heat transferred from area 1 to area 2 and in the reversed direction. Expression (3.5c) ensures that only one area is exporting heat at a time, while (3.5d) sets the export quantities as non-negative.

The set of expressions (3.5) allows to completely model the heat transfer between two areas, but (3.5c) makes this a non-convex model. Expression (3.5c) can be omitted, since there is an economic objective of minimizing operational costs and the transfer efficiency $\eta_{12}^{\text{tr}}=\eta_{21}^{\text{tr}}<1$.

Having the variables h_{12} and h_{21} "shared" between the areas, i.e., they are included in the heat balances of both areas, is not suitable for economic operation, since there is not a straightforward way of decomposing the operation problem between the areas in such a manner that each area solves a model with variables and parameters that are not present in its neighbors energy balances. Therefore, besides disallowing independent area operation, the centralized heat transfer scheme (3.5) requires the sharing of operational and technical information which could lead to strategic bidding by the other areas.

To overcome this issue, we model the heat transfer between areas in terms of local copies of the transfer variables, i.e. each area has a local variable representing the values of the shared variables involved in the transfer.

Heat transfer with local copies

An alternative approach for the transfer of heat between two areas is to create local copies of the transfer variables, e.g., the variable h_{12} will be represented as a local copy $h_{12}^{(1)}$ in area 1 and another one $h_{12}^{(2)}$ in area 2; as shown in Figure 3.3(b). The use of local copies allows us to rewrite the thermal energy balances(3.5) as:

$$H_1^{\text{D}} = h_1 + \eta_{12}^{\text{tr}} h_{21}^{(1)} - h_{12}^{(1)}, \tag{3.6a}$$

$$H_2^{\text{D}} = h_2 + \eta_{21}^{\text{tr}} h_{12}^{(2)} - h_{21}^{(2)}, \tag{3.6b}$$

$$h_{12}^{(1)} = h_{12}^{(2)}, \tag{3.6c}$$

$$h_{21}^{(1)} = h_{21}^{(2)}, \tag{3.6d}$$

$$h_{12}^{(1)}, h_{21}^{(1)}, h_{12}^{(2)}, h_{21}^{(2)} \geq 0. \tag{3.6e}$$

Expressions (3.6c) and (3.6d) ensure the agreement (coordination) on the exchanged heat by the areas. In a decentralized framework, i.e., each area solves its own operation model, expressions (3.6c) and (3.6d) are verified between iterations. In

Section 3.4 we present the decentralized coordination of the heat market.

For transfer efficiencies $\eta_{12}^{\text{tr}}<\eta_{21}^{\text{tr}}=1$ this approach leads to a unique and convex solution of the heat transfer problem, since the transfer of heat in two directions at the same time would result in higher costs due to the apparent wasted heat. Therefore, at the optimal solution: $h_{12}^{(1)} \cdot h_{12}^{(2)} = 0$ and $h_{21}^{(1)} \cdot h_{21}^{(2)} = 0$.

(a) Global transfer value (b) Local area copies

Figure 3.3: Modelling of heat transfer values.

3.2.5 Energy balances

The electric energy balance is characterized by meeting the electric load P_a^{D}, with the area generation p_a and the use of the energy exchange with the external distribution network through electricity import p_a^{imp} and export p_a^{exp}:

$$P_a^{\text{D}} = p_a + p_a^{\text{imp}} - p_a^{\text{exp}}, \qquad \forall a. \tag{3.7a}$$

The thermal load balancing of area a is achieved through the use of the internal heat generation h_a and the heat transfer with neighboring areas $b \in \mathcal{T}_a$. $\mathcal{T}_a$ is the set containing the areas connected to a. The generalization of the thermal energy balance for two areas presented in Section 3.2.4 can be written as:

$$H_a^{\text{D}} = h_a + \sum_{b \in \mathcal{T}_a} \left(\eta_{ba}^{\text{tr}} h_{ba}^{(a)} - h_{ab}^{(a)} \right), \qquad \forall a. \tag{3.7b}$$

3.2.6 Electricity exchange limits

There exists a limit on the maximum amount of electricity that can be imported (exported) to (from) the external grid. This limit is set by the transformer capacity at the main substation, i.e., point of common connection with the external grid.

The area bounds for electricity import p_a^{imp} and export p_a^{exp} are set by

$$0 \leq p_a^{\text{imp}} \leq \overline{P_a}, \qquad \forall a \tag{3.8a}$$

$$0 \leq p_a^{\text{exp}} \leq \overline{P_a}, \qquad \forall a. \tag{3.8b}$$

3.2.7 Global system optimization

Model 4 summarizes the global model for the optimal heat exchange between multi-energy microgrids. The optimal operation of a combined heat-and-power microgrid is performed by minimizing its operational costs composed of the generation costs, and the electricity import and export costs through the main substation to the external electric system (3.9a), while satisfying the thermal and electric demand. The generation costs (3.9b) are given as a quadratic polynomial of the heat and power generation in the areas. Areal electric and thermal energy balances are respectively set in (3.9c) and (3.9d). In the heat balance (3.9d) $b \in \mathcal{T}_a$ are the areas thermally connected to a. The feasible operation region for the equivalent combined heat and power unit is defined by a convex polygon (3.9e).

Heat transfer continuity is ensured in (3.9f), whereas heat transfer limits are set by (3.9g). Please note that we do not bound the variable $h_{ab}^{(b)}$, since through (3.9f)

Model 4 Area Coordination Dispatch [QP]

$$\text{min.} \quad \sum_a \left(c_a + \pi_a^{\text{imp}} p_a^{\text{imp}} - \pi_a^{\text{exp}} p_a^{\text{exp}}\right) \tag{3.9a}$$

subject to

$$c_a = C_{2,a}^{\text{p}} p_a^2 + C_{1,a}^{\text{p}} p_a C_{2,a}^{\text{h}} h_a^2 + C_{1,a}^{\text{h}} h_a + C^{\text{hp}} h_a p_a + C_{0,a}, \quad \forall a \tag{3.9b}$$

$$(\lambda_a): \quad P_a^{\text{D}} = p_a + p_a^{\text{imp}} - p_a^{\text{exp}}, \quad \forall a \tag{3.9c}$$

$$(\gamma_a): \quad H_a^{\text{D}} = h_a + \sum_{b \in \mathcal{T}_a} \left(\eta_{ba}^{\text{tr}} h_{ba}^{(a)} - h_{ab}^{(a)}\right), \quad \forall a \tag{3.9d}$$

$$(\mu_{al}): \quad p_a K_{al}^{\text{p}} + h_a K_{al}^{\text{h}} \leq K_{al}^0, \quad \forall a \tag{3.9e}$$

$$(\chi_{ab}): \quad h_{ab}^{(a)} = h_{ab}^{(b)}, \quad \forall a, b \in \mathcal{T}_a \tag{3.9f}$$

$$(\overline{\kappa}_a): \quad 0 \leq h_{ab}^{(a)} \leq \overline{H}_{ab}^{\text{tr}}, \quad \forall a \tag{3.9g}$$

$$(\overline{\psi}_a): \quad 0 \leq p_a^{\text{imp}} \leq \overline{P_a}, \quad \forall a \tag{3.9h}$$

$$(\overline{\phi}_a): \quad 0 \leq p_a^{\text{exp}} \leq \overline{P_a}, \quad \forall a. \tag{3.9i}$$

it will implicitly be bounded by (3.9g). The explicit addition of transfer limits for $h_{ab}^{(b)}$ leads to a redundancy of constraints, which translates into a degenerated dual problem. Thus, it would be possible that the dual variables take different values, through the use of different solving algorithms. Given that we derive the market prices from the values of Model 4's dual variables, dual degeneracy could lead to multiple prices for each area employing a different solution algorithm. Degeneracy in the dual problem is thus a property not desirable for the economic coordination of microgrids, and is easily avoidable by not imposing bounds on $h_{ab}^{(b)}$. Finally, the limits for electricity exchange with the external grid are set by (3.9h) and (3.9i).

3.2.8 Flexibility gains from thermal interconnection

The thermal interconnection between adjacent microgrids reduces operational costs by reducing the thermal generation costs of the heat importing area, and increasing the exporter's revenue. Additional to its financial benefits, the thermal interconnection between microgrids increases their thermal and electric flexibility. Figure 3.4 displays in green the feasible operating region of an illustrative area generation represented as an extraction condensing steam turbine. Prior to its thermal interconnection with another area, the optimal electricity and heat generation are displayed as a circle and its electric flexibility as a blue line, i.e., how much its electric power output can change. Without interconnection the area cannot modify its heat generation, since it must match the local demand and cannot import or export heat. However, if so needed, the electricity generation could be increased to match an increase on the electric demand up to the limit defined by the blue line.

Once there exists a thermal interconnection of capacity $\overline{H}_{ab}^{\text{tr}}$ with another area, the heat generation must not exactly match the local demand, gaining the orange line as a new feasible operating range. In a similar manner, since the generated heat can be adjusted by managing the imported/exported heat, the feasible electricity output can also be altered within the new feasible operating region, indicated by the purple line. For this particular case, the increase in electric flexibility only comes from reducing the thermal output by importing heat, since exporting heat and consequently increasing the thermal generation would reduce the feasible electricity

generation. Therefore changes in the electric demand would be met with either a change in imported/exported electricity from the external grid or with increasing the heat import and adjusting the electricity generation accordingly.

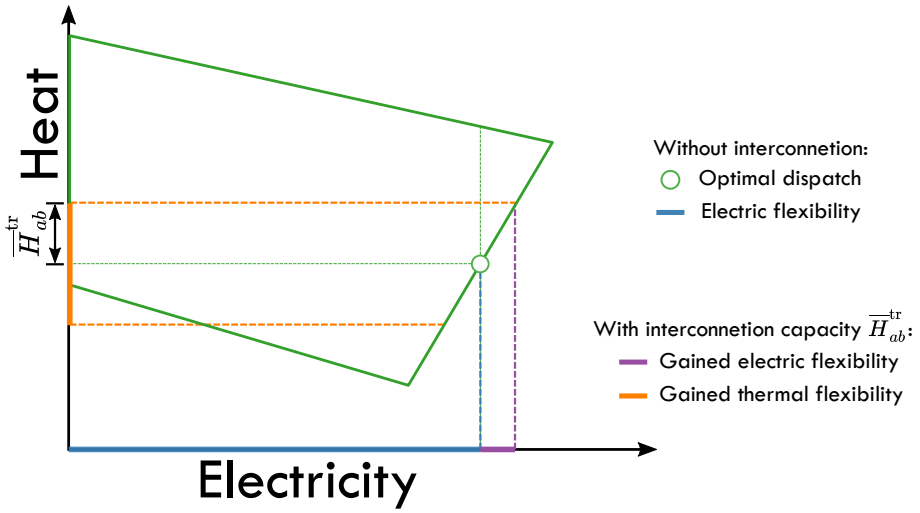

Figure 3.4: Flexibility gains derived from a thermal interconnection of capacity $\overline{H}^{\text{tr}}_{ab}$

3.3 Pricing heat transfer between areas

Duality theory can be used to derive the electricity and heat prices in an integrated energy system [57]. The dual multipliers of the expressions in Model 4 are presented next to them in Greek alphabet, e.g., λ_a for expression (3.9c) and γ_a for expression (3.9d). The dual multipliers represent the changes in the objective function derived from the modification of the constant terms in the expressions [114]. Therefore, the meaning of the dual variables can be understood as follows: *i)* λ_a and γ_a are respectively the marginal electricity and heating costs at area a; *ii)* χ_{ab} is the marginal heat export cost from area a to area b; *iii)* μ_{al} is the marginal generation cost increment of area a for reaching the generation operational boundary l; *iv)* $\overline{\kappa}_{ab}$ reflects the marginal cost savings that would be derived from increasing the export capacity for the interconnection a–b; and finally *v)* $\overline{\psi}_a$ and $\overline{\phi}_a$, analogously to $\overline{\kappa}_{ab}$, represent the marginal costs savings incurred by increasing the electricity import and export capacity for area a. The value of the dual values at the optimum operation point, i.e., at its minimum cost, can be calculated by solving Model 4's dual problem.

Alternatively, based on Model 4's optimality conditions we can derive analytical expressions for the dual variables that relate them to our scheduling (primal) variables (p_a, h_a, and h_{ab}^{tr}). This second approach is the one used in this work, since it allows us to infer the physical meaning behind the derived analytical expressions of the energy prices.

3.3.1 Optimality conditions

To obtain the expressions relating the primal and dual variables of Model 4, we can represent the optimization Model 4 as its equivalent Lagrangian function $\mathcal{L}$ that combines its objective function with its constraints. The Lagrangian function of the coordination market 3.9 is given by:

$$\begin{aligned}\mathcal{L}=\sum_{a}\Bigg[& c_a+\pi^{\mathrm{imp}}p_a^{\mathrm{imp}}-\pi^{\mathrm{exp}}p_a^{\mathrm{exp}} \\ & +\lambda_a\left(P_a^{\mathrm{D}}-p_a-p_a^{\mathrm{imp}}+p_a^{\mathrm{exp}}\right) \\ & +\gamma_a\left(H_a^{\mathrm{D}}-h_a-\sum_{b\in\mathcal{T}_a}\left(\eta_{ba}^{\mathrm{tr}}h_{ba}^{(a)}-h_{ab}^{(a)}\right)\right) \\ & +\sum_{b\in\mathcal{T}_a}\chi_{ab}\left(h_{ab}^{(b)}-h_{ab}^{(a)}\right) \\ & +\sum_{l}\mu_{al}\left(p_aK_{al}^{\mathrm{p}}+h_aK_{al}^{\mathrm{h}}-K_{al}^{0}\right) \\ & +\overline{\kappa}_{ab}\left(h_{ab}^{(a)}-\overline{H}_{ab}^{\mathrm{tr}}\right)+\overline{\psi}_a\left(p_a^{\mathrm{imp}}-\overline{P_a}\right)+\overline{\phi}_a\left(p_a^{\mathrm{exp}}-\overline{P_a}\right)\Bigg].\end{aligned} \tag{3.10}$$

The Karush-Kuhn-Tucker (KKT) conditions for the optimality of the Lagrangian function (3.10) are: primal feasibility, dual feasibility, complementary slackness (3.11), and stationarity (3.12). These set of conditions can be used to derive the analytical expressions that relate the operational and dual variables. The derived analytical expressions provide an understanding of the technical variables influence on the price formation.

Primal feasibility

The heat market model (3.9) is known as the *primal* optimization model. At the optimum, the constraints of the area coordination model, (3.9b)–(3.9g), must be satisfied. In other words, the optimal operation point must be feasible.

Dual feasibility

The dual variables associated with the inequalities must be greater or equal to zero, i.e., $\mu_{al},\ \overline{\kappa}_{ab},\ \overline{\psi}_a,\ \overline{\phi}_a \geq 0$.

Complementary slackness

The product of the dual variables with their respective inequalities in standard form must be equal to zero:

$$0 = \mu_{al}\big(p_a K^{\mathrm{p}}_{al} + h_a K^{\mathrm{h}}_{al} - K^{0}_{al}\big), \qquad \forall a, l \tag{3.11a}$$

$$0 = \overline{\kappa}_{ab}\Big(h^{(a)}_{ab} - \overline{H}^{\mathrm{tr}}_{ab}\Big), \qquad \forall a \tag{3.11b}$$

$$0 = \overline{\psi}_a\big(p^{\mathrm{imp}}_a - \overline{P_a}\big), \qquad \forall a \tag{3.11c}$$

$$0 = \overline{\phi}_a\big(p^{\mathrm{exp}}_a - \overline{P_a}\big), \qquad \forall a. \tag{3.11d}$$

The value of the dual variables associated with the inequalities values could become non-zero only when their respective inequalities are binding. Therefore, $\mu_{al}\geq 0$ if area a is operating at its operational bound l, i.e., if $p_a K^{\mathrm{p}}_{al} + h_a K^{\mathrm{h}}_{al} = K^{0}_{al}$.

Stationarity:

In a convex optimization problem, the optimum is an stationary point of the Lagrangian function $\mathcal{L}$. Therefore, at the optimum the gradient of the Lagrangian function $\mathcal{L}$ (3.10) equals zero.

$$\nabla\mathcal{L} = \overrightarrow{0}. \tag{3.12}$$

The gradient $\nabla\mathcal{L}$ can be split in terms of the primal variables so as to derive them analytically as:

$$0=\frac{\partial\mathcal{L}}{\partial p_a} = 2C^{\mathrm{p}}_{2,a}p_a+C^{\mathrm{p}}_{1,a}+C^{\mathrm{hp}}_{a}h_a-\lambda_a+\sum_l \mu_{al}K^{\mathrm{p}}_{al}, \quad \forall a \tag{3.12a}$$

$$0=\frac{\partial\mathcal{L}}{\partial h_a} = 2C^{\mathrm{h}}_{2,a}h_a+C^{\mathrm{h}}_{1,a}+C^{\mathrm{hp}}_{a}p_a-\gamma_a+\sum_l \mu_{al}K^{\mathrm{h}}_{al}, \quad \forall a \tag{3.12b}$$

$$0=\frac{\partial\mathcal{L}}{\partial h^{(a)}_{ab}} = \gamma_a-\chi_{ab}+\overline{\kappa}_{ab}, \quad \forall a \tag{3.12c}$$

$$0=\frac{\partial\mathcal{L}}{\partial h^{(a)}_{ba}} = \eta^{\mathrm{tr}}_{ba}\gamma_a-\chi_{ba}, \quad \forall a \tag{3.12d}$$

$$0=\frac{\partial\mathcal{L}_a}{\partial p^{\mathrm{imp}}_a} = \pi^{\mathrm{imp}}_a-\lambda_a+\psi_a, \quad \forall a \tag{3.12e}$$

$$0=\frac{\partial\mathcal{L}_a}{\partial p^{\mathrm{exp}}_a} = -\pi^{\mathrm{exp}}_a+\lambda_a+\phi_a \quad \forall a. \tag{3.12f}$$

As an example, the terms λ_a and γ_a respectively represent the marginal generation cost of the areas with respect to their electricity and heat generation, namely the extra cost of generating one additional unit of electricity and heat; and their values are given by

$$\lambda_a = 2C^{\mathrm{p}}_{2,a}p_a+C^{\mathrm{p}}_{1,a}+C^{\mathrm{hp}}_{a}h_a+\sum_l \mu_{al}K^{\mathrm{p}}_{al}, \quad \forall a \tag{3.13a}$$

$$\gamma_a = 2C^{\mathrm{h}}_{2,a}h_a+C^{\mathrm{h}}_{1,a}+C^{\mathrm{hp}}_{a}p_a+\sum_l \mu_{al}K^{\mathrm{h}}_{al}, \quad \forall a. \tag{3.13b}$$

Note how the coupling of heat and power generation is reflected in the marginal generation costs (3.13a) and (3.13b). The heat generation h_a influences the marginal electric generation cost in (3.13a) and the electricity generation affects the marginal heating costs in (3.13b). In an area without cogeneration units, the heat generation does not affect the marginal electricity cost nor the electricity generation the marginal heating cost, since C^{hp}_a=0.

3.3.2 Heat transfer price

The optimal operation point of Model 4 satisfies the optimality conditions presented in Section 3.3.1. Therefore, from the KKT stationarity conditions at the optimum

(3.12), we can now derive the prices χ_{ab} for the heat transfer as

$$\chi_{ab} = \gamma_a + \overline{\kappa}_{ab}. \tag{3.14}$$

The heat export price given by expression (3.14) can be understood as follows: in case of exporting heat without reaching the transfer limits, the export price χ_{ab} is equal to the local heat price γ_a.[2] If the maximum transfer capacity is reached, then the price is increased by $\overline{\kappa}_a$.

Additionally, from the derivative of the Lagrangian by the imported heat $h_{ba}^{(a)}$ (3.12d), the import price depends on the local heating price of the receiving area and the interconnection efficiency:

$$\chi_{ab} = \eta_{ab}^{\text{tr}} \gamma_b \tag{3.15}$$

Expression (3.15) indicates that the price paid to area a for exporting heat to b is dependent on the local heat price at b and the interconnection efficiency between them. Therefore, if two areas are exporting heat to area b and their transfer efficiency to b is equal, they will both be paid at the same price, independently of their costs curves and transferred quantities. Analogously, if one area has a lower interconnection efficiency with area b, it will be paid at a lower price than those with higher efficiency to compensate for the transfer losses.

3.3.3 Competitive equilibrium

The prices χ_{ab} obtained in (3.14) can be used to organize the centralized heat transfer market. The centralized heat transfer market defines a competitive equilibrium if by setting a heat transfer price π_{ab} [69]:

1. The market clears at the optimal values $h_{ab}^{(a),*} = h_{ab}^{(b),*},\ \forall a, b.$

2. Each area a maximizes its profit under an export payment of $\Pi_a^{\text{exp}} = \sum_{b \in \mathcal{T}_a} \pi_{ab} h_{ab}^{(a),*}$

[2] The heat consumption prices inside the areas and the export prices are not flat tariffs. These prices are influenced by the demand levels and transfer quantities as seen in expressions (3.13a) and (3.13b).

and import payment of $\Pi_a^{\text{imp}} = \sum_{b\in\mathcal{T}_a} \pi_{ba} h_{ba}^{(a),*}$, i.e., the market is incentive-compatible.

To prove that the use of π_{ab} as the heat transfer price leads to a competitive equilibrium, let us consider the area profit-maximization problem (APMP) given in Model 5.

Model 5 Area Profit-maximization Problem (APMP) [QP]

$$\max. \quad \overbrace{\sum_{b\neq a} \pi_{ab} h_{ab}^{(a)} + \pi_a^{\text{p}} P_a^{\text{D}} + \pi_a^{\text{h}} H_a^{\text{D}} + \pi_a^{\text{exp}} p_a^{\text{exp}}}^{\text{Revenue}} - \underbrace{\left(c_a + \sum_{b\neq a} \pi_{ba} h_{ba}^{(a)} \right) + \pi_a^{\text{imp}} p_a^{\text{imp}}}_{\text{Cost}} \tag{3.16a}$$

subject to

$$c_a = C_{2,a}^{\text{p}} p_a^2 + C_{1,a}^{\text{p}} p_a + C_{2,a}^{\text{h}} h_a^2 + C_{1,a}^{\text{h}} h_a + C^{\text{hp}} h_a p_a + C_{0,a}, \tag{3.16b}$$

$$(\lambda_a): \quad P_a^{\text{D}} = p_a + p_a^{\text{imp}} - p_a^{\text{exp}}, \tag{3.16c}$$

$$(\gamma_a): \quad H_a^{\text{D}} = h_a + \sum_{b\in\mathcal{T}_a} \left(\eta_{ba}^{\text{tr}} h_{ba}^{(a)} - h_{ab}^{(a)} \right), \tag{3.16d}$$

$$(\mu_{al}): \quad p_a K_{al}^{\text{p}} + h_a K_{al}^{\text{h}} \leq K_{al}^0, \tag{3.16e}$$

$$(\overline{\kappa}_a): \quad 0 \leq h_{ab}^{(a)} \leq \overline{H}_{ab}^{\text{tr}}, \qquad \forall b \in \mathcal{T}_a \tag{3.16f}$$

$$(\overline{\psi}_a): \quad 0 \leq p_a^{\text{imp}} \leq \overline{P_a}, \tag{3.16g}$$

$$(\overline{\phi}_a): \quad 0 \leq p_a^{\text{exp}} \leq \overline{P_a}. \tag{3.16h}$$

In the APMP (3.16), it is of no importance for area a that its local copy of $h_{ab}^{(a)}$ matches that of the adjacent areas, i.e., the continuity constraint (3.9f) does not appear in the APMP. This is because it is the responsibility of the centralized market operator to guarantee the heat transfer continuity between areas.

Let $\mathcal{L}_a$ be the Lagrangian function of the APMP (3.16), then the optimal stationarity conditions of the APMP are:

$$0 = \frac{\partial \mathcal{L}_a}{\partial p_a} = -\pi_a^{\text{p}} + 2C_{2,a}^{\text{p}} p_a + C_{1,a}^{\text{p}} + C_a^{\text{hp}} h_a + \sum_l \mu_{al} K_{al}^{\text{p}}, \tag{3.17a}$$

$$0 = \frac{\partial \mathcal{L}_a}{\partial h_a} = -\pi_a^{\text{h}} + 2C_{2,a}^{\text{h}} h_a + C_{1,a}^{\text{h}} + C_a^{\text{hp}} p_a + \sum_l \mu_{al} K_{al}^{\text{h}}, \tag{3.17b}$$

$$0=\frac{\partial \mathcal{L}_a}{\partial h_{ab}^{(a)}}= -\pi_{ab}+\gamma_a+\overline{\kappa}_{ab}, \tag{3.17c}$$

$$0=\frac{\partial \mathcal{L}_a}{\partial h_{ba}}= \pi_{ba}-\eta_{ba}^{\mathrm{tr}}\gamma_a, \tag{3.17d}$$

$$0=\frac{\partial \mathcal{L}_a}{\partial p_a^{\mathrm{imp}}}= \pi_a^{\mathrm{imp}}-\lambda_a+\overline{\psi}_a, \tag{3.17e}$$

$$0=\frac{\partial \mathcal{L}_a}{\partial p_a^{\mathrm{imp}}}= -\pi_a^{\mathrm{exp}}+\lambda_a+\overline{\phi}_a. \tag{3.17f}$$

From (3.17c) and (3.17d), we obtain:

$$\pi_{ab}=\gamma_a+\overline{\kappa}_{ab}, \tag{3.18a}$$

$$\pi_{ba}=\gamma_a\eta_{ba}^{\mathrm{tr}}. \tag{3.18b}$$

Respectively comparing expressions (3.18) and (3.18b) with (3.12c) and (3.12d), we obtain that:

$$\pi_{ab}=\chi_{ab}, \quad \forall a,b\in\mathcal{T}_a. \tag{3.19}$$

From (3.19), if $h_{ab}^{(a)}{=}h_{ab}^{(a),*},\ \forall a,b\in\mathcal{T}_a$, it follows that $\pi_{ab}{=}\chi_{ab}^{*},\ \forall a,b\in\mathcal{T}_a$. Therefore, $\{h_{ab}^{(a),*},\ \pi_{ab}\}$ maximize (3.16) and solve Model 4; proving that the established heat transfer market leads to a competitive equilibrium.

3.3.4 Transfer price dependence on interconnection capacity

The maximum transfer capacity between areas can influence not only the heat transfer price, but also the internal area prices. Figure 3.5(a) presents two areas with different price curves and possible transfer scenarios. The x–axes represents the area heat generation, while the y–axes the associated heat price. In scenario (I) there is no transfer allowed between areas and their generation matches the internal demand. Based on this operation point, the shaded areas represent the range in which the generation can change subject to the transfer capacity. Note that in this scenario the heating price at area a is lower than that of area b. Therefore it would be beneficial for both areas to have heat exchanged from area a to b, since area a

would increase its revenue and area b reduce its costs.

Scenario (II) presents an export scenario, from area a to b, at a value that allows for the prices at area a and b to become equal. This is the maximum transfer value that enables the economic feasibility of the transaction. Heat export increases the required generation, resulting in the increase of heating costs γ_a. Similarly, an importing area reduces its heating price by generating less. Thus, the optimal amount of transferred heat would be one that allows the prices in both areas to reach the same value. This corresponds to the fact that further heat exchange would reduce the heating price of the importing area and increase that of the price of the exporting one, creating a price mismatch in the opposite direction and making the exchange economically inefficient.

If the export quantity was increased to the maximum transfer limit, scenario (III), the price in area a would rise above that of area b. Therefore, the maximum transferable quantity is not only dependent on the technical limits, but also on the price difference between the areas. The exported quantity will increase until the prices in the areas are matched or the technical transfer limit is reached. In case that the transfer limit is reached, there will be a price difference Δ between the areas, scenario (II) of Figure 3.5(b). It must be noted that the quantities transferred and their prices are dependent on the requested area demands, since a change in demand would shift the operation points of scenario (I) in Figures 3.5(a) and 3.5(b).

3.3.5 Transfer price dependence on interconnection efficiency

Due to the losses in the interconnection pipe, area b receives a quantity of $\eta_{ab}^{\text{tr}} h_{ab}$ from the originally transferred quantity h_{ab} from area a. Therefore, we can define an effective import price γ_{ab}^{eff} of an interconnection as the perceived export price after

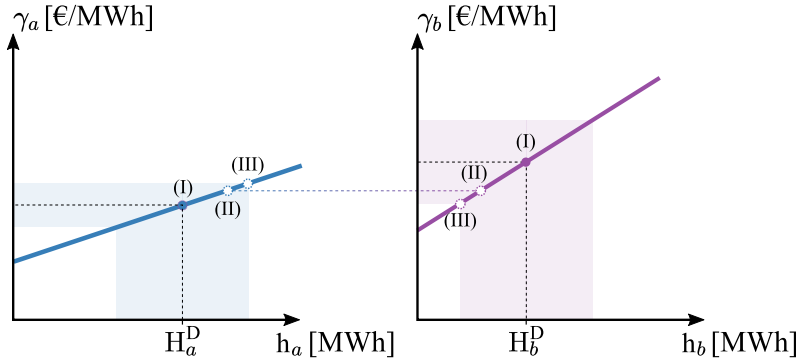

(a) General model of two-area interconnection: (I) before transfer, from area a to b (II) below maximum capacity, and (III) at maximum capacity.

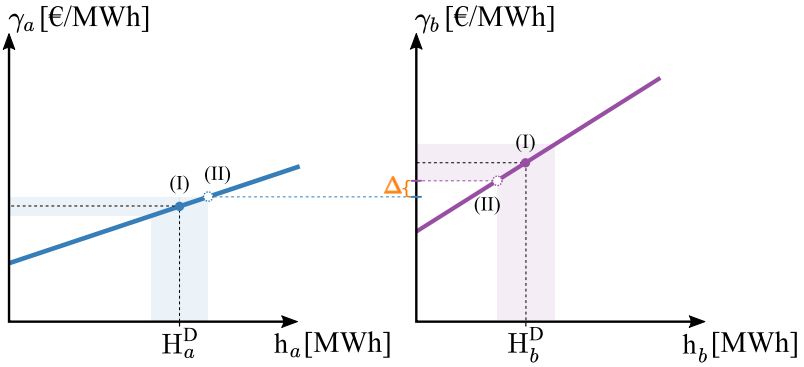

(b) Constrained model of two-area interconnection: (I) before transfer, and (II) transfer from area a to b at maximum capacity.

Figure 3.5: Effect of transfer capacity on heat transfer quantities and prices: (a) with sufficient capacity, and (b) with insufficient capacity. η_{ab}^{tr}=1

the losses have been accounted for [3]:

$$\gamma_{ab}^{\text{eff}} = \frac{h_{ab}^{\text{sent}}\gamma_a}{h_{ab}^{\text{received}}} = \frac{h_{ab}\gamma_a}{h_{ab}\eta_{ab}^{\text{tr}}}, = \frac{\gamma_a}{\eta_{ab}^{\text{tr}}}, \quad \forall a, b \in \mathcal{T}_a. \tag{3.20}$$

The effective import price γ_{ab}^{eff} thus increases for lower interconnection efficiencies η_{ab}^{tr}. The influence of the interconnection efficiency on the effective import price is shown in Figure 3.6 through three scenarios: (I) η_{ab}^{tr}=1, (II) η_{ab}^{tr}=0.9, and (III) η_{ab}^{tr}=0.7. In scenario (I) the effective import price matches the heating price in area b and the exported quantity equals that received.

At a transfer efficiency η_{ab}^{tr}=0.9, scenario (II), the quantity of heat transferred is

[3]The steady-state pipeline heat losses are approximately independent to mass flow rates in practical applications, while being mostly dependent on pipeline inlet temperatures [115]. Therefore, the pipeline losses can be controlled by managing the pipe's inlet temperature.

reduced and its price increased. At this efficiency level, the amount of heat exported from area a is lower than that received by area b. The changes in the quantity and price of heat transferred reflect the losses in the transfer process.

When the interconnection efficiency is too low, as in scenario (III) with η_{ab}^{tr}=0.7, the effective import price without transfer becomes greater than the heat price in area b. Therefore, even though the price in area a is lower than that of area b, the losses in the interconnection pipeline make it appear greater and make the transfer economically inefficient.

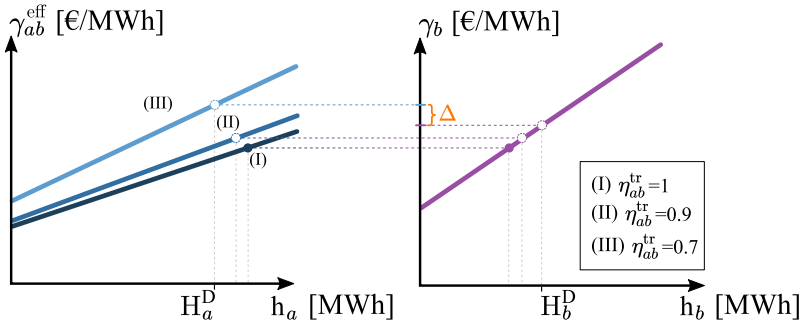

Figure 3.6: Influence of interconnection efficiency η_{ab}^{tr} on heat transfer.

There are three possible relations between local heat prices and effective import prices: (I) $\gamma_b<\gamma_{ab}^{\text{eff}}$, (II) $\gamma_b=\gamma_{ab}^{\text{eff}}$, and (III) $\gamma_b>\gamma_{ab}^{\text{eff}}$; as shown in Figure 3.7.

In the first scenario, the pipeline efficiency is too low, $\eta_{ab}^{\text{tr}}<\eta_{ab}^{\text{in}}$, resulting in great transfer losses. Thus, the effective import price is greater than the heating cost at area b and there is no heat transfer. In region (I) as the interconnection efficiency increases, the effective import price decreases. However, the heating price at area b remains constant since there is no transfer that leads to generation reduction in the area.

Once the efficiency increases above a certain value, $\eta_{ab}^{\text{in}}\leq\eta_{ab}^{\text{tr}}\leq\eta_{ab}^{\text{sat}}$, the losses in the interconnection are reduced to a point in which the transfer becomes economically feasible. Along region (II) the effective import price matches the heat price at area b. With the increase of efficiency, both prices are reduced, since less generation is required in area b.

As the transfer efficiency increases beyond η_{ab}^{in}, the quantity of transferred heat also increases. This increase in exported heat continues until reaching the intercon-

nection capacity, when the transfer efficiency equals η_{ab}^{sat}. After this point, region (III) with $\eta_{ab}^{\text{sat}}<\eta_{ab}^{\text{tr}}$, the heat pipeline is saturated and the heat transfer equals the interconnection capacity. Once the interconnection is saturated, there appears a price difference between the effective import price and the heating price in area b. This price difference, gives an economic signal that the transfer capacity could be increased to further reduce the operational costs.

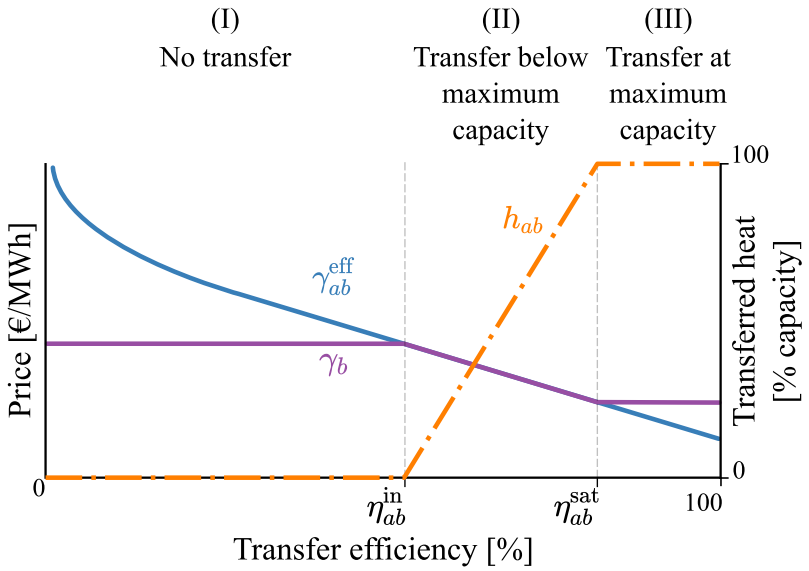

Figure 3.7: Possible transfer scenarios based on the interconnection efficiency η_{ab}^{tr}.

3.4 Decentralized thermal coordination

It is not always possible to solve the area coordination problem in a centralized way. A centralized optimization would require complete knowledge of the internal area characteristics, which might not be desirable for cases in which two independent microgrids decide to exchange heat while preserving their private information. In such cases it is necessary to agree on the transferred heat and its price in a decentralized manner, with each area optimizing its own system while exchanging only the information related to the transfer quantity and its price.

For this purpose, we would like to split Model 4 into area sub-problems, so that each area optimizes its own operation in a decentralized manner without sharing their full system's information to third parties. Constraint (3.9f) binds the areas

together. Therefore, we cannot directly solve the problem independently on each area without accounting for the impact of the continuity of heat transfer between the areas. Constraint (3.9f) is called the complicating or coupling constraint of the master area coordination problem.

With the knowledge that (3.9f) is the complicating constraint, Model 4 can be written in compact form as:

$$\min. \quad \sum_{a} c_a(x_a) \tag{3.21a}$$

$$(\chi_{ab}): \quad h_{ab}^{(a)} = h_{ab}^{(b)}, \qquad \forall a, b \in \mathcal{T}_a \tag{3.21b}$$

$$g_a(x_a) \leq 0, \qquad \forall a. \tag{3.21c}$$

where x_a are the state variables for each microgrid of the global system. x_a contains information on microgrid a's control and dependent variables. Constraint (3.21b) represents the heat transfer continuity equation (3.9f). Constraint (3.21c) includes the cost characterization (3.9b), energy balances (3.9c)–(3.9d), generation characterization (3.9e), and limits over dependent and control variables (3.9g)–(3.9i). The set of constrains (3.21c) represents both equality and inequality constraints.

Problem (3.21) can be rewritten based on its reduced Lagrangian function as:

$$\min. \quad \sum_{a} \left(c_a(x_a) + \sum_{b \in \mathcal{T}_a} \left[\chi_{ab} \left(h_{ab}^{(a)} - h_{ab}^{(b)} \right) + \chi_{ba} \left(h_{ba}^{(b)} - h_{ba}^{(a)} \right) \right] \right) \tag{3.22a}$$

$$\text{s.t.} \quad g_a(x_a) \leq 0, \qquad \forall a. \tag{3.22b}$$

Problem (3.22) is obtained by adding to the objective function the multiplication of the the exchange coordination equality (3.21b) in its standard form (equal to zero) times its dual variable χ_{ab}. Note that at the optimum the exchange coordination equality (3.21b) holds. Thus, the term $h_{ab}^{(a)} - h_{ab}^{(b)} = 0$ and does not affect the optimal objective value.

Given its convexity and decomposable structure, i.e., for each area a the copies of the heat transfer from other areas $h_{ab}^{(b)}$ can be fixed yielding independent operational problems, problem (3.22a) can be solved in a distributed and iterative manner through the alternating direction method of multipliers (ADMM) [116]. For

the coordination of more than 2 areas, the use of the traditional ADMM, introduced in [117, 118] and extensively analysed in [116], does not guarantee converge to the optimal solution for problems with three or more blocks (areas) [119]. The uncertainty of obtaining the global optimum in the exchange market is not desired since it would lead to inefficient heat transfers between the areas. Resulting in suboptimal transfer quantities and prices. Therefore, we employ a Jacobi–Proximal ADMM (JP–ADMM), introduced by Deng *et al.* [120], to model the distributed solution of the coordinated market. The JP–ADMM is suitable for the solution of the coordination market in a distributed manner with convergence assurance.

In the JP–ADMM, in every iteration each area optimizes its own sub-problem and exchanges with the other areas the optimal values of its local copy for the transferred heat $h_{ab}^{(a)}$. With the optimized values for $h_{ab}^{(a)}$, the transfer prices χ_{ab} are calculated. If the calculated transfer prices do not alter the optimal exchanged heat, the problem has been solved; else, the areas optimize their sub-problems once more with the new transfer prices and the iterations continue until optimal exchange quantities and prices are obtained.

We present below the decentralized operation of the heat market under the JP–ADMM algorithm, detailing the steps of the iterative procedure and the calculation of its parameters. The steps of the JP–ADMM are summarized in Figure 3.8 and are described as follows:

Step 0 – Initialization and distribution of parameters and variables:

In the initial iteration, k=0, the coordination parameters ϵ_s>0, ρ>0, $s_{ab}^{k=0} \gg \epsilon$ and the area variables $h_{ab}^{(a),k=0}, h_{ba}^{(a),k=0}, \chi_{ab}^{k=0}, \chi_{ba}^{k=0}$ are initialized. The allowed convergence gap is given by ϵ, the step-size by ρ and the change of the transfer-price update by s_{ab}^{k}. The initialized variables and coordination parameters are distributed to all areas.

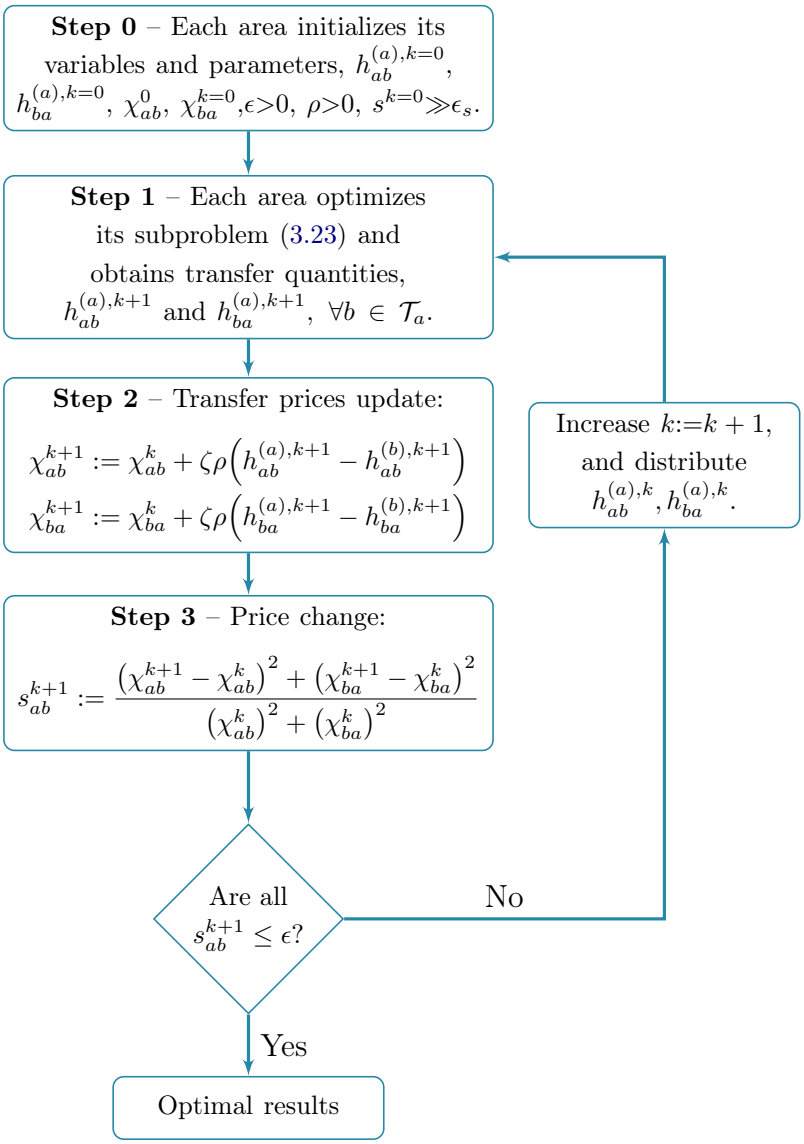

Figure 3.8: Coordination between the areas with the Jacobi–proximal alternating direction method of multiplies (JP–ADMM).

Step 1 – Area subproblem optimization:

In the JP–ADMM each area optimizes its own subproblem, Model 6, (3.23), by fixing during iteration k the values of χ_{ab}=χ_{ab}^{k} and χ_{ba}=χ_{ab}^{k} $\forall a, b \in \mathcal{T}_a$, as well as those of the heat import and export of the interconnecting areas ($h_{ab}^{(b)}$=$h_{ab}^{(b),k}$ and $h_{ba}^{(b)}$=$h_{ba}^{(b),k}$).

In the area subproblem (3.23), the terms with the superscript k indicate that these variables are set as constants during the k^{th} iteration. The term $(\rho/2)\left\|R_{ab}^{k}\right\|_2^2$ represents the penalty for deviations on the heat transfer continuity between areas

Model 6 JP–ADMM Area Sub-problem: $\boldsymbol{k}^{th}$ iteration [QP]

$$\min. \quad \sum_a \Bigg[\Big(c_a + \pi_a^{\text{imp}} p_a^{\text{imp}} - \pi_a^{\text{exp}} p_a^{\text{exp}}\Big) - \sum_{b\in\mathcal{T}_a} \left(\boldsymbol{\chi}_{\boldsymbol{ba}}^{\boldsymbol{k}} h_{ba}^{(a)} - \boldsymbol{\chi}_{\boldsymbol{ab}}^{\boldsymbol{k}} h_{ab}^{(a)} + \frac{\rho}{2} \big\| R_{ab}^k \big\|_2^2 \right) \Bigg] + \frac{1}{2} \|\mathbf{H}_a - \mathbf{H}_a^k\|_{\mathbf{P}_a}^2 \tag{3.23a}$$

subject to

$$c_a = C_{2,a}^{\text{p}} p_a^2 + C_{1,a}^{\text{p}} p_a C_{2,a}^{\text{h}} h_a^2 + C_{1,a}^{\text{h}} h_a + C^{\text{hp}} h_a p_a + C_{0,a}, \quad \forall a \tag{3.23b}$$

$$(\lambda_a): \quad P_a^{\text{D}} = p_a + p_a^{\text{imp}} - p_a^{\text{exp}}, \quad \forall a \tag{3.23c}$$

$$(\gamma_a): \quad H_a^{\text{D}} = h_a + \sum_{b\in\mathcal{T}_a} \left(\eta_{ba}^{\text{tr}} h_{ba}^{(a)} - h_{ab}^{(a)} \right), \quad \forall a \tag{3.23d}$$

$$(\mu_{al}): \quad p_a K_{al}^{\text{p}} + h_a K_{al}^{\text{h}} \leq K_{al}^0, \quad \forall a \tag{3.23e}$$

$$(\overline{\kappa}_a): \quad 0 \leq h_{ab}^{(a)} \leq \overline{H}_{ab}^{\text{tr}}, \quad \forall a \tag{3.23f}$$

$$(\overline{\psi}_a): \quad 0 \leq p_a^{\text{imp}} \leq \overline{P_a}, \quad \forall a \tag{3.23g}$$

$$(\overline{\phi}_a): \quad 0 \leq p_a^{\text{exp}} \leq \overline{P_a}, \quad \forall a. \tag{3.23h}$$

for the k^{th} iteration. The vector $R_{ab}^k = \left[h_{ab}^{(a)} - h_{ab}^{(b),k}, h_{ba}^{(b),k} - h_{ba}^{(a)} \right]^\top$ collects the residuals of the transfer between areas a and b at iteration k.[4] The term $\left\| R_{ab}^k \right\|_2^2$ becomes zero once the transferred quantities have been agreed between the areas.

The final term in the objective function, $\frac{1}{2}\|\mathbf{H}_a - \mathbf{H}_a^k\|_{\mathbf{P}_a}^2$, is a proximal term that prevents the divergence between iterations [120]. $\mathbf{H}_a$ is the vector containing the quantities of heat transfer: $\mathbf{H}_a = \left[h_{ab_1}^{(a)}, h_{b_1 a}^{(a)}, ..., h_{ab_{|\mathcal{T}_a|}}^{(a)}, h_{b_{|\mathcal{T}_a|} a}^{(a)} \right]^\top$, where $b_t \in \mathcal{T}_a$ are the areas connected to a. $\mathbf{P}_a \succeq 0$ is a symmetric and positive semi-definite matrix, and the operator $\|Y_a\|_{\mathbf{P}_a}^2$ is defined as $\|Y_a\|_{\mathbf{P}_a}^2 := Y_a^\top \mathbf{P}_a Y_a$.

The values of $\mathbf{P}_a$ that guarantee convergence are given by:

$$\mathbf{P}_a = \tau_a \mathbf{I}, \quad \forall a \tag{3.24a}$$

where

$$\tau_a > \rho \left(\frac{N}{2-\zeta} - 1 \right) \|\mathbf{T}_a\|_2^2, \quad \forall a. \tag{3.24b}$$

N is the total number of areas and $\zeta > 0$ is the damping parameter for the update

[4] The l^2–norm of a vector Y, also known as the Euclidean norm, denoted by $\|X\|_2$ is calculated as $\|Y\|_2 = \left(\sum_{i=1}^n |y_i|^2 \right)^{1/2}$. Thus, in expression (3.23a) $\left\| R_{ab}^k \right\|_2^2 = \left(h_{ab}^{(a)} - h_{ab}^{(b),k} \right)^2 + \left(h_{ba}^{(b),k} - h_{ba}^{(a)} \right)^2$.

of the transfer prices χ_{ab} between iterations. Given that $\mathbf{T}_a$ is the transfer vector for the local copies of the heat import and export variables for area a, its elements are 1 for each of the export variables and -1 for the import ones. Therefore the value of $\|\mathbf{T}_a\|_2^2$ can be calculated by:

$$\|\mathbf{T}_a\|_2^2 = \mathbf{T}_a^\top \mathbf{T}_a = \sum_{b=1}^{|\mathcal{T}_a|} \big(|1|^2 + |-1|^2\big) = \sum_{b=1}^{|\mathcal{T}_a|} 2 = 2|\mathcal{T}_a|, \quad \forall a \tag{3.24c}$$

Since expression (3.24c) holds for every area[5], we can calculate the value of τ_a by transforming inequality (3.24b) into:

$$\tau_a > 2|\mathcal{T}_a|\rho\left(\frac{N}{2-\zeta} - 1\right), \qquad \forall a. \tag{3.24d}$$

Finally, the constraints of the area subproblem, (3.23b) – (3.23h), represent the internal area constraints discussed in Section 3.2.

With Model 6 each area optimizes its operation, calculating $h_{ab}^{(a)}$ and $h_{ba}^{(a)}$, $\forall b \in \mathcal{T}_a$. The obtained transfer quantities are set as the local area copies for the next iteration, i.e., $h_{ab}^{(a),k+1} := h_{ab}^{(a)}$ and $h_{ba}^{(a),k+1} := h_{ba}^{(a)}$, $\forall b \in \mathcal{T}_a$.

Step 2 – Variables distribution and price update:

Once each area has optimized its own subproblem, the obtained transfer values are distributed among them. With the new values of $h_{ab}^{(a),k+1}$ and $h_{ab}^{(b),k+1}$, each area updates χ_{ab}^{k+1} and χ_{ba}^{k+1} with:

$$\chi_{ab}^{k+1} = \chi_{ab}^{k} + \zeta\rho(h_{ab}^{(a),k+1} - h_{ab}^{(b),k+1}), \quad \forall a, b \in \mathcal{T}_a \tag{3.25a}$$

$$\chi_{ba}^{k+1} = \chi_{ba}^{k} + \zeta\rho(h_{ba}^{(a),k+1} - h_{ba}^{(b),k+1}), \quad \forall a, b \in \mathcal{T}_a. \tag{3.25b}$$

[5]For example, consider the case where there are three areas $\{1, 2, 3\}$ with connection between areas 1–3 and 2–3, but not between 1–2. For the number of area interconnections we obtain that $|\mathcal{T}_1|=|\mathcal{T}_2|=1$ and $|\mathcal{T}_3|=2$. The transfer vectors for the local copies $\mathbf{T}_a$ are: $\mathbf{T}_1=\mathbf{T}_2=[1,-1]^\top$ and $\mathbf{T}_3=[1,-1,1,-1]^\top$. Consequently, $\|\mathbf{T}_1\|_2^2=\|\mathbf{T}_2\|_2^2=[1,-1][1,-1]^\top=1^2+(-1)^2=2=2|\mathcal{T}_1|=2|\mathcal{T}_2|$; and $\|\mathbf{T}_3\|_2^2=[1,-1,1,-1][1,-1,1,-1]^\top=1^2+(-1)^2+1^2+(-1)^2=4=2|\mathcal{T}_3|$.

Step 3 – Convergence check:

The changes in the transfer prices after iteration k are computed by:

$$s_{ab}^{k+1} = \frac{\left(\chi_{ab}^{k+1} - \chi_{ab}^{k}\right)^2 + \left(\chi_{ba}^{k+1} - \chi_{ba}^{k}\right)^2}{\left(\chi_{ab}^{k}\right)^2 + \left(\chi_{ba}^{k}\right)^2}, \quad \forall a, b \in \mathcal{T}_a. \tag{3.25c}$$

The distributed optimization has converged and the optimal values have been obtained when $s_{ab}^{k} \leq \epsilon$; else, the iterations continue and $k{:=}k+1$.

3.5 Numerical tests

In this section numerical tests are conducted to illustrate the area coordination for an hourly time step in a heat market. These test cases are divided into two main sub-cases: i) a two-area, and ii) a three-area system. In the two-area system, the conditions for heat transfer between areas are discussed, i.e., price difference between areas, electricity import prices and interconnection capacity. Additionally, the iterative decentralized coordination procedure is analyzed. For the 3-area sub-case, the effects of the interconnection topology, capacities, and transfer efficiencies are examined. The system operational data, assumed parameters and prices, adapted from [121] and [122] is presented in Table 3.1. Each of the areas is represented as having a convex operating region, Figure 3.9, which is analogous to that of an extraction condensing steam turbine. The simulations are performed using the modeling software Julia 1.5.3 [123], with the optimization package JuMP [124], and Gurobi 9.1.1 [98] as solver. The test machine features an Intel(R) Core(TM) i7-10710U CPU @ 1.10 GHz, 1608 MHz, 6 Cores, 12 Logical Processors.

3.5.1 Two-area case

In order to study the conditions for heat transfer between areas, a two-area case is devised. The operating costs and heat exchange of both areas 1 and 2 are compared when they are both with and without interconnection.

During the independent operation shown in Figure 3.10(a), i.e., without heat transfer, the internal heat prices in areas 1 and 2 resultant of their optimal inde-

Table 3.1: Test System Data

	Area 1	Area 2	Area 3	Units
P_a^{D}	200	70	80	MWh
H_a^{D}	125	95	30	MWh
$C_{2,a}^{\mathrm{p}}$	0.0345	0.0435	0.072	€/MWh^2
$C_{1,a}^{\mathrm{p}}$	14.5	36	20	€/MWh
$C_{2,a}^{\mathrm{h}}$	0.030	0.027	0.020	
$C_{1,a}^{\mathrm{h}}$	4.20	0.60	2.34	€/MWh
C_a^{hp}	0.031	0.011	0.040	€/MWh
$C_{0,a}$	26.50	12.50	15.65	€
π_a^{imp}	28	30	27.6	€/MWh
π_a^{exp}	22.4	24	22.1	€/MWh
$\overline{H}_{ab}^{\mathrm{tr}} = 10$ MW,		$\eta_{ab}^{\mathrm{tr}} = 0.9$		

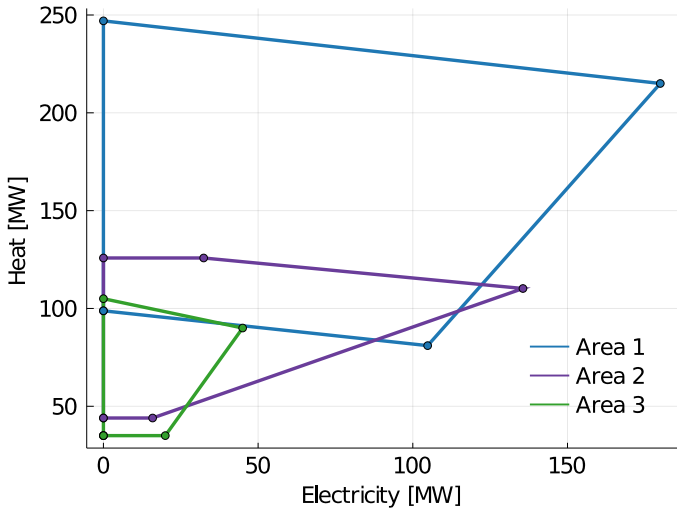

Figure 3.9: Equivalent Operating Regions of the Area Generation

pendent dispatch are respectively 16.02 and 5.73 €/MWh. The lower heat price in area 2 makes it convenient to transfer heat from area 2 to area 1. It must be noted that the electricity price at each area matches their respective import prices, since electric import from the grid occurs when the internal prices is greater or equal the import price. In this case, the marginal electricity generation cost of area 2 is greater than the electricity import price, allowing it to import all of the electricity necessary to cover its demand from the external network. Since the electric import capacity is not reached, both the local and import prices are equal.

Once a connection of 10 MW with a transfer efficiency of 0.9 is considered, Figure

3.10(b), the coordination results in area 2 exporting heat to area 1 at maximum capacity and at an optimal price of 14.05 €/MWh. The heating price in area 1 is reduced by 2.4%, from 16.02 to 15.61 €/MWh.

Since there exists a capacity saturation of the interconnection pipeline, there exists a price difference between areas 1's importing price of 14.05 €/MWh and its local heating price at 15.61 €/MWh. The congestion surplus for exporting at maximum capacity, $\overline{\kappa}_{21}$, is 7.78 €/MWh, i.e., 55.4 % of the export tariff. The congestion surplus is the difference between the transfer price and the local price at area 2, and serves as an indicator of the economic inefficiency of operating with a limited transfer capacity. In this case, an increase in the interconnection capacity would allow for the matching of the local and import prices.

Given that area 1 now has to produce 9 MWh of heat less, 10 MWh multiplied by the transfer efficiency of 0.9, it can reduce its heat generation. The lower heat generation translates into a heat price decrease, to 15.61€/MWh. Now area 1 can produce more electricity while maintaining its marginal generation price of electricity matching the network import price, at 28 €/MWh. Consequently, the quantity of electricity imported by area 1 is reduced.

By allowing heat transfer between the areas, their operational costs are reduced. Area 2 derives the greatest total cost reductions during the scheduled hourly exchange, 80.5 € versus 0.9 €, since it benefits from the lower internal heat prices. Area 1's heat import leads to a decrease in its heat generation, thus reducing its marginal electricity generation costs by (3.13a); resulting in higher internal electricity generation by area 1 and a consequently reduction of its electricity import from the external network. The increase of electricity generation by area 1 increases overall generation efficiency by working closer to its nominal conditions.

Decentralized two-area coordination

The decentralized Jacobi-proximal ADMM was used to solve the two-area system of Figure 3.10(b). To ensure global convergence, the parameters for the JP-ADMM discussed in Section 3.4 were set as ϵ=10^{-9}, ζ=1, ρ=0.01, and τ_1=τ_2=0.025. Areas 1 and 2 start the iterative procedure by setting their export quantities and

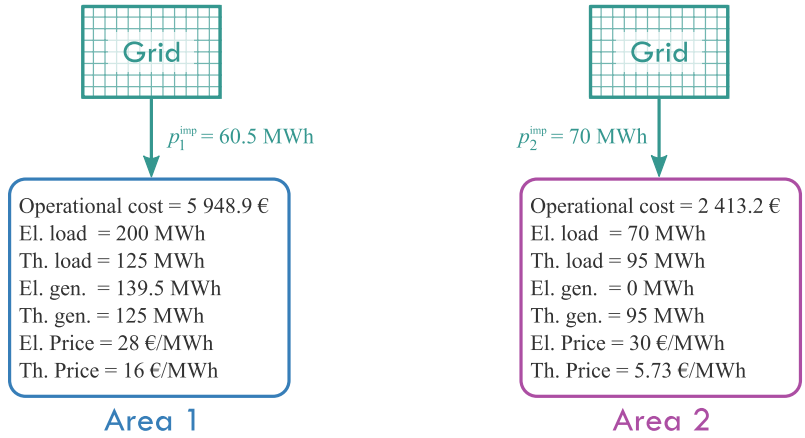

(a) Without interconnection

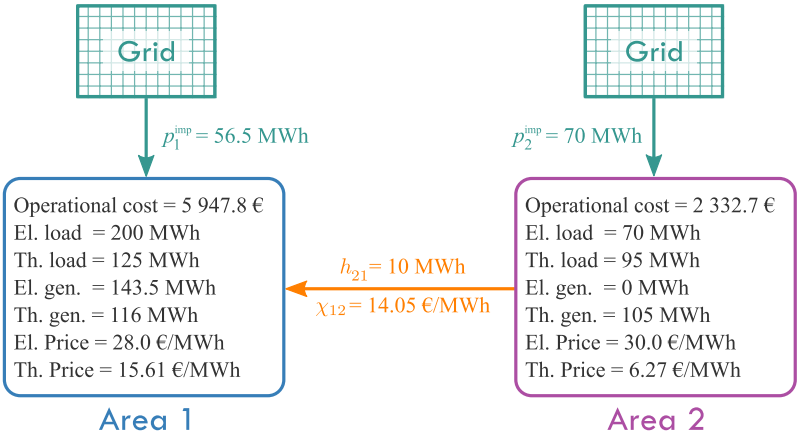

(b) With interconnection

Figure 3.10: Results of the two-area Coordination: (a) without, and (b) with interconnection.

prices respectively at 0 MWh and 0 €/MWh, as presented in Figures 3.11(a) and 3.11(b). After the first two iterations, it is determined that area 2 possesses the lowest marginal heat costs. Therefore, it is more convenient to export heat from area 2 to area 1. Consequently setting the export quantity for area 1 at zero and increasing that exported from area 2, Figure 3.11(a). Through the iterations, the areas must now agree on the transfer quantity and its price. This coordination is now done by increasing the transfer quantity until it reaches the maximum transfer capacity at 10 MWh. On the other hand, the export price is raised, Figure 3.11(b), up to the value when the effective import price equals the internal heat price of area 1 within the set tolerance.

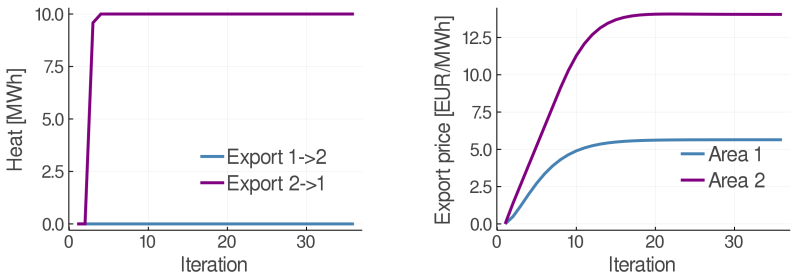

(a) Heat Transfer vs. Iteration (b) Transfer Price vs. Iteration

Figure 3.11: Results of the two-area ADMM Coordination: (a) amount of heat transferred, and (b) transferred heat price.

Sensitivity analysis: interconnection capacity

A sensitivity analysis for the maximum heat transfer capacity has been performed to exemplify the impact of the transfer capacity on the economic coordination between the areas.

The transferred heat increases as a function of the available capacity until the capacity reaches a transfer saturation point $\overline{H}^{\mathrm{tr,sat}}$, Figure 3.12(a). At $\overline{H}^{\mathrm{tr,sat}}$ the effective import price for area 2 (internal heat price over the transfer efficiency) matches the heat price of area 1, i.e., it costs the same to produce an extra MWh locally in area 1 than to import it, Figure 3.12(b) . Therefore, once the saturation capacity is reached, there are no economic benefits of increasing the transfer capacity. At the saturation capacity $\overline{H}^{\mathrm{tr,sat}}$, the following relationship holds $\gamma_1 = \eta_{21}^{\mathrm{tr}}\gamma_2$.

The economic benefits of the heat interconnection between the areas are represented in the reduction of the total areal operational costs, Figure 3.12(c). Given that area 2 experiences the highest price change, it obtains higher costs reductions than area 1.

Sensitivity analysis: electricity import price

As with the maximum transfer capacity, the effects of the electricity import prices on the heat transfer between areas are analyzed. Changes on area 2's electricity import price do not affect neither the amount of heat transferred nor its price, Figure 3.13. However, the electricity import price for area 1 has an impact on the heat transfer

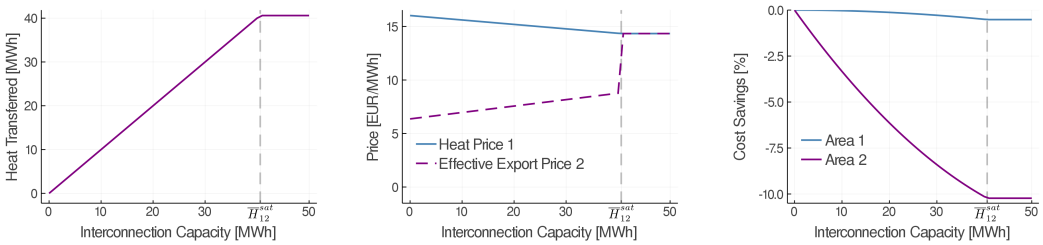

(a) Heat Transfer (b) Marginal Gen Cost and Transfer Cost (c) Heat Expense

Figure 3.12: Sensitivity analysis of the heat transfer capacity's impact on: (a) amount of heat transferred, (b) price differences, and (c) operational cost savings. $\eta_{ba}^{\text{tr}} = 0.9$.

price but not on the transferred heat, which is maintained at a value of 10 €/MWh as in the base case.

Changes on the electricity import price for area 1 affect how much electricity this area will import, thus affecting its internal electricity generation and with it the heating price γ_1 (3.13b), to which the heat transfer price χ_{21} is directly proportional (3.15)[6]. Thus, increments on the electricity import price, π_1^{imp}, lead to an increase on the electricity generation in area 1, increasing the local heating price, γ_1, and with it the heat import price from area 2, χ_{21}. Note that the heat transfer price increases with the electricity import price, up to the point where the area 1 does not import more electricity, i.e., when the generated power matches the local demand. For area 2 the changes on its electricity import price do not affect the heat exchange price, since this area has higher electricity generation costs; leading it to import electricity at a level that fully satisfies entirely its internal demand.

3.5.2 3-area test case

In this numerical test, we explore the effects that the interconnection topology, transfer capacity, and interconnection efficiencies have in the heat transfer quantities and prices for the 3-area coordination. For this purpose, three possible interconnection topologies are considered: i) triangular connection, i.e., all networks are intercon-

[6]We remind the reader about the relationship between the internal electricity generation p_a and the internal heating price γ_a: $\gamma_a = 2C_{2,a}^{\text{h}} h_a + C_{1,a}^{\text{h}} + C_a^{\text{hp}} p_a + \sum_l \mu_{al} K_{al}^{\text{h}}$. Additionally, the relationship between the local heating price γ_a and the heat import transfer price χ_{ba} is given by: $\chi_{ba} = \eta_{ab}^{\text{tr}} \gamma_a$.

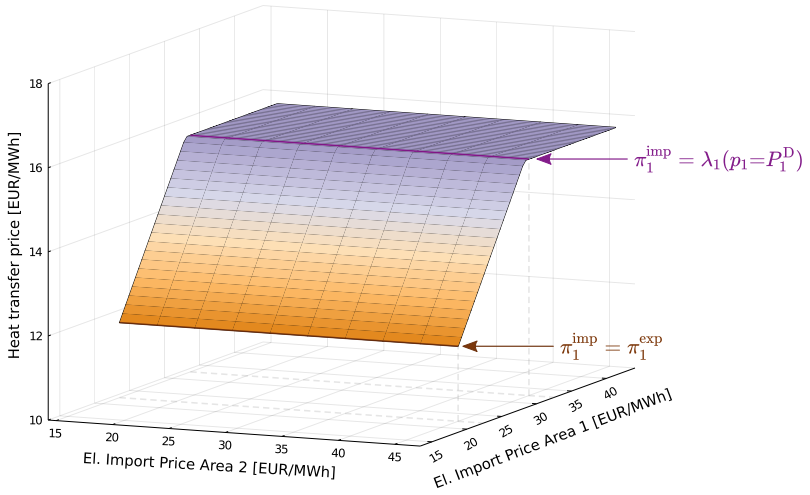

Figure 3.13: Effect of the Electricity Import Prices on the Heat Transfer Price

nected; and ii) 1-3-2 interconnection, i.e., area 1 and 2 have a connection only to area 3; and iii) reduction of transfer efficiency for the triangular interconnection due to larger distance between areas 1 and 3. The results of modifying the topological and interconnection parameters are expected to be maintained for larger and more complex interconnection topologies, since the underlying influence of the technical parameters on the economic operation follows the same principles.

For each topology, 3 sub-cases are created in which all the existent interconnections have the same transfer capacity. The transfer capacity for the sub-cases is set to the values of 20, 40 and 80 MW.

Triangular Coordination

In this configuration, there exists interconnections between all the three areas; labeled here as a triangular configuration. This case will present the optimal heat exchanges and prices when there is the possibility to transfer heat between any pair of areas.

The results of optimal heat exchange for the triangular configuration are presented in Figure 3.14(a). The resultant flow directions are represented by arrows. Based on their cost parameters and local demand area 1 has the highest marginal heat generation costs, and thus it imports heat from the other areas for the three capacity sub-cases. Similarly, area 2 has the lowest marginal costs and exports heat

to areas 1 and 3. Note that the price difference between areas 1–2, as for 1–3, allows for heat transfer towards area 1 in all the sub-cases.

Area 2 and 3 export 20 MWh of heat to area 1, at maximum capacity, while area 2 exports an additional 5.55 MWh to area 3 at a lower price. Area 2 cannot increase the quantity of heat it exports to area 3, since at a transfer of 5.55 MWh the internal price of area 3 matches the effective import price from area 2 to 3, i.e., γ_3=7.90=7.11/0.9=$\gamma_2/\eta_{23}^{\text{tr}}$=$\gamma_{23}^{\text{eff}}$.

Once the capacity is increased to 40 MWh, the transfer from area 2 to area 1 is increased to the maximum allowed quantity and the heat transferred to area 3 is reduced, since it is more profitable to export to area 1. The exported quantity from area 3 to area 1 is reduced, since at a net import of 50 MWh the marginal generation price in area 1 matches the effective import price of 13.72 €/MWh. Thus, area 3 cannot compete with the new price from area 2. If area 3 increased its amount of transferred heat, its price would increase and this new price would not be acceptable for area 1. This case is an example of how the saturation of the transfer capacity between two areas can favor a third one, since are 3 receives higher revenue from a topology with a capacity of 20 MWh than it does for one with 40 MWh.

An additional increase in the transfer capacity to 80 MWh does not increase the total area 1 imports, since the transfer of an extra unit of heat would increase the effective import price and reduce the local area 1 price. Consequently making the price of area 1 lower than the effective import price, which leads to an economically inefficient transfer. Therefore, the total import of area 1 remains the same as that imported for the case with 40 MWh but the imported heat from area 2 is increased by 0.6 MWh, at which point the local price of area 2 matches that of area 3 at 12.35 €/MWh. At a capacity of 80 MW, it is not convenient the transfer between areas 2 and 3, given that they have equal internal prices and the transfer of heat would incur in economic losses due to the inefficiency of the interconnection.

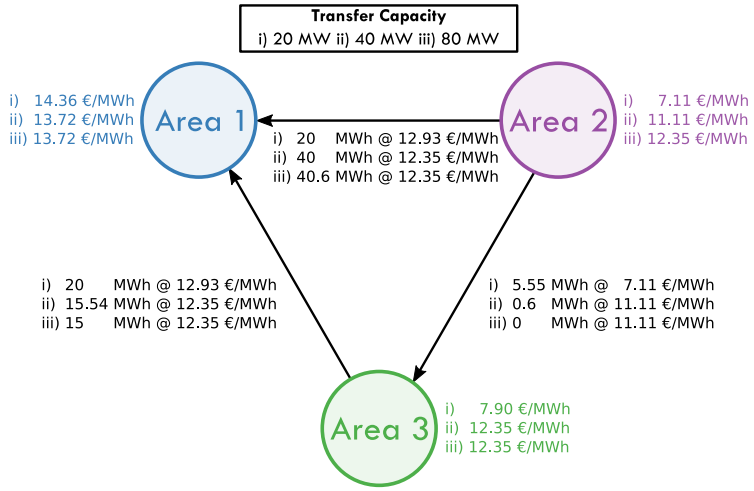

(a) Triangular coordination with $\eta_{ab}^{\text{tr}} = 0.9$.

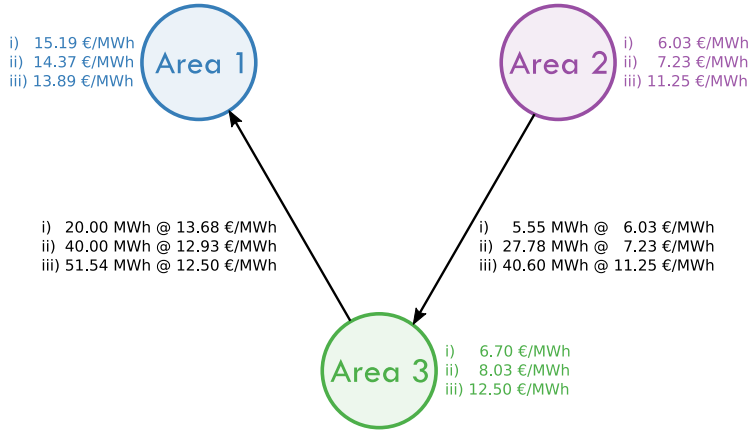

(b) 1-3-2 coordination with $\eta_{ab}^{\text{tr}} = 0.9$.

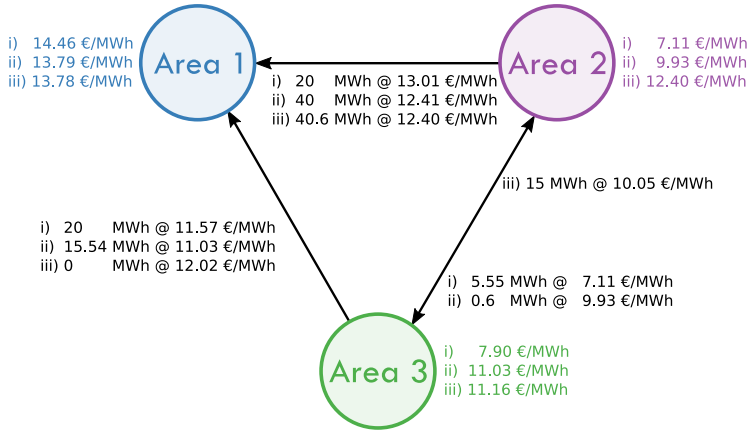

(c) Triangular coordination with $\eta_{12}^{\text{tr}} = \eta_{23}^{\text{tr}} = 0.9$ and $\eta_{13}^{\text{tr}} = 0.8$.

Figure 3.14: Topologies for the 3-area case: (a) triangular, (b) 1-3-2, and (c) triangular with $\eta_{13}^{\text{tr}} = 0.8$. The internal heating prices are given for each sub-case next to the areas in their same color. The transferred heat between areas and its price is given along the edges connecting the areas. The arrows indicate the obtained heat exchange direction.

Topology effect: 1-3-2 coordination

In this topology, area 3 serves as a buffer between areas 1 and 2, Figure 3.14(b). For the sub-cases with a capacity of 20 and 40 MWh, area 3 exports heat to area 1 at the maximum capacity, owing to the fact that it must not compete with area 2. However, as in the triangular topology, the maximum quantity at which area 1 can benefit from importing is 51.54 MWh. Therefore, even though the capacity is increased to 80 MWh, area 3 cannot increase it exports to area 1 beyond this quantity.

At a maximum capacity of 20 MWh, area 3 receives from area 2 the same quantity of heat as in the triangular case. For the case with 40 and 80 MWh, the transfer between area 2 and 3 increases due to the fact that area 3 is exporting more to area 1. Thus, area 3 benefits from arbitraging between the import price from area 2 and export price to area 1. Area 3 can purchase heat from area 2 at a lower price than it charges area 1. This increment reflects the lack of connection between areas 1 and 2, since area 2 must now redirect all of its export to area 3 at a lower price than what it would charge if it had a direct connection to area 1, receiving 11.25 instead of 12.35 €/MWh.

The use of the presented heat market model could be employed to analyze the economic viability of establishing inter-area pipelines and the optimal interconnection topology. As seen on Figure 3.14, for areas 2 and 1 the most profitable configuration is a triangular on2, while for area 3 the 1-2-3 configuration. The investment costs would thus determine the optimal configuration between the three areas.

Efficiency effect

To analyze the impact of the efficiency in import prices from different areas, the triangular case has been modified with η_{12}^{tr}=η_{23}^{tr}=0.9 and η_{13}^{tr}=0.8, Figure 3.14(c). For the capacity sub-cases of 20 and 40 MWh, the transfer quantities are the same as the topology with equal interconnection efficiency. However, unlike the case with equal transfer efficiencies, area 1 pays different import prices to areas 2 and 3.

In the base case with a 90% transfer efficiency, Figure 3.14(a), even though areas 2 and 3 have different internal prices, of respectively 7.11 and 7.90 €/MWh, their

export to area 1 is paid for both at 12.93 €/MWh. This corresponds to the fact that the export price to area 1 is determined by its internal heat price and the interconnection efficiency as seen in expression (3.15). Since the transfer efficiency between areas 1–2 and 1–3 equals 0.9, areas 2 and 3 receive the same price of export to area 1, which corresponds to the value that the heat received by area 1 has; not to the cost incurred by the exporter. When the interconnection efficiency between areas 1 and 3 is reduced, the price paid to area 3 is reduced to compensate for higher losses, Figure 3.14(c).

For a transfer capacity of 80 MWh, area 2 assumes the total share of the export to area 1. The reduction of the export from area 3 represents that the effective import price χ_{31}^{eff} is higher than the local heat price in area 1, corresponding to the lower interconnection efficiency. The exports of area 3 must be then redirected to area 2 which has a higher local price and lower transfer losses. However, the export to area 2 is done at a lower price than that received from area 1 at a higher efficiency of 0.9.

3.6 Conclusions

In this work, we analyzed the main economic principles in heat markets for integrated heat-and-power microgrids, i.e., networks that can generate thermal and electric energy to satisfy their internal demand. We present a convex heat market formulation in both a centralized and decentralized manner. A centralized market approach can be used by an operator when managing a vast number of small heat microgrids in an urban area. Thus, reducing the communication overhead necessary for a decentralized approach. On the other hand, a decentralized market allows preserving each area's independent operation and privacy while guaranteeing fast optimality convergence, modeled in this work done via a Jacobi–Proximal ADMM.

Heat transfer between areas reduces overall energy consumption and expenses for the market participants. The profitability of heat exchange between adjacent areas is influenced by i) price difference between local heat prices, ii) interconnection efficiency, iii) connection topology and iv) transfer capacity. In the presented case

studies, heat transfer at maximum capacity reduced heating-related costs by more than 10%.

Savings derived from the implementation of a heat transfer market are dependent on differences between local area prices, interconnection capacity, and transfer efficiency. The evaluation of interconnection capacities and configurations would allow network owners and investors to assess the economic benefits derived from such a market.

THIS PAGE INTENTIONALLY LEFT BLANK

Chapter 4

Energy and Balancing Pricing in Stochastic Power Markets

Recently, chance-constrained stochastic energy markets have been proposed to address shortcomings of scenario-based stochastic market designs. In particular, the chance-constrained market-clearing avoids trading off in-expectation and per-scenario characteristics and yields unique energy and reserves prices. However, current formulations rely on symmetric control policies based on the aggregated system imbalance, which restricts balancing providers in their energy and reserve commitments. This chapter extends existing chance-constrained market-clearing formulations by leveraging node-to-node and asymmetric balancing policies and deriving the resulting energy and reserve prices. The proposed node-to-node policy allows for relating the remuneration of balancing providers and payment of uncertainty sources using a marginal cost-based approach. Further, we introduce asymmetric balancing into the chance-constrained framework and show how this additional degree of freedom affects the market outcomes.

The contents of this chapter are partially based on a paper submitted to the journal *IEEE Transactions on Power Systems*.

This chapter is organized as follows. Section 4.2 presents the developed formulation for an energy and spinning reserves market based on asymmetric node-to-node balancing. Next, based on duality theory, Section 4.3 derives the energy and balancing prices from the market proposed in Section 4.2. In Section 4.4 we relate

the proposed market scheme with those present in the literature, by modifying the balancing rules and comparing the obtained energy and balancing prices, while Section 4.5 determines the main factors influencing the energy and balancing prices for the different balancing frameworks. Section 4.6 analyzes the incurred costs from renewable forecasting errors and proves how these costs equal the payments made to balancing generators. Thus, providing an approach to pricing compensation costs from renewable generators introducing uncertainty in the system. Finally, Section 4.8 numerically contrasts the generation dispatch under diverse balancing provision. The computational results show a decrease in balancing requirements and costs under the proposed balancing framework.

Nomenclature

The mathematical symbols used in this chapter are described in the table below:

Abbreviations	
CC-OPF	chance-constrained optimal power flow
GPM_i	generator i's profit maximization problem
ISO	Independent system operator
LBP	Locational balancing price
LMP	Locational marginal price
N2N	Node-to-node
OPF	Optimal power flow
OPF-N2N-AB	Optimal power flow with asymmetric node-to-node balancing policy
OPF-N2N-SB	Optimal power flow with symmetric node-to-node balancing policy
OPF-SW-AB	Optimal power flow with asymmetric system-wide balancing policy
OPF-SW-SB	Optimal power flow with symmetric system-wide balancing policy
RES	Renewable energy sources
SW	System-wide

Indexes

i, j	Network nodes
u, v, w	Renewable generation units

Sets

$\mathcal{C}_i$	Nodes with direct connection to i
$\mathcal{G}$	Controllable generators
$\mathcal{U}$	Renewable generators
$\mathcal{U}_i$	Renewable generators located at i

Parameters

$c_{(\cdot),i}$	Generation cost coefficients	[–]
D_i	Nodal power demand	[MW]
e	Vector of ones of appropriate dimensions	[–]
$\overline{F}_{ij}$	Maximum active power line flow	[MW]
M	Vector of expected negative and positive forecast errors (M=$\mathbb{E}[\boldsymbol{\omega}]$) [–]	
$\underline{P}_i/\overline{P}_i$	Generation capacity limits	[MW]
s^2	Sum over the covariance matrix of forecast errors (s^2=$e\Sigma e$)	[MW^2]
$\mathbf{w}_u$	Stochastic renewable power output at u ($\mathbf{w}_u$=$\mathrm{w}_u + \boldsymbol{\omega}_u$)	[MW]
w_u	Forecasted renewable power output at u	[MW]
X_{ij}	Line reactance	[p.u.]
z_i	Auxiliary parameter (z_i=$\sqrt{(1-\epsilon_i)/\epsilon_i}$)	[–]
ϵ_i	Probability of generation capacity constraints violation	[–]
μ_u	Expected value of the forecast error $\boldsymbol{\omega}_u$	[MW]
$\sigma_{u,v}$	Covariance between forecast errors at u and v	[MW^2]
Σ	Covariance matrix of forecast errors (Σ=$cov[\boldsymbol{\omega}]$)	[MW^2]
$\boldsymbol{\omega}$	Vector of nodal forecast errors $\left[\boldsymbol{\omega}_1^-, ..., \boldsymbol{\omega}_{\lvert\mathcal{U}\rvert}^-, \boldsymbol{\omega}_1^+, ..., \boldsymbol{\omega}_{\lvert\mathcal{U}\rvert}^+\right]$	[MW]
$\boldsymbol{\omega}_u$	Stochastic generation forecast error at u ($\boldsymbol{\omega}_u$=$\boldsymbol{\omega}_u^- + \boldsymbol{\omega}_u^+$)	[MW]
$\boldsymbol{\omega}_u^{-/+}$	Negative/positive component of the forecast error $\boldsymbol{\omega}_u$	[MW]

Variables

A_i	Vector of balancing participation factors $\left[\alpha_{i1}^{-}, ..., \alpha_{i\|\mathcal{U}\|}^{-}, \alpha_{i1}^{+}, ..., \alpha_{i\|\mathcal{U}\|}^{+}\right]^\top$ [–]	
C_i	Expected generation cost	[$]
f_{ij}	Active power flow on line (i, j)	[MW]
$\boldsymbol{p}_i$	Uncertain power output by the controllable generator at i	[MW]
p_i	Scheduled power output by the controllable generator at i	[MW]
S_i	Auxiliary variable (S_i=$\sqrt{A_i^\top \Sigma A_i}$)	[MW]
$\alpha_{iu}^{-/+}$	Asymmetric balancing participation factors for the controllable generator at i to balance forecast deviations at u	[–]
β_u	Ratio between nodal and system-wide balancing prices	[–]
$\underline{\delta}_i/\overline{\delta}_i$	Dual multiplier related to generation capacity	[$]
λ_i	Electricity price	[$/MWh]
θ_i	Voltage angle	[rad]
$\chi_u^{-/+}$	Asymmetric nodal balancing price	[$]

Functions

$c_i(\cdot)$	Generator cost function
$cov[\cdot]$	Expected value of a random variable
$\mathbb{E}[\cdot]$	Expected value of a random variable
$\mathbb{P}[\cdot]$	Event probability of occurrence
$f_{\boldsymbol{\omega}_u}(\cdot)$	Probability density function of the forecast error $\boldsymbol{\omega}_u$

4.1 Introduction

The deployment of renewable energy sources (RES) challenges wholesale electricity markets' efficiency, which largely treat RES injections as deterministic and do not internalize their stochasticity rigorously. Although, as Hobbs and Oren discuss in [125], recent market design improvements have targeted (and often succeeded in) improving economic and energy efficiency in the presence of RES stochasticity, they

have been "*primarily incremental in nature*," benefiting from enhanced computational capabilities and supply/demand technologies. As a result of these incremental changes, market-clearing procedures have become increasingly complex and market outcomes "*are not transparent and perhaps have contributed to decreases in trading activity*" [125]. This lack of transparency inhibits meaningful interpretations of energy and reserve allocations and prices, i.e., there is no technically and economically sound intuition on (i) which resources drive the demand for balancing services and how much they should pay for it, and (ii) which resources are most efficient to mitigate this stochasticity and how much they should be paid. This chapter aims to develop a stochastic market design that allows such intuitive interpretations and insights into the energy and reserve price formation under RES stochasticity.

Existing stochastic market designs rely on either scenario-based stochastic programming [67] or chance-constrained [70] dispatch models, which outperform deterministic benchmarks in terms of the total operating cost and the accuracy of reserve allocations, [126]. In [127, 128, 129], a two-stage scenario-based stochastic programming framework is used for the day-ahead market-clearing optimization, which yields scenario-specific locational marginal prices (LMPs). Although these LMPs are useful to understand dispatch and price implications of each scenario, it is impossible to ensure cost recovery simultaneously (i.e., each producer recovers its production cost from market outcomes) and revenue adequacy (i.e., the payment collected by the market from consumers is greater than the payment by the market to producers) in each scenario and in expectation over all scenarios without welfare losses and relying on out-of-market corrections and uplift payments [130].

As an alternative to [127, 128, 129, 130], the work in [131, 132, 133, 134, 135] developed a stochastic market design that internalizes the RES stochasticity by means of its statistical moments (e.g., mean and variance) and chance constraints from [70]. Although stochastic by design, the models in [131, 132, 133, 134, 135] render deterministic reformulations that computationally outperform scenario-based formulations, see [70], and produce uncertainty- and risk-aware LMPs and reserve prices. Although these prices capture all uncertainty realizations assumed, they are scenario-agnostic, which guarantees cost recovery and revenue adequacy for convex

markets [132, 135], as well as minimizes the uplift for non-convex markets [132]. Further, [132] shows the chance-constrained framework makes it possible to ensure the cost recovery for each uncertainty realization and in expectation without welfare losses. The qualitative analyses in [132, 133, 134] show that these LMPs do not explicitly depend on statistical moments and risk preferences of the market, while reserve prices explicitly depend on these parameters. Despite these computational and market design advantages relative to [127, 128, 129, 130], the chance-constrained framework has several limitations. First, it typically assumes that the RES stochasticity is symmetric, which does not hold in practice, [72, 73], where upward and downward reserve needs vary significantly. Second, while allowing for a nodal reserve allocation, it lacks a nodal reserve pricing mechanism, thus preventing from fairly charging and remunerating those resources that drive the need for and provide balancing services, respectively.

This chapter extends the market design originally proposed in [132, 133, 134] to accommodate asymmetric reserve provision, node-to-node reserve pricing, and provide techno-economic insights on the energy and reserve price formation process under uncertainty. Considering the asymmetric reserve provision leads to appropriately sizing and allocating reserve requirements based on empirical RES statistics (e.g., moments), while the node-to-node reserve pricing mechanism leads to the transparent allocation of (i) uncertainty costs among RES resources and (ii) reserve payments among producers, thus incentivizing the efficient energy and reserve co-optimization to firm up RES generation as necessitated in [125].

4.2 Asymmetric Chance-Constrained OPF

Consider an electricity market operator that uses an optimal power flow (OPF) formulation to compute a least-cost generator schedule. As shown in [131, 132, 133, 134, 135], traditional deterministic OPF-based market designs (see, e.g., [136] for reference) can be efficiently robustified against uncertain injections from RES by means of chance-constraints. For this purpose, injections at every network node u that hosts an uncertain RES resource is modeled as random variable $\mathbf{w}_u$ using a

forecast value w_u and a forecast error term $\boldsymbol{\omega}_u$ as follows:

$$\mathbf{w}_u = \mathrm{w}_u + \boldsymbol{\omega}_u. \tag{4.1}$$

Typically, $\boldsymbol{\omega}_u$ is assumed to be zero-mean and normally distributed, [69, 70, 126, 131, 133, 134, 135]. However, in practice, empirical measurements of solar and wind power forecast errors are often asymmetric and can not be captured well by a Gaussian normal distribution, [72, 73]. As a result, the impact of forecast errors from nodes with significant asymmetries might be over- or under-estimated. For example, by inspecting day-ahead forecast and actual generation data recorded at two nodes in the ENTSO-E (European Network of Transmission System Operators for Electricity) in 2020, plotted in Figure 4.1, the diversity of forecast error distributions becomes evident. While the forecast at the German node, Figure 4.1(a), is symmetric and may be parametrized as a normal distribution, the forecast at the Italian node, Figure 4.1(b), is strongly skewed to overestimate generator output and a normal distribution is unsuitable to model the forecast error distribution. Additionally, there exists a tendency of RES operators to report generation values lower than the day-ahead forecast; which could be a result of strategic forecast offering by the generator in order to obtain additional benefits from the market regulations. See also discussion in [137, Section 6.6.].

As a result, assuming normally distributed (symmetric) forecast errors in combination with a symmetric balancing regulation policy as in [69, 70, 126, 131, 133, 134, 138, 139, 140, 141, 142, 143] can lead to ineffective and inefficient operating decisions and electricity prices. Therefore, to adequately capture possible forecast error asymmetries and improve the efficiency of balancing reserve quantification and allocation, this chapter explicitly models negative and positive forecast errors (i.e., real-time energy deficit and surplus, respectively) and proposes a suitable asymmetric balancing regulation policy. Sections 4.2.1 and 4.2.2 below describe the asymmetric model of uncertain injections and introduce an asymmetric balancing reserve policy, respectively. Section 4.2.3 derives the resulting chance-constrained optimal power flow problem.

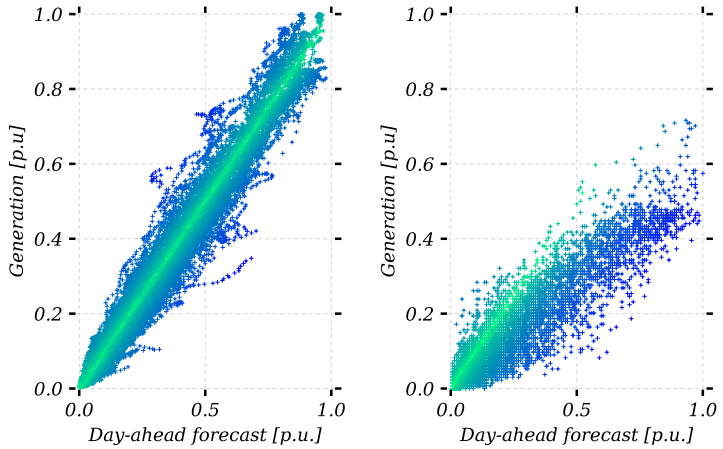

(a) Germany, `10YDE-EON---1` (b) Italy, `10Y1001A1001A70O`

Figure 4.1: Day-ahead forecast w_t and actual generation p_t per unit of maximal power generation in a European aggregation area. An accurate forecast falls on the line $p_t = w_t$. Figure 4.1(b) illustrates that forecasting errors in practice can be non-zero-mean.

4.2.1 Asymmetric Uncertainty Model

Consider random variable $\boldsymbol{\omega}_u$ as

$$\boldsymbol{\omega}_u = \boldsymbol{\omega}_u^- + \boldsymbol{\omega}_u^+, \tag{4.2}$$

where $\boldsymbol{\omega}_u^- \leq 0$ and $\boldsymbol{\omega}_u^+ \geq 0$ are the negative and positive components of the forecast error such that $\boldsymbol{\omega}_u^- \boldsymbol{\omega}_u^+ = 0$, i.e., $\boldsymbol{\omega}_u^-$ and $\boldsymbol{\omega}_u^+$ are mutually exclusive events. First, we assume that any expected systematic forecast error can be considered as a fixed parameter in the model (e.g. by accounting it to fixed load forecasts), so that the total imbalance $\boldsymbol{\omega}_u$ can always be corrected to have zero-mean. See e.g. [133]. Second, from (4.2) and the linearity of the expectation, it follows that $\mathbb{E}[\boldsymbol{\omega}_u] = \mathbb{E}[\boldsymbol{\omega}_u^- + \boldsymbol{\omega}_u^+] = 0$, i.e., $\mathbb{E}[\boldsymbol{\omega}_u^+] = -\mathbb{E}[\boldsymbol{\omega}_u^-] = \mu_u$. Therefore, for a zero-mean forecast the expected deviation on both directions, positive and negative, are equal independently of the forecast distribution. Figure 4.2(a)–(b) illustrate this representation, which allows for modeling asymmetric distributions.

Mean μ_u of the forecast distributions can be obtained by considering them as distributions truncated at zero. For instance, for an estimated continuous distribution,

it follows:

$$\mu_u = \mathbb{E}[\boldsymbol{\omega}_u \geq 0] = \mathbb{E}\left[\boldsymbol{\omega}_u^+\right] = \int_0^\infty \omega_u f_{\boldsymbol{\omega}_u}(\omega_u)\, d\omega_u, \quad \forall u \tag{4.3}$$

where $f_{\boldsymbol{\omega}_u}$ is the probability density function of the forecast error $\boldsymbol{\omega}_u$.

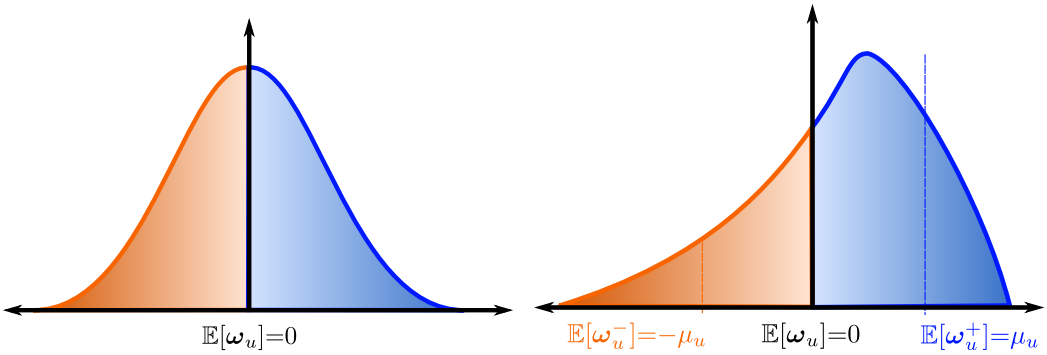

(a) Symmetric forecast error (b) Asymmetric forecast error

Figure 4.2: Nodal forecast errors $\boldsymbol{\omega}_u$ for (a) symmetric or (b) asymmetric probability distributions with zero expected value.

4.2.2 Asymmetric Node-to-Node Balancing

To ensure that the power system remains balanced (i.e., generation equals demand at all times), generators with balancing control capabilities react to any real-time imbalances $\boldsymbol{\omega}_u^-$, $\boldsymbol{\omega}_u^+$ by increasing or decreasing their power outputs. We model this balancing control policy using asymmetric "node-to-node" balancing participation factors $\alpha_{iu}^-, \alpha_{iu}^+ \in [0,1]$ that capture the participation of a generator at bus i to balancing the negative and positive imbalance caused by a stochastic resource at bus u. Note that for ease of notation, we assume that each node i hosts exactly one controllable generator and each node u hosts exactly one uncertain RES. The resulting uncertain power output $\boldsymbol{p}_i$ of each controllable generator is then given by:

$$\boldsymbol{p}_i = p_i - \sum_u \left(\alpha_{iu}^- \boldsymbol{\omega}_u^- + \alpha_{iu}^+ \boldsymbol{\omega}_u^+\right), \qquad \forall i \tag{4.4a}$$

$$\sum_i \alpha_{iu}^- = 1, \quad \sum_i \alpha_{iu}^+ = 1, \qquad \forall u \tag{4.4b}$$

where p_i and $\alpha_{iu}^{-}, \alpha_{iu}^{+} \in [0,1]$ are decision variables that define the power output and asymmetric participation factors for balancing reserve provision. Constraints Eq. (4.4b) ensure system balance for all outcomes $\boldsymbol{\omega}_u^{-}$, $\boldsymbol{\omega}_u^{+}$ [140, 143]. Note that uncertain variables are written in **bold** font throughout this chapter.

4.2.3 Model Formulation

Following [69, 131, 133, 134, 135], the model objective is to minimize the expected production cost of conventional generators. By replacing $\boldsymbol{p}_i$ from (4.4a) in (4.5), the expected generation cost C_i of generator i can be calculated as in Eq. (4.6) (see Appendix C for details):

$$c_i(\boldsymbol{p}_i) = c_{2,i}(\boldsymbol{p}_i)^2 + c_{1,i}(\boldsymbol{p}_i) + c_{0,i}, \quad \forall i \tag{4.5}$$

$$\begin{aligned}\mathbb{E}[c_i(\boldsymbol{p}_i)] &=: C_i \\ &= c_{2,i}p_i^2 + c_{1,i}p_i + c_{0,i} - (2c_{2,i}p_i + c_{1,i})(MA_i) + c_{2,i}\left[(M \cdot A_i)^2 + S_i^2\right], \quad \forall i,\end{aligned} \tag{4.6}$$

where M is the row vector of expected negative and positive forecast errors, $M = \mathbb{E}[\boldsymbol{\omega}]$, with $\boldsymbol{\omega} = \left[\boldsymbol{\omega}_1^{-}, \boldsymbol{\omega}_2^{-}, ..., \boldsymbol{\omega}_{|\mathcal{U}|}^{-}, \boldsymbol{\omega}_1^{+}, \boldsymbol{\omega}_2^{+}, ..., \boldsymbol{\omega}_{|\mathcal{U}|}^{+}\right]$, and A_i is the vector of balancing participation factors for generator i, $A_i = \left[\alpha_{i1}^{-}, \alpha_{i2}^{-}, ..., \alpha_{i|\mathcal{U}|}^{-}, \alpha_{i1}^{+}, \alpha_{i2}^{+}, ..., \alpha_{i|\mathcal{U}|}^{+}\right]^{\top}$. The $\cdot$ operator denotes the dot-product of two vectors. The covariance matrix of the forecast errors is given by $\Sigma = cov[\boldsymbol{\Omega}]$ and $S_i = \sqrt{A_i^{\top}\Sigma A_i} = \left\| A_i \Sigma^{1/2} \right\|_2$. Upper and lower power output limits are enforced by the chance constraints (4.7a) and (4.7b), respectively, and parameter ϵ_i is chosen to ensure constraint satisfaction with an $1-\epsilon_i$ guarantee:

$$\mathbb{P}\left[\boldsymbol{p}_i \leq \overline{P}_i\right] \geq 1 - \epsilon_i, \quad \forall i \tag{4.7a}$$

$$\mathbb{P}[-\boldsymbol{p}_i \leq -\underline{P}_i] \geq 1 - \epsilon_i, \quad \forall i. \tag{4.7b}$$

Constraints (4.7a) and (4.7b) must reflect the probability that the aggregated fulfillment of the node-to-node balancing commitment does not exceed the capacity limits. Therefore, the underlying probability distribution functions representing the different RES must be reflected in the generation capacity limits. However, unlike

for Gaussian distributions, the aggregation of asymmetric distributions truncated at do not have an equivalent deterministic representation. To overcome this issue, we apply the Chebyshev inequality to (4.7) for representing its satisfaction probability for any kind of underlying distribution [69]. Thus, the capacity constraints (4.7) can be reformulated by means of the Chebyshev approximation, as the deterministically-equivalent constraints (4.8a) and (4.8b):

$$p_i - M{\cdot}A_i + z_i S_i \leq \overline{P}_i, \qquad \forall i \tag{4.8a}$$

$$-p_i + M{\cdot}A_i + z_i S_i \leq -\underline{P}_i, \qquad \forall i, \tag{4.8b}$$

where the parameter $z_i{=}\sqrt{(1-\epsilon_i)/\epsilon_i}$.

Using (4.4b), (4.6), (4.8a), and (4.8b), Model 7 formulates an OPF problem with a deterministic equivalent of the chance-constrained generator dispatch for node-to-node asymmetric balancing policy (OPF-N2N-AB). The objective function in (4.9a) minimizes the expected system generation cost and is subject to DC power flow network constraints (4.9b)-(4.9e), asymmetric node-to-node balancing adequacy requirements (4.9f)–(4.9g), and chance-constrained generator output limits (4.9h)–(4.9i). In the OPF-N2N-AB, the network buses are indexed by i, the RES buses by $u \in \mathcal{U}_i$, and the power lines by the tuple (i,j) with $j \in \mathcal{C}_i$. The nodal demand is given by D_i and the lines' reactance by X_{ij}. The line flow is represented by f_{ij} and the nodal voltage angle by θ_i. Line capacity limits are set at $\overline{F}_{ij}$, while the minimum and maximum generation capacity limits are respectively defined as $\underline{P}_i$ and $\overline{P}_i$.

The decision variables of OPF-N2N-AB are collected in set $\Xi = \{p_i, \alpha^{-}_{iu}, \alpha^{+}_{iu}, f_{ij}\}$. Greek symbols in parenthesis define dual multipliers associated with each constraint. Note that OPF-N2N-AB is a non-linear program (NLP) with second-order conic constraints. Specifically, objective (4.9a) contains bi-linear terms that require suitable solution techniques presented in Section 4.7. However, the second-order conic solution space spanned by constraints (4.9b)–(4.9i) is convex and thus enables the analytical derivations in the following sections.

Model 7 OPF-N2N-AB

$$\min_{\Xi} \sum_i \Big[c_{2,i} {p_i}^2 + c_{1,i}(p_i) + c_{0,i} - (2c_{2,i}p_i + c_{1,i})(M \cdot A_i) + c_{2,i}\big[(M \cdot A_i)^2 + S_i^2\big] \Big] \tag{4.9a}$$

subject to:

$$(\lambda_i): \quad p_i + \textstyle\sum_{u \in \mathcal{U}_i} \mathrm{w}_u - D_i - \sum_{j \in \mathcal{C}_i} f_{ij} = 0, \qquad \forall i \tag{4.9b}$$

$$(\psi_{ij}): \quad f_{ij} - \frac{1}{X_{ij}}(\theta_i - \theta_j) = 0, \qquad \forall i, j \in \mathcal{C}_i \tag{4.9c}$$

$$(\overline{\eta}_{ij}): \quad f_{ij} \leq \overline{F}_{ij}, \qquad \forall i, j \in \mathcal{C}_i \tag{4.9d}$$

$$(\underline{\eta}_{ij}): \quad -f_{ij} \leq -\overline{F}_{ij}, \qquad \forall i, j \in \mathcal{C}_i \tag{4.9e}$$

$$(\chi_u^-): \quad \sum_i \alpha_{iu}^- = 1, \qquad \forall u \tag{4.9f}$$

$$(\chi_u^+): \quad \sum_i \alpha_{iu}^+ = 1, \qquad \forall u \tag{4.9g}$$

$$(\overline{\delta}_i): \quad p_i - M \cdot A_i + z_i S_i \leq \overline{P}_i, \qquad \forall i \tag{4.9h}$$

$$(\underline{\delta}_i): \quad -p_i + M \cdot A_i + z_i S_i \leq -\underline{P}_i, \qquad \forall i. \tag{4.9i}$$

4.3 Pricing Energy and Balancing Provision

From the perspective of an electricity market operator, e.g., as in current U.S. practice an Independent System Operator (ISO), OPF-N2N-AB resembles a market clearing problem that is used to compute optimal (least-cost) generator dispatch and balancing reserve decisions p_i^*, $\alpha_{iu}^{-,*}$, $\alpha_{iu}^{+,*}$ and efficient corresponding prices for energy π^{p} and reserves π_u^-, π_u^+. The price-quantity tuples $(\pi^{\mathrm{p}}, p_i^*)$, (π_u^-, α^-), $(\pi_u^+, \alpha_{iu}^{+,*})$ are efficient if they support a competitive equilibrium, i.e., they ensure that [69]:

1. The market clears at $p_i^* + \sum_{u \in \mathcal{U}} \mathrm{w}_u - \sum_{j \in \mathcal{C}_i} f_{ij} = D_i, \ \forall i, \ \sum_i \alpha_{iu}^{-,*} = \sum_i \alpha_{iu}^{+,*} = 1, \ \forall u$.

2. Prices π^{p}, π_u^- and quantities p_i^*, $\alpha_{iu}^{-,*}$ maximize the profit of i given by $\Pi_i = \pi_i^{\mathrm{p}} p_i^* + \sum_u \big(\pi_u^- \alpha_{iu}^{-,*} + \pi_u^+ \alpha_{iu}^{+,*}\big) - C_i$, i.e., there is no incentive to deviate these market outcomes.

To derive these prices from OPF-N2N-AB, we use duality theory similar to previous works on chance-constrained stochastic market design [69, 133, 134]. However,

unlike in [69, 133, 134], the prices derived from the OPF-N2N-AB model will support asymmetric balancing needs and account for node-to-node participation factors, thus enabling a more precise allocation of balancing resources. First, we prove:

Proposition 1. Consider the OPF-N2N-AB. Let λ_i, χ_u^- χ_u^+ be the locational marginal prices (LMPs) for energy and asymmetric locational balancing prices (A-LBPs) defined as dual multipliers of constraints (4.9b), (4.9f), and (4.9g), respectively. Then, these prices can be expressed as:

$$\lambda_i = 2c_{2,i}(p_i - M\cdot A_i) + c_{1,i} + \overline{\delta}_i - \underline{\delta}_i, \qquad \forall i \tag{4.10a}$$

$$\chi_u^- = \frac{1}{|\mathcal{G}|}\sum_i \left[\mu_u\lambda_i + \left(\Sigma_u^- A_i\right)\left(2c_{2,i} + \frac{z_i}{S_i}\left(\overline{\delta}_i + \underline{\delta}_i\right)\right)\right], \qquad \forall u \tag{4.10b}$$

$$\chi_u^+ = \frac{1}{|\mathcal{G}|}\sum_i \left[-\mu_u\lambda_i + \left(\Sigma_u^+ A_i\right)\left(2c_{2,i} + \frac{z_i}{S_i}\left(\overline{\delta}_i + \underline{\delta}_i\right)\right)\right], \qquad \forall u. \tag{4.10c}$$

where Σ_u^- and Σ_u^+ are the rows of the covariance matrix Σ related to the asymmetric forecast errors $\boldsymbol{\omega}_u^-$ and $\boldsymbol{\omega}_u^+$, respectively.[1]

Proof. Consider the first-order optimality conditions of (4.9) for variables p_i, α_{iu}^-, and α_{iu}^+:

$$2c_{2,i}(p_i - M\cdot A_i) + \overline{\delta}_i - \underline{\delta}_i - \lambda_i = 0, \qquad \forall i \tag{4.11a}$$

$$\left(\Sigma_u^- A_i\right)\left(2c_{2,i} + \frac{z_i}{S_i}\left(\overline{\delta}_i + \underline{\delta}_i\right)\right) + \mu_u\left(2c_{2,i}(p_i - M\cdot A_i) + \overline{\delta}_i - \underline{\delta}_i\right) - \chi_u^- = 0, \qquad \forall i,u \tag{4.11b}$$

$$\left(\Sigma_u^- A_i\right)\left(2c_{2,i} + \frac{z_i}{S_i}\left(\overline{\delta}_i + \underline{\delta}_i\right)\right) - \mu_u\left(2c_{2,i}(p_i - M\cdot A_i) + \overline{\delta}_i - \underline{\delta}_i\right) - \chi_u^+ = 0, \qquad \forall i,u. \tag{4.11c}$$

Expression (4.10a) immediately follows from separating λ_i from (4.11a). Note that χ_u^- and χ_u^+ are the dual variables of the nodal balancing reserve adequacy constraints in Eq. (4.9f) and (4.9g) and, therefore, are specific to node u requiring balancing services, as opposed to generator i providing balancing services. Therefore, expressions (4.11b) and (4.11c) have the same value for each generator i and can be summed over all $|\mathcal{G}|$ generators, leading to $\sum_{i\in\mathcal{G}}\chi_u^- = |\mathcal{G}|\chi_u^-$ and $\sum_{i\in\mathcal{G}}\chi_u^+ = |\mathcal{G}|\chi_u^+$. Hence, we obtain (4.10b) and (4.10c) by dividing (4.11b) and (4.11b) by $|\mathcal{G}|$. ■

[1] For example, in a system with two RES $\Sigma_1^- = \left[Var(\boldsymbol{\omega}_1^-), cov(\boldsymbol{\omega}_1^-, \boldsymbol{\omega}_1^+), cov(\boldsymbol{\omega}_1^-, \boldsymbol{\omega}_2^-), cov(\boldsymbol{\omega}_1^-, \boldsymbol{\omega}_2^+)\right]$.

Model 8 GPM$_i$-N2N-AB

$$\text{max.} \quad \Pi_i = \pi_i^{\text{p}} p_i + \sum_u \left(\pi_u^{\text{-}} \alpha_{iu}^{\text{-}} + \pi_u^{+} \alpha_{iu}^{+}\right) - C_i \tag{4.12a}$$

subject to:

$$(\overline{\delta}_i): \quad p_i - M \cdot A_i + z_i S_i \leq \overline{P}_i, \qquad \forall i \tag{4.12b}$$

$$(\underline{\delta}_i): \quad -p_i + M \cdot A_i + z_i S_i \leq -\underline{P}_i, \qquad \forall i. \tag{4.12c}$$

We now prove that the dual variables used as prices in Proposition 1 together with the primal dispatch decisions satisfy the conditions for a competitive equilibrium.

***Theorem* 1.** Consider the OPF-N2N-AB, using $\pi^{\text{p}} = \lambda_i^*$, $\pi_u^{\text{-}} = \chi_u^{-,*}$ and $\pi_u^{+} = \chi_u^{+,*}$ as the LMPs and A–LBPs constitutes a competitive equilibrium.

***Proof*.** Each generator i's profit maximization problem (GPM$_i$) is modeled as given in Model 8, which is abbreviated below as GPM$_i$-N2N-AB. The first-order optimality conditions of this optimization with respect to decision variables p_i, $\alpha_{iu}^{\text{-}}$, and α_{iu}^{+} lead to the expressions (4.13a),(4.13b), and (4.13c), respectively:

$$\pi_i = 2c_{2,i}(p_i - M \cdot A_i) + c_{1,i} + \overline{\delta}_i - \underline{\delta}_i, \qquad \forall i \tag{4.13a}$$

$$\pi_u^{\text{-}} = \mu_u \left(2c_{2,i}(p_i - M \cdot A_i) + c_{1,i} + \overline{\delta}_i - \underline{\delta}_i\right) + \left(\Sigma_u^{-} A_i\right)\left(2c_{2,i} + \frac{z_i}{S_i}\left(\overline{\delta}_i + \underline{\delta}_i\right)\right), \qquad \forall i,u \tag{4.13b}$$

$$\pi_u^{+} = -\mu_u \left(2c_{2,i}(p_i - M \cdot A_i) + c_{1,i} + \overline{\delta}_i - \underline{\delta}_i\right), + \left(\Sigma_u^{+} A_i\right)\left(2c_{2,i} + \frac{z_i}{S_i}\left(\overline{\delta}_i + \underline{\delta}_i\right)\right), \quad \forall i,u. \tag{4.13c}$$

Due to the equality of first-order optimality conditions in (4.13a)–(4.13c) and in (4.10a)–(4.10c), it follows that the primal $(p_i, \alpha_{iu}^{+}, \alpha_{iu}^{\text{-}})$ and dual $(\lambda_i, \chi_u^{\text{-}}, \chi_u^{+})$ solution from the centralized OPF-N2N-AB model, which satisfies constraints (4.9b), (4.9g) and (4.9f), also solves the GPM$_i$-N2N-AB model for each generator. Hence, the prices obtained in Proposition 1 and derived from the OPF-N2N-AB, (4.10a)–(4.10c), constitute a competitive equilibrium, i.e. $\pi^{\text{p}} = \lambda_i^*$, $\pi_u^{\text{-}} = \chi_u^{-,*}$ and $\pi_u^{+} = \chi_u^{+,*}$. ■

4.4 Symmetric and System-wide Markets

Using the results derived in Section 4.3, we consider several particular cases that allow for relating the obtained prices to existing results in [69, 70, 126, 131, 133, 134, 140, 143]. A summary of the relationship between the pricing for the different balancing schemes is provided in Table 4.1.

4.4.1 Asymmetric System-wide Balancing – OPF-SW-AB

Instead of the node-to-node balancing regulation policy (4.4a), the proposed OPF-N2N-AB can be modified to use a balancing policy based on the aggregated system-wide uncertainty as in, e.g., [69, 131, 133, 134]. Here, the system-wide uncertainty is given as:

$$\boldsymbol{\Omega}^{\text{-}}=\sum_{u}\boldsymbol{\omega}_{u}^{\text{-}},\quad \boldsymbol{\Omega}^{+}=\sum_{u}\boldsymbol{\omega}_{u}^{+}, \tag{4.14}$$

where in turn $\boldsymbol{\Omega}^{+}$ and $\boldsymbol{\Omega}^{\text{-}}$ are linked by:

$$\mathbb{E}\left[\boldsymbol{\Omega}^{+}+\boldsymbol{\Omega}^{\text{-}}\right]=\mathbb{E}[\boldsymbol{\Omega}]=0, \tag{4.15}$$

and the the node-to-node participation factors used in the OPF-N2N-AB are set to system-wide participation factors by enforcing $\alpha_{iu}^{\text{-}}=\alpha_{i}^{\text{-}}$ and $\alpha_{iu}^{+}=\alpha_{i}^{+}$. As a result we have that $A_i=\left[\alpha_i^{\text{-}},\alpha_i^{+}\right]^{\top}$. Although this approach resembles the pricing mechanism from [69, 131, 133, 134], there is a notable distinction of this representation, because it still accounts for asymmetric distributions and asymmetric provision of balancing services.

We define $\boldsymbol{\Omega}^{\text{-}/+}=\left[\boldsymbol{\Omega}^{\text{-}},\boldsymbol{\Omega}^{+}\right]$ and expected value of $\boldsymbol{\Omega}^{\text{-}/+}$ is then given by $M=\mathbb{E}\left[\boldsymbol{\Omega}^{\text{-}/+}\right]=[-\nu,\nu]$, where $\nu=\sum_u\mu_u=\sum_u\mathbb{E}[\boldsymbol{\omega}_u^{+}]=-\sum_u\mathbb{E}[\boldsymbol{\omega}_u^{\text{-}}]$ is the expected value of the aggregated asymmetric forecast errors. Finally, the covariance matrix of $\boldsymbol{\Omega}^{\text{-}/+}$ is defined as $\Sigma=cov\left(\boldsymbol{\Omega}^{\text{-}/+}\right)$.

1) Generation Output: Under the asymmetric balancing provision with system-wide participation factors, we reformulate Eqs. (4.4a) and (4.4b) as follows:

$$\boldsymbol{p}_i = p_i - \alpha_i^{\text{-}}\boldsymbol{\Omega}^{\text{-}} - \alpha_i^{+}\boldsymbol{\Omega}^{+}, \quad \forall i \tag{4.16a}$$

$$(\chi^{\text{-}}, \chi^{+}): \quad 1 = \sum_i \alpha_i^{\text{-}} = \sum_i \alpha_i^{+}. \tag{4.16b}$$

2) Energy and Balancing Prices:

Following the procedure described in Proposition 1, we derive the following prices:

$$\lambda_i = c_{2,i}(p_i - M{\cdot}A_i) + c_{1,i} + \overline{\delta}_i - \underline{\delta}_i, \qquad \forall i \tag{4.16c}$$

$$\chi^{\text{-}} = \frac{1}{|\mathcal{G}|}\sum_i \left[\nu\lambda_i + (\Sigma^{\text{-}}A_i)\left(2c_{2,i} + \frac{z_i}{S_i}(\overline{\delta}_i + \underline{\delta}_i)\right)\right], \tag{4.16d}$$

$$\chi^{+} = \frac{1}{|\mathcal{G}|}\sum_i \left[-\nu\lambda_i + (\Sigma^{+}A_i)\left(2c_{2,i} + \frac{z_i}{S_i}(\overline{\delta}_i + \underline{\delta}_i)\right)\right], \tag{4.16e}$$

where Σ^{-} and Σ^{+} are the rows of the covariance matrix Σ related to the asymmetric forecast errors $\boldsymbol{\Omega}^{\text{-}}$ and $\boldsymbol{\Omega}^{+}$, respectively. Additionally, $S_i = \sqrt{A_i^{\top}\Sigma A_i} = \left\|A_i\Sigma^{1/2}\right\|_2$. Note that the value of S_i in the OPF-SW-AB and in the derived balancing policies presented below does not equal that of the OPF-N2N-AB. Even though the expression for its calculation is the same, the way in which the vector A_i and the matrix Σ are formed depends on the balancing policy. Notably, the A–LBPs become dependent on the aggregated asymmetric uncertainty in the system and as such are equal for all the RES nodes, i.e., the generators are paid to balance the net system imbalances independently of the source. Hence, relative to OPF-N2N-AB, a system-wide balancing approach does not capture a one-to-one relationship between individual sources of uncertainty and reserve providers, which may lead to inefficient price signaling.

4.4.2 Symmetric Node-to-Node Balancing – OPF-N2N-SB

Another modification of OPF-N2N-AB is derived under the assumption that controllable generators provide balancing regulation using nodal but symmetric participation factors, α_{iu} for a symmetric forecast error $\boldsymbol{\omega}_u = \boldsymbol{\omega}_u^{\text{-}} + \boldsymbol{\omega}_u^{+}$. See, e.g., [140, 143]. Under these assumptions, we obtain $\alpha_{iu} = \alpha_{iu}^{\text{-}} = \alpha_{iu}^{+}$ and $A_i = \left[\alpha_{i1}, \alpha_{i2}, ..., \alpha_{i|\mathcal{U}|}\right]^{\top}$. $\boldsymbol{\omega}$ is the vector of nodal forecast errors and Σ is the covariance matrix of the nodal

forecast errors.

1) Generation Output: Using these assumptions, (4.4a), (4.4b), (4.6) can be reformulated as follows:

$$\boldsymbol{p}_i = p_i - \textstyle\sum_u (\alpha_{iu} \boldsymbol{\omega}_u), \qquad \forall i \tag{4.17a}$$

$$C_i = c_i(p_i) + c_{2,i} S_i, \qquad \forall i, \tag{4.17b}$$

$$(\chi_u): \quad 1 = \sum_u \alpha_{iu}, \qquad \forall u. \tag{4.17c}$$

Expression (4.17b) no longer includes the expected balancing costs, which is cancelled out by symmetric forecast errors.

2) Probabilistic Capacity Limits: Similarly to the expected cost in (4.17b), the capacity limits do not consider the asymmetric nodal RES forecast errors, which makes it possible to recast them as second-order conic constraints dependent on the variances of the nodal forecast errors only:

$$(\overline{\delta}_i): \quad p_i + z_i S_i \leq \overline{P}_i, \qquad \forall i \tag{4.17d}$$

$$(\underline{\delta}_i): \quad -p_i + z_i S_i \leq -\underline{P}_i, \qquad \forall i \tag{4.17e}$$

3) Energy and Balancing Prices: Following the procedure described in Proposition 2, we derive the following prices:

$$\lambda_i = 2c_{2,i} p_i + c_{1,i} + \overline{\delta}_i - \underline{\delta}_i, \qquad \forall i \tag{4.17f}$$

$$\chi_u = \frac{1}{|\mathcal{G}|} \sum_i \left((\Sigma_u A_i) \left(2c_{2,i} + \frac{z_i}{S_i} \left(\overline{\delta}_i + \underline{\delta}_i \right) \right) \right), \quad \forall u, \tag{4.17g}$$

where Σ_u is the row of the covariance matrix Σ related to the nodal forecast error $\boldsymbol{\omega}_u$. The LMPs do not change with the forecasted RES generation and the balancing reserve has only one price χ_u, which is insensitive to the direction of the RES forecast errors and the LMPs. Note that the results in (4.17f) and (4.17g) are similar those from [69, 133, 134].

4.4.3 System-wide Symmetric Balancing – OPF-SW-SB

The most studied chance-constrained electricity market design has system-wide, symmetric RES forecast errors and symmetric generation response firstly introduced in [131] and then applied in [69, 133, 134]. This case can be modeled within the proposed OPF-N2N-AB if $\boldsymbol{\Omega}$ is the system-wide RES forecast error, such that $\boldsymbol{\Omega}=\sum_u \boldsymbol{\omega}_u$, $A_i^-=A_i^+=[\alpha_i, \forall u]$ and $S_i=S_i=\alpha_i s$, where s^2 is the total sum over the covariance matrix, $s^2 = e\Sigma e^T$.

1) Generation Output: Using these assumptions, (4.4a), (4.4b), (4.5), (4.6) can be reformulated as follows:

$$C_i = c_i(p_i) + c_{2,i}\alpha_i^2 s^2, \qquad \forall i \tag{4.18a}$$

$$\boldsymbol{p}_i = p_i - \alpha_i \boldsymbol{\Omega}, \qquad \forall i \tag{4.18b}$$

$$(\chi): \qquad 1 = \sum_i \alpha_i. \tag{4.18c}$$

2) Probabilistic Capacity Limits: Similarly to (4.17d)-(4.17e), the capacity limits are reduced to the linear constraints:

$$\big(\overline{\delta}_i\big): \qquad p_i + z_i\alpha_i s \leq \overline{P}_i, \qquad \forall i \tag{4.18d}$$

$$(\underline{\delta}_i): \qquad -p_i + z_i\alpha_i s \leq -\underline{P}_i, \qquad \forall i. \tag{4.18e}$$

3) Energy and Balancing Prices: Following the procedure described in Proposition 2, we derive the following prices:

$$\lambda_i = 2c_{2,i}p_i + c_{1,i} + \overline{\delta}_i - \underline{\delta}_i, \qquad \forall i \tag{4.18f}$$

$$\chi = \frac{1}{|\mathcal{G}|}\sum_i \big(2c_{2,i}s^2\alpha_i + z_i s\big(\overline{\delta}_i + \underline{\delta}_i\big)\big). \tag{4.18g}$$

Table 4.1: Variables for CC-OPF with balancing regulation

Balancing Type		Participation Factor		Energy Price	Balancing Price	
		α_{iu}^-	α_{iu}^+	λ_i	χ_u^-	χ_u^+
Asymmetric	Node-to-Node (OPF-N2N-AB)	α_{iu}^-	α_{iu}^+	$c_{2,i}(p_i - M\cdot A_i)+c_{1,i}+\overline{\delta}_i-\underline{\delta}_i$	$\frac{1}{\lvert\mathcal{G}\rvert}\sum_i\Big[\mu_u\lambda_i+(\Sigma_u^- A_i)\Big(2c_{2,i}+\frac{z_i}{S_i^-}\big(\overline{\delta}_i+\underline{\delta}_i\big)\Big)\Big]$	$\frac{1}{\lvert\mathcal{G}\rvert}\sum_i\Big[-\mu_u\lambda_i+(\Sigma_u^+ A_i)\Big(2c_{2,i}+\frac{z_i}{S_i^+}\big(\overline{\delta}_i+\underline{\delta}_i\big)\Big)\Big]$
	System-wide (OPF-SW-AB)	α_i^-	α_i^+		$\frac{1}{\lvert\mathcal{G}\rvert}\sum_i\Big((\Sigma_u A_i)\Big(2c_{2,i}+\frac{z_i}{S_i^-}\big(\overline{\delta}_i+\underline{\delta}_i\big)\Big)\Big)$	
Symmetric	Node-to-Node (OPF-N2N-SB)	α_{iu}	α_{iu}	$2c_{2,i}p_i + c_{1,i} + \overline{\delta}_i - \underline{\delta}_i$	$\frac{1}{\lvert\mathcal{G}\rvert}\sum_i\Big[\nu\lambda_i+(\Sigma^- A_i)\Big(2c_{2,i}+\frac{z_i}{S_i^-}\big(\overline{\delta}_i+\underline{\delta}_i\big)\Big)\Big]$	$\frac{1}{\lvert\mathcal{G}\rvert}\sum_i\Big[-\nu\lambda_i+(\Sigma^+ A_i)\Big(2c_{2,i}+\frac{z_i}{S_i^+}\big(\overline{\delta}_i+\underline{\delta}_i\big)\Big)\Big]$
	System-wide (OPF-SW-SB)	α_i	α_i		$\frac{1}{\lvert\mathcal{G}\rvert}\sum_i\big(2c_{2,i}s^2\alpha_i + z_i s\big(\overline{\delta}_i+\underline{\delta}_i\big)\big)$	

4.5 Discussion and Insights on Locational Energy and Balancing Prices

4.5.1 Symmetric vs Asymmetric Energy Pricing

In the asymmetric balancing schemes, the energy price λ_i reflects not only cost of generation through cost coefficients $c_{2,i}$ and $c_{1,i}$, and the generation capacity limits through duals $\overline{\delta}_i$ and $\underline{\delta}_i$, but also the expected generation adjusted by the expected real-time balancing efforts, i.e., $p_i - M \cdot A_i$. Therefore, the expected asymmetric balancing provision affects the LMPs by reducing or increasing the expected available generation at the generation nodes. The influence of the expected balancing provision on the LMPs does not occur in symmetric balancing markets, since the expected balancing provision equals zero.

4.5.2 Symmetric vs Asymmetric Balancing Pricing

The locational balancing prices (LBPs) in the asymmetric balancing frameworks include a term that relates the LMPs λ_i to the nodal expected asymmetric forecast error μ_u in (4.10b)–(4.10c), and to the expected system-aggregated forecast error ν in (4.16d)–(4.16e). Therefore, the asymmetric LBPs reflect the expected balancing need at the uncertain node and the LMP of the balancing generator.

4.5.3 Nodal vs System-Wide Balancing Pricing

It is of interest to understand and quantify how the introduction of uncertainty by RES affects the system balancing prices. This analysis can be done by evaluating the relationship between the LBPs and the system-wide balancing prices. To simplify such comparison, we will focus on the symmetric balancing frameworks, since the asymmetric balancing analysis leads to more complicated expressions which could hinder the economic interpretation of the results.

In a symmetric balancing participation design defined as generators covering the same proportion of the imbalance independently of the source, i.e., $\alpha_{iu}{=}\alpha_{iv},\ \forall i, u, v$ as in Section 4.4.3 the system-wide and node-to-node participation factors are equal:

$\alpha_i{=}\alpha_{iu}$, and $\alpha_i\boldsymbol{\Omega}{=}\sum_u(\alpha_{iu}\boldsymbol{\omega}_u)$; $\forall i, u$. It follows that:

$$S_i = \left\|A_i\Sigma^{1/2}\right\|_2 = \alpha_i s, \qquad \forall i. \tag{4.19}$$

It is possible to derive a relationship β_u between the LBPs and the system-wide balancing price, where

$$\beta_u = \frac{\chi_u}{\chi}, \qquad \forall u. \tag{4.20}$$

An analytical expression for (4.20) can be derived by factorizing (4.17g) in the following way:

$$\chi_u{=}\frac{1}{|\mathcal{G}|}\sum_i\left((\Sigma_u A_i)\left(2c_{2,i} + \frac{z_i}{S_i}\left(\overline{\delta}_i + \underline{\delta}_i\right)\right)\right), \quad \forall u \tag{4.21a}$$

using identity (4.19) and since $\alpha_{iv} = \alpha_i, \forall i, v$

$$\chi_u{=}\frac{1}{|\mathcal{G}|}\sum_i\left[\sum_v(\alpha_i s_{uv})\left(2c_{2,i}{+}z_i\frac{\overline{\delta}_i{+}\underline{\delta}_i}{\alpha_i s}\right)\right], \qquad \forall u \tag{4.21b}$$

$${=}\frac{1}{|\mathcal{G}|}\sum_i\left[\frac{\sum_v s_{uv}}{s^2}\left(2c_{2,i}s^2\alpha_i{+}z_i s\left(\overline{\delta}_i{+}\underline{\delta}_i\right)\right)\right], \qquad \forall u \tag{4.21c}$$

$${=}\frac{\sum_v s_{uv}}{s^2}\left[\frac{1}{|\mathcal{G}|}\sum_i\left(2c_{2,i}s^2\alpha_i{+}z_i s\left(\overline{\delta}_i{+}\underline{\delta}_i\right)\right)\right], \qquad \forall u \tag{4.21d}$$

where the term inside the square brackets equals the balancing price χ (4.18g). Using $s^2 = e\Sigma e = \sum_{v,w}\sigma_{vw}$ we get

$$\chi_u{=}\frac{\sum_v \sigma_{uv}}{\sum_{v,w}\sigma_{vw}}\chi, \qquad \forall u. \tag{4.21e}$$

Finally, by rearranging the terms to match β_u's definition (4.20)

$$\beta_u = \frac{\sum_v \sigma_{uv}}{\sum_{v,w}\sigma_{vw}}, \qquad \forall u. \tag{4.21f}$$

It must be noted that β_u does not depend on system parameters, variables, or duals. Thus, the nodal balancing price depends on the effect that the uncontrollable generator u has on the system-wide variance, i.e., the higher the introduced uncertainty by generator u, the higher the price that it must pay for deviations from its forecasted generation. It can be easily seen that $\sum_u \beta_u = 1$. This equivalence allows to understand the factor β_u as node u's contribution to the overall system balancing

price.

As the LBPs χ_u carry information on the marginal balancing cost that a node with uncertainty adds to the system, they can be used to incentivize system-beneficial RES deployment strategies. For example, a RES investor would prefer to install their RES project at a node with low, or ideally negative, correlation with the existing uncertain RES in the system. Here, necessary compensations for introducing uncertainty and increasing balancing requirements will be lower, possibly yielding a neutral or even negative value of β_u.

The balancing prices derived from the proposed framework highlight the value that the system as a whole derives from complementary RES generation,i.e., RES generators with negative correlation to other RES, since a RES that compensates the imbalance of others provides load balancing support and as such its balancing costs are lower.

4.6 Analysis of RES Costs

Typically, RES operators submit zero-cost bids to electricity market operators, reflecting their zero or near-zero marginal production cost. However, they inflict non-zero marginal cost to the system by driving the need for procuring balancing reserve products. This section compares two approaches to quantify these costs by (i) using the balancing payments to controllable generation resources and by (ii) using the marginal balancing cost. We show that both approaches can be equivalent.

4.6.1 Compensating Balancing Cost

We define the the balancing cost incurred by the system for compensating imbalances of a RES' forecast as C_u^{α} given by the sum of payments for balancing regulation towards reserve-providing generators:

$$C_u^{\alpha} = \chi_u \sum_i \alpha_{iu}, \qquad \forall u \tag{4.22a}$$

and since $\sum_i \alpha_{iu}$=1 we obtain:

$$C_u^{\alpha}=\chi_u=\frac{1}{|\mathcal{G}|}\sum_i\left[\frac{\sum_v \alpha_{iv}\sigma_{uv}}{S_i}\left[2c_{2,i}S_i+z_i\left(\overline{\delta}_i+\underline{\delta}_i\right)\right]\right],\forall u. \tag{4.22b}$$

The balancing compensation cost C_u^{α} paid by the RES at u depends on the uncertainty it introduces to the system ($\sigma_{u,u}$) and its correlation with other nodes v ($\sigma_{u,v}$). If the RES at u does not introduce uncertainty to the system, then C_u^{α}=0.

4.6.2 RES Costs as Marginal Balancing Costs

Since the RES are modelled with zero marginal operating cost, their revenue can be calculated as:

$$R_u = -\frac{\partial \mathcal{L}_{\text{SN}}}{\partial \text{w}_u}\cdot \text{w}_u, \qquad \forall u \tag{4.23}$$

where $\mathcal{L}_{\text{SN}}$ is the Lagrangian function for the OPF-N2N-SB under the node-to-node symmetric balancing framework presented in Section 4.4.2. If the standard deviation σ_u of $\boldsymbol{\omega}_u$ is proportional to its forecast injection, i.e. σ_u=$\kappa_u \text{w}_u$, and ζ_{uv} is the correlation coefficient between uncertain injections at nodes u and v [141]. Then, the marginal revenue for the RES resource is:

$$-\frac{\partial \mathcal{L}_{\text{SN}}}{\partial \text{w}_u}=\lambda_u-\sum_i\left(\frac{\sum_v \alpha_{iu}\alpha_{iv}\zeta_{uv}\kappa_u\sigma_v}{S_i}\left[2c_{2,i}S_i+z_i\left(\overline{\delta}_i+\underline{\delta}_i\right)\right]\right), \quad \forall u \tag{4.24}$$

where the positive part of expression (4.24) can be understood as the active power price paid to RES generator u, π_u^{p}, and the negative one as the cost associated with its stochastic generation, c_u. If the uncontrollable generation u introduces no uncertainty to the system, i.e., κ_u=0, then c_u=0. The operation cost of the RES generator is then given by:

$$C_u^{\text{w}} = c_u \text{w}_u, \qquad \forall u. \tag{4.25}$$

4.6.3 Cost Equivalence between the Compensating and Marginal Balancing Costs

The equivalence between C_u^{α} and C_u^{P} can be demonstrated by examining (4.25):

$$C_u^{\mathrm{w}} = c_u \mathrm{w}_u$$

$$= \mathrm{w}_u \sum_i \left(\frac{\sum_v \alpha_{iu}\alpha_{iv}\zeta_{uv}\kappa_u\sigma_v}{S_i} \left[2c_{2,i}S_i + z_i\left(\overline{\delta}_i + \underline{\delta}_i\right) \right] \right), \qquad \forall u \tag{4.26a}$$

$$= \sum_i \left(\frac{\sum_v \alpha_{iu}\alpha_{iv}\zeta_{uv}\kappa_u\mathrm{w}_u\sigma_v}{S_i} \left[2c_{2,i}S_i + z_i\left(\overline{\delta}_i + \underline{\delta}_i\right) \right] \right), \qquad \forall u \tag{4.26b}$$

since $\sigma_u = \kappa_u \mathrm{w}_u$ and $\sigma_{uv} = \zeta_{uv}\sigma_u\sigma_v$

$$C_u^{\mathrm{w}} = \sum_i \left(\frac{\sum_v \alpha_{iu}\alpha_{iv}\sigma_{uv}}{S_i} \left[2c_{2,i}S_i + z_i\left(\overline{\delta}_i + \underline{\delta}_i\right) \right] \right), \qquad \forall u \tag{4.26c}$$

$$= \alpha_{iu} \sum_i \left(\frac{\sum_v \alpha_{iv}\sigma_{uv}}{S_i} \left[2c_{2,i}S_i + z_i\left(\overline{\delta}_i + \underline{\delta}_i\right) \right] \right), \qquad \forall u \tag{4.26d}$$

replacing χ_u

$$C_u^{\mathrm{w}} = \chi_u \sum_i \alpha_{iu} = C_u^{\alpha}, \qquad \forall u. \tag{4.26e}$$

As shown in Eq. (4.26e), the total operating cost of uncontrollable generation resources is equivalent when computed from balancing payments C_u^{α} and marginal costs C_u^{w}. However, the latter holds only if the total operating cost of uncontrollable generation resources are computed under the assumption that the variances, $\sigma_{u,v}$, are proportional to the injected power and fixed node-to-node correlation factors, i.e., $\sigma_u = \kappa_u \mathrm{w}_u$. If these assumptions do not hold, the total operating cost of uncontrollable generation resources can only be computed via the balancing payments in (4.22b).

4.7 Numerical Experiments

In this section, the proposed stochastic market-clearing model OPF-N2N-AB and its modifications from Section 4.4 are evaluated on a modified IEEE 118-bus case [134]. The experiments were conducted using Julia 1.53, JuMP 0.21.6 and Mosek [144] on an Intel i7-1165G7 processor clocked at 2.80GHz with 16 GB of RAM. The

code and data supplement can be downloaded from [145].

4.7.1 Test Case and Stochastic Data

For this case study, we add 11 utility-scale wind farms to the IEEE-118 bus test-system as stochastic resources. Table 4.2 indicates their placement in the system. Forecasts and forecast error distributions are emulated from real data of onshore wind farms in different European regions collected between January 1st, 2020 and October 1st. This data is available on the ENTSO-E transparency database [146]. Table 4.2 summarizes the used wind power data. Note, that the time series analyzed were scaled per unit of capacity (p.u.o.C).

To study the impact of stochastic generation at different penetration levels, we create four renewable penetration scenarios by scaling the installed capacity of each wind farm by 50%, 100%, 200%, and 400%. In these scenarios, the available generation from all wind farms covers 4.8%, 9.7%, 19.4%, and 38.8% of total demand, respectively.

Every wind farm was assigned an independent normal distribution $\boldsymbol{\omega}_u \sim \mathcal{N}(0, \sigma_u)$ with σ_u being estimated from data. From these parent distributions truncated distributions were inferred. For asymmetric balancing designs, we generate truncated Normal distributions $\boldsymbol{\omega}_u^+$ and $\boldsymbol{\omega}_u^+$ from $\boldsymbol{\omega}_u$ with the following parameters:

$$\sigma_u^{\pm} = \sigma_u \sqrt{\frac{2\pi - 4}{2\pi}}, \quad \mu_u^{\pm} = \sigma_u \sqrt{\frac{2}{\pi}} \tag{4.27}$$

We set the chance-constraint confidence level at $(1-\epsilon)$=0.99, obtaining $z_i \approx 9.95$

Table 4.2: Forecasts w_u mean and standard deviations at node u [p.u.o.C.]

u	3	8	11	20	24	26	31	38	43	49	53
w_u	0.112	0.801	0.61	0.086	0.142	0.0	0.056	0.137	0.353	0.207	0.305
σ_u	0.1	0.26	0.22	0.25	0.22	0.19	0.14	0.44	0.17	0.13	0.07
μ_u	0.1544	0.4101	0.3539	0.3962	0.3483	0.3029	0.2267	0.7016	0.2791	0.2113	0.1106
σ_u^-	0.06	0.155	0.142	0.116	0.121	0.097	0.087	0.279	0.103	0.079	0.039
σ_u^+	0.056	0.155	0.126	0.19	0.142	0.134	0.084	0.251	0.108	0.081	0.045

with the Chebyshev inequality as in [69].

4.7.2 Solution Methodology

Chance-constrained market clearing procedures as proposed in [131, 132, 133, 134] can be solved in a single or two-step[2] procedure using off-the-shelf solvers. However, solving OPF-N2N-AB and its modifications shown in Section 4.4 requires dealing with bilinear terms in the objective function. Therefore, we use McCormick envelopes to convexify the bilinear terms in (4.9a). The obtained envelopes are then sequentially tightened around the initial operating point or one that was produced by the previous iteration to improve the approximation. The proposed sequential solution approach based on using off-the-shelf solvers is summarized as follows:

- *Step 1.* Obtain a solution to a convex approximation of the original OPF-N2N-AB problem.
- *Step 2.* Tighten the convex approximation around *Step 1*'s solution by using a decreasing scalar factor to reduce the distance between its obtained operation point and the current bounds.
- *Step 3.* Stop if the convex approximation is good enough. If not, update and return to *Step 1* and repeat.

Two important notes must be made on the proposed solution methodology. First, the convexified problem always yields a feasible solution to the OPF-N2N-AB, this corresponds to the fact that the convexification is introduced to the problem's objective, rather than to its constraints. Second, an optimal solution $\hat{x}^*$ of the convexified problem provides an upper bound to the objective of the original non-convex problem, i.e., $C(x^*) \leq C(\hat{x}^*)$, where $C(\cdot)$ is the objective function of OPF-N2N-AB, and x^* is an optimal solution to the original non-convex version of OPF-N2N-AB. On the other hand the optimal objective value of the convexified problem $\hat{C}(\hat{x}^*)$ provides a lower bound to the objective of the original non-convex problem, i.e.,

[2]To derive prices from a chance-constrained unit commitment problem, it is necessary to run the problem a second time with fixed binary variable to obtain prices from dual multipliers. See [132].

$\hat{C}(\hat{x}^*) \leq C(x^*)$. Therefore, we can observe that $\hat{C}(\hat{x}^*) \leq C(x^*) \leq C(\hat{x}^*)$. Whereas $C(x^*)$ cannot be computed directly, both values $\hat{C}(\hat{x}^*)$ and $C(\hat{x}^*)$ can. We evaluate as the stopping criteria on *Step 3* the approximation accuracy $100(^{C(\hat{x}^*)}/_{\hat{C}(\hat{x}^*)} - 1)$. Once a the approximation accuracy is below the set tolerance level, we can derive the prices using the convexification of model OPF-N2N-AB.

4.7.3 Comparison of Balancing Frameworks

System-wide and node-to-node balancing

First, we compare the symmetric balancing in the system-wide and node-to-node cases. Both balancing frameworks are solved using Mosek. Table 4.3 summarizes the main results for our base scenario with a renewable penetration rate of 9.7%.

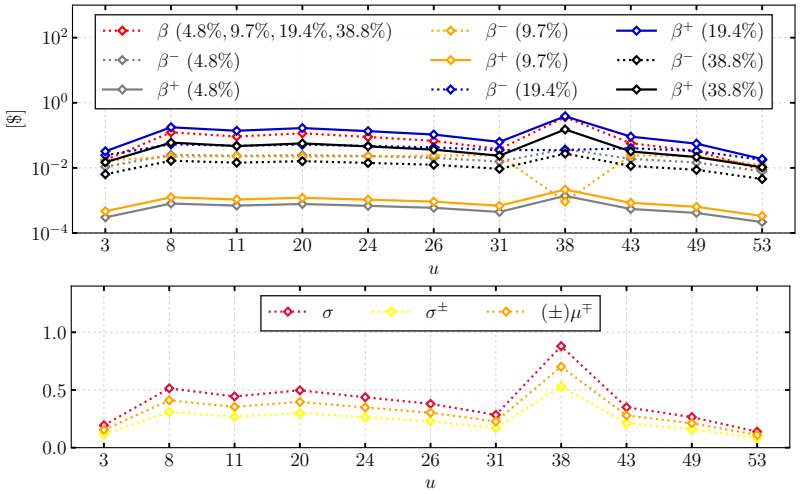

Figure 4.3: Relationship between $\beta_u^{(\pm)}$ and stochastic generation parameters.

Our results show that symmetric, zero-mean balancing yields the same objective value in both system-wide and node-to-node frameworks. Moreover, we observe regarding the dual values χ and χ_u, that the sum of the nodal balancing prices equals the system-wide balancing price, i.e., $\sum_u \chi_u = \chi$, as shown analytically in Eq. (4.20) above.

The dependence of χ_u on the variance σ_u^2 is illustrated in Figure 4.3. A node-to-node balancing framework provides better pricing signals by reflecting the influence the forecast error variance introduced by the RES has on the price paid for its

balancing.

Asymmetric balancing provision with varying amounts of renewable penetration

Next, we study the asymmetric balancing provision as proposed in Section 4.7.2 with different renewable penetration levels. To facilitate comparison, results are presented alongside those obtained using symmetric balancing (discussed in Section 4.7.3 above) in Figure 4.4.

Figure 4.4 contains the best objective value found in the sequential process described in Section 4.7.2, such that $C(\hat{x}^*) \approx C(x^*)$. Further it shows the payments collected from consumers (λD), payments disbursed to wind farms (λW) and conventional generators ($\sum_i \Pi_i$), respectively for the studied renewable penetration levels of 4.8%, 9.7%, 19.4%, and 38.8%.

With an increasing penetration of wind generation, system cost given by objective value $C(x^*)$ are decreasing due to the greater availability of low-cost energy from RES. This leads to notable differences in payments made to conventional generators. However, for low renewable penetration rates, the total cost barely change between market frameworks.

Our experiments confirm the revenue adequacy property of the prices, i.e., $\lambda D = \lambda W + \sum_i \Pi_i$. Table 4.4 shows consumer payments, generator revenues and generation costs using different market designs. The difference in consumer payments between asymmetric and symmetric balancing markets is defined as $\Delta\lambda D$. The

Table 4.3: Computational Results for Markets with Symmetric Balancing Provision (SW, N2N)

	SW	N2N
z^* [\$/h]	127020.2	127020.2
χ	22.9	-

u	3	8	11	20	24	26	31	38	43	49	53	$\sum$
χ_u	0.4	2.822	2.102	2.634	2.036	1.539	0.862	8.258	1.307	0.749	0.205	22.9

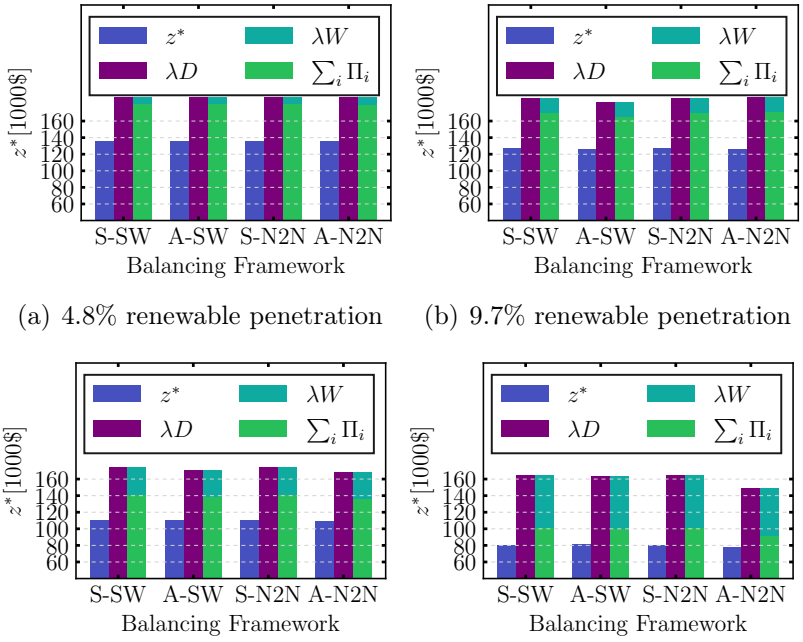

(a) 4.8% renewable penetration (b) 9.7% renewable penetration

(c) 19.4% renewable penetration (d) 38.8% renewable penetration

Figure 4.4: Optimization results under different balancing frameworks and renewable penetration. Where z^* represents the objective value, λD consumer payments, λW wind payments and $\sum_i \Pi_i$ the generators' revenue.

approximation error introduced by the convexification is captured in the term *err*. As summarized in Figure 4.4 and Table 4.4, markets with asymmetric node-to-node balancing show that significant reductions in consumer payments are possible. Evaluating the solution obtained with the relaxed model yields an approximation error of 1.79%, which is not enough to explain consumer payment reductions of well over 9%.

Two main takeaways can be drawn from the obtained results. First, the approximation method works very well for system-wide asymmetric balancing markets. Given a solution, the objective differs by less than 0.0026% from the exact objective. Second, this market design yields consistent reductions in consumer payments compared to symmetric balancing strategies.

Figure 4.5 provides insights as to how prices are formed in the proposed asymmetric node-to-node market framework. We can observe that the dual values $\overline{\delta}$ are proportional to the system's renewable penetration level. This is due to less dispatchable generating capacity being required. Thus, less expensive generators must

Table 4.4: Consumer Payments λD and Approximation Errors by Scenario

Scenario		4.8%	9.7%	29.4%	38.8%
S-SW	λD [\$\h]	188965.12	188082.21	174123.79	164091.47
A-SW	λD [\$\h]	188940.56	182724.69	170674.6	163494.45
	$\Delta\lambda D$ [%]	-0.013	-2.85	-1.98	-0.364
	err [%]	4.0e-5	1.0e-4	3.8e-4	2.63e-3
S-N2N	λD [\$\h]	188965.16	188082.55	174123.41	164091.43
A-N2N	λD [\$\h]	188869.01	188465.01	168506.01	148982.8
	$\Delta\lambda D$ [%]	-0.051	+0.2	-3.23	-9.21
	err [%]	0.70217	1.01088	1.15133	1.79429

be dispatched to clear the market. Simultaneously, the variance introduced into the system increases with higher onshore wind capacity, which leads to tighter chance constraints (4.9i) and (4.9h). Accordingly, more dispatchable generation capacity must be reserved for balancing, which leads to the increase in dual values and, subsequently, prices.

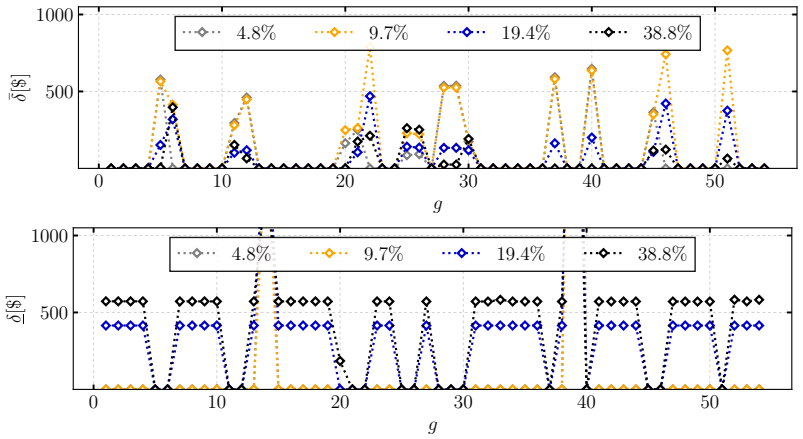

Figure 4.5: Dual values $\underline{\delta}$ and $\overline{\delta}$ for different renewable capacity levels.

4.8 Conclusion

In this chapter, we have described and analyzed the economic impact of four approaches for the provision of balancing regulation in a chance-constrained optimal power flow: system-wide symmetric, node-to-node symmetric, system-wide asym-

metric, and node-to-node asymmetric. Both the locational marginal electricity prices and the balancing regulation prices are derived and are proven to establish a competitive equilibrium for all the balancing frameworks. The asymmetric node-to-node regulation provides the lowest balancing prices while introducing to the electricity prices a dependence on the generation participation in the balancing provision. We have shown that asymmetric reserve provision facilitates more efficient reserve pricing. This it is more relevant as the renewable generation capacity increases. Additionally, the other configurations are proven to be particular subcases of the asymmetric node-to-node regulation one, thus yielding higher operational costs.

Chapter 5

Conclusions and Future Work

In this thesis, we aimed to provide a family of mathematical models for enhanced characterization of flexibility measures available to the electric power systems. Under the framework of convex optimization theory, we approached from three angles the flexibility provision in electric power systems. We focus our investigation on the mathematical modeling for the representation of i) the characterization of electric energy storage systems for their use in operation and planning models, ii) a market design for integrated heat-and-power microgrids, and iii) wholesale stochastic electricity markets with asymmetric and node-to-node balancing provision for renewable variations.

5.1 Conclusions

The general conclusions of the doctoral research presented in this thesis are listed as follows.

1. Pertaining electric energy storage characterization in operation scheduling models:

    - The use of ideal energy storage characterization models with constant efficiency and power limits does not properly represent the operational characteristics of batteries. It was evindenced in the performed studies that the use of ideal models leads to overestimating the flexibility pro-

vided by storage units. This overestimation results in faliure to fulfill the real-time dispatch commitments.

- At higher renewable penetration levels, there is a greater mismatch between the scheduled dispatch of energy storage units with ideal models and their real-time operation. Thus, higher levels of real-time balancing must be procured from more expensive flexibility sources, which increase the system operation costs.
- The lifting of the energy storage operational variables, power, and stored energy, to a three-dimensional space, enables the representation of non-constant efficiencies and power limits as linear constraints in optimization problems.
- The lifted three-dimensional representation can then be used in linear programming (LP) and mixed-integer linear programming (MILP) models to characterize energy storage operation more accurately. Unlike MILP models, LP models preserve computational tractability while also accurately representing the storage performance with a mean error of 1.2% between the exact and approximated operation region.

2. Pertaining the heat exchange between integrated heat-and-power microgrids:

- Heat exchange markets between integrated heat-and-power microgrids can be established based on convex optimization models with decomposable structure, preserving operation independence and privacy, since they do not exchange technical parameters but only the desired exchange quatinty and its bid price.
- The exchange of heat between multi-energy microgrids increases their electric operational flexibility by expanding the range in which the electricity generation can operate.
- Duality theory provides a framework for the derivation of heat exchange prices. The derived prices constitute a competitive equilibrium, with each participating microgrid maximizing its modeled operational profits.

- The heat exchange prices are dependent on three main factors: i) the interconnection efficiency, ii) the interconnection capacity, and iii) the local heating price at the importing microgrid.

3. Pertaining the design of energy and reserves electricity markets:

   - The use of stochastic energy and reserves markets must represent the asymmetric nature of renewable generation forecast errors. There exists evidence of renewable generation asymmetric forecast errors in several existing markets.
   - Gaussian distributions and system-wide aggregation for the representation for renewable forecast errors overestimates the required reserve levels in the system, resulting in greater balancing expenses.
   - The asymmetric and node-to-node provision of generation balancing reduces the system operation costs. The costs' reductions could boost new renewable investment levels.
   - The pricing of asymmetric and node-to-node balancing reflects the uncertainty introduced in the system by renewable energy sources, i.e., sources with higher forecast error variance have higher associated balancing prices. Additionally, this type of pricing reflects the statistical correlation between the generation uncertainty of renewable energy sources at different locations.
   - The dependence between the balancing prices and the uncertainty of renewable energy sources serves as a signal for investors to locate renewable generation projects at zones with a negative correlation with the existing system's renewable sources. In this manner, their balancing costs would be further reduced even with larger shares of renewable generation sources.
   - The derived asymmetric and node-to-node balancing prices reflect the compensation costs that the market operation could charge renewable energy sources for introducing uncertainty in the system operation.

5.2 Discussion and Future Work Recommendations

Considering the central role that the electric power systems and renewable generation will play in the future technological development of the energy sector, the wide range of flexibility measures in electric networks and their possible interconnection with other energy systems provide a challenging and attractive field for the development of new markets, and communication, control, and planning strategies for the flexible power systems operation.

As seen in this thesis, there is no unified framework for quantifying a system's flexibility. The lack of consensus in the literature corresponds to the extensive array of flexibility measures within electric power systems and the additional layers of complexity introduced by its interconnection with other energy systems. Unlocking flexibility through the centralized operation of multi-energy systems, albeit technically feasible, must also correspond with the seamless coordination of the different energy markets, which operate at different time scales [8].

An additional limitation for the flexibility analysis of electric power systems is the gap existing between the control layer (order of minutes) in which the flexibility measures operate and the planning horizon (in years) for the sizing and selection of these measures. The flexibility study must also include the stochastic nature of variable renewable resources, which increases the mathematical complexity of whole system consideration. Finally, decentralized control and communication infrastructures must be developed to coordinate the different flexibility and energy systems to enable a fast and cost-effective response to variable renewable generation.

The flexible development of future power systems will be heavily influenced by understanding the characteristics of the technical, interconnection, and market mechanism design resources available to electric networks.

Sound developments on convex optimization and mathematical modeling should be at the center of our recommendation for unlocking efficiently flexibilities from different sources in modern power systems. Although being at the foundations for a proper flexibility characterization, such tools should be complemented with other regulatory nature strategies to achieve more significant impact. Additionally, the

simultaneous implementation of several sources of flexibility in the power system calls for further investigation to estimate their degree of substituteness and complementness. However, we have devoted our research efforts to quantify the impact of different flexibility solutions for power systems with a large share of renewables. Finally, power systems are complex per se, where multiple agents and bodies simultaneously interact while at the same time being heavily affected by externalities. Such complex interaction analysis will be part of our future research avenues, being the current thesis one of the fundamental mathematical building blocks for the flexibility characterization to further expand.

THIS PAGE INTENTIONALLY LEFT BLANK

Appendix A

Mixed-integer linear programming (MILP) battery characterization

This appendix presents in Model A.1 the formulation of the mixed-integer linear programming for the piecewise linearization of the battery performance characterization based on the triangle method presented in [93]. The state of the battery, discharge and charge, is controlled by the binary variables z_t^{cha} and z_t^{dis} in (A.1a). In this method, the SOC, the p^{out}, and the p^{in} are taken as reference dimensions with sampling values in sets j, k, and l, respectively. The values of the variables SOC_t, the $p_t^{\text{out/in}}$, and $p_t^{\text{in/cha}}$ are obtained as a convex combination of their repective sampling points in (A.1b)-(A.1f) with the use of the real auxiliary variables $\alpha_{j,k,t}$ and $\alpha_{j,l,t}$, respectively used for the discharging and charging processes. The selection of the approximating segments is done by teh special order set (SOS) constraints (A.1g) and (A.1h). Expressions (A.1i) and (A.1j) define the linear combination of the sampling points. Finally, constraints (A.1k) and (A.1l) define the relationship between the sampling points and the selected approximation segments.

Model 9 Li-ion battery mixed-integer linear programming model [MILP]

Variables:

e_t, SOC_t	battery energy level (absolute and relative values)	[Wh,–]
$p_t^{\text{dis}}, p_t^{\text{cha}}$	discharging and charging power	[W]
$p_t^{\text{out}}, p_t^{\text{in}}$	power outgoing and incoming at the cells	[W]
$z_t^{\text{cha}}, z_t^{\text{dis}} \in \{0,1\}$	Binary variables indicating if the battery charging or discharging.	
$\alpha_{j,k,t}$	Variable associated with each discharging breakpoint (j,k).	
$\alpha_{j,l,t}$	Variable associated with each charging breakpoint (j,l).	
$\beta_{j,k,t}^{\text{up}}, \beta_{j,k,t}^{\text{low}} \in \{0,1\}$	Binary variables associated with the upper and lower triangles of the rectangle corresponding to the intervals $[\widehat{SOC}_j, \widehat{SOC}_{j+1}]$ and $[\hat{P}_k^{\text{out}}, \hat{P}_{k+1}^{\text{out}}]$, for the characterization of the discharge curve.	
$\beta_{j,l,t}^{\text{up}}, \beta_{j,l,t}^{\text{low}} \in \{0,1\}$	Binary variables associated with the upper and lower triangles of the rectangle corresponding to the intervals $[\widehat{SOC}_j, \widehat{SOC}_{j+1}]$ and $[\hat{P}_l^{\text{in}}, \hat{P}_{l+1}^{\text{in}}]$, for the characterization of the charge curve.	

Constraints:

$$z_t^{\text{cha}} + z_t^{\text{dis}} \leq 1, \qquad \forall t \quad \text{(A.1a)}$$

$$SOC_t = \sum_j \left[\sum_k \alpha_{j,k,t} + \sum_k \alpha_{j,l,t} \right] \cdot \widehat{SOC}_j, \qquad \forall t \quad \text{(A.1b)}$$

$$p_t^{\text{out}} = \sum_j \sum_k \alpha_{j,k,t} \cdot \hat{P}_k^{\text{out}}, \qquad \forall t \quad \text{(A.1c)}$$

$$p_t^{\text{dis}} = \sum_j \sum_k \alpha_{j,k,t} \cdot \hat{P}_{j,k}^{\text{dis}}, \qquad \forall t \quad \text{(A.1d)}$$

$$p_t^{\text{in}} = \sum_j \sum_l \alpha_{j,l,t} \cdot \hat{P}_l^{\text{in}}, \qquad \forall t \quad \text{(A.1e)}$$

$$p_t^{\text{cha}} = \sum_j \sum_l \alpha_{j,l,t} \cdot \hat{P}_{j,l}^{\text{cha}}, \qquad \forall t \quad \text{(A.1f)}$$

$$\sum_j \sum_k (\beta_{j,k,t}^{\text{up}} + \beta_{j,k,t}^{\text{low}}) = z_t^{\text{dis}}, \qquad \forall t \quad \text{(A.1g)}$$

$$\sum_j \sum_l (\beta_{j,l,t}^{\text{up}} + \beta_{j,l,t}^{\text{low}}) = z_t^{\text{cha}}, \qquad \forall t \quad \text{(A.1h)}$$

$$\sum_j \sum_k \alpha_{j,k,t} = z_t^{\text{dis}}, \qquad \forall t \quad \text{(A.1i)}$$

$$\sum_j \sum_l \alpha_{j,l,t} = z_t^{\text{cha}}, \qquad \forall t \quad \text{(A.1j)}$$

$$\alpha_{j,k,t} \leq \beta_{j,k,t}^{\text{up}} + \beta_{j,k,t}^{\text{low}} + \beta_{j-1,k,t}^{\text{low}} + \beta_{j,k-1,t}^{\text{up}} + \beta_{j-1,k-1,t}^{low} + \beta_{j-1,k-1,t}^{\text{up}}, \qquad \forall t \quad \text{(A.1k)}$$

$$\alpha_{j,l,t} \leq \beta_{j,l,t}^{\text{up}} + \beta_{j,l,t}^{\text{low}} + \beta_{j-1,l,t}^{\text{low}} + \beta_{j,l-1,t}^{\text{up}} + \beta_{j-1,l-1,t}^{low} + \beta_{j-1,l-1,t}^{\text{up}}, \qquad \forall t. \quad \text{(A.1l)}$$

Appendix B

Stochastic Distribution Unit Commitment

This appendix presents the full formulation of the stochastic unit commitment (UC) problem used in Section 2.6's test case for a distribution network with renewable generation, energy storage and reserves, Model 10. The UC problem is modeled as a two-stage stochastic optimization problem on which the first stage represents the generation start-up/shut-down commitment, energy purchase and reserves allocation, on the second stage the reserves realization, generation and storage operation are defined. The model below was presented in [147] and fully developed in [75].

The objective of the UC in a distribution system is to schedule the distributed generation and electricity exchange with the main grid at a minimum cost, while satisfying its demand and network constraints. The minimization of the generation operation cost and the economic exchange with the main grid is stated in (B.1). The generation start-up and shut-down costs are recovered as Φ (B.2) and the fuel consumption costs in W_ω (B.5). K defines the electricity exchange costs with the main grid (B.3). The total reserve allocation cost Υ, (B.4), is given by the requested capacity $r_t^{\text{up/dw}}$ and the cost associated to it $K_{h(t)}^{\text{up/dw}}$. Increasing the power output by $\hat{r}_{t,\omega}^{\text{up}}$ during the operation stage will incur the system operator in an additional costs with price $K_{h(t)}^{\text{up}}$ in €/MWh, whereas reducing its consumption will provide him revenue at $K_{h(t)}^{\text{dw}}$. The reserve realization cost is given by (B.6).

Equation (B.7) defines the net power exchanged with the grid during the opera-

tion stage as the sum of the scheduled import and export, plus the realized reserved. Constant hourly power exchange with the main grid is set by (B.8). Constraints (B.9) and (B.10) set the upper bound for the allocation of upward and downward reserves in terms of the scheduled power import p_t^{imp} and the maximum import capacity $\overline{P}^{\text{imp}}$. The bounds for reserve allocation based on the market rules are presented in (B.11) and (B.12). The limits for the reserves realization during the operational stage are set by (B.13) and (B.14). Finally, the hourly market nature for the reserve allocation is guaranteed by (B.15).

The power flow equations are set by (B.16)-(B.22). Equations (B.16) and (B.17) represent the active and reactive nodal power balances for each time step t and scenario ω. The active power flow through line (n, m) is given in terms of its conductance $G_{n,m}$ and susceptance $B_{n,m}$ by equation (B.18), where c_{nm} and s_{nm} are the variables used to respectively represent the branch relationships $V_n V_m \cos(\theta_n - \theta_m)$ and $V_n V_m \sin(\theta_n - \theta_m)$. Equation (B.19) provides the lines' reactive power flow in terms of their conductance, susceptance and line charging susceptance $b_{n,m}^{\text{cha}}$. To keep the dimensional equivalence between both sides of expressions (B.18) and (B.19), the right-hand sides are multiplied by the base value of the apparent power S_{base} in MVA. The SOCP relaxation of the expression $c_{nm}^2 + s_{nm}^2 = c_{nn} c_{mm}$ is given by (B.20), while the trigonometric symmetries of c_{nm} and s_{nm} are presented in (B.21) and (B.22). The voltage limits at the nodes and the thermal rates for the power lines are given by (B.23) and (B.24).

The generation start-up and shut-down costs are respectively given by (B.25) and (B.26). Generation ramp constraints are given by (B.27) and (B.28), whereas capacity limits are set by (B.29) and (B.30). The storage operation with non-constant efficiency can be described in a linear way by (B.31)–(B.42). The battery energy balance is given by (B.31), where p_t^{batt} is the net power delivered to the battery cell (positive if charging, negative if discharging), and defined in (B.32). The discharging and charging powers are respectively described by equations (B.33)–(B.34) and (B.35)–(B.36). The SOC as a linear combination of the sampling points is presented by (B.37), while its definition by (B.38). The linear combination of the characteristic points during discharge and charge is ensured by (B.39)–(B.42).

Model 10 Stochastic Distribution Unit Commitment

Indexes:

g	conventional generation unit index
j, k	sampling indexes for the battery charging and discharging operation points
n, m	node index
s	index for the battery storage system
t	time step index
ω	index for probabilistic scenarios

Sets:

$\mathcal{G}(n)$	set containing the generators connected at n
$h(t)$	hour containing time step t
$\mathcal{J}, \mathcal{K}$	set for battery operation sampling points
$\mathcal{L}$	set containing every existing line (n, m)
$\mathcal{N}(n)$	set containing the nodes m connected to n
$\mathcal{S}(n)$	set containing the storage units connected at n

Parameters:

b_{nm}^{cha}	line charging susceptance of branch (n, m)	[p.u.]
$\overline{E}$	battery capacity	[MWh]
$\overline{F}_{nm}$	current limit for line (n, m)	[p.u.]
G_{nm}, B_{nm}	conductance and susceptance of line (n, m)	[p.u.]
$K_h^{\text{imp}}, K_h^{\text{exp}}$	import and export cost during h	[€/MWh]
$\hat{K}_h^{\text{r,up}}, \hat{K}_h^{\text{r,dw}}$	up and down reserve deployment cost during h	[€/MWh]
$\underline{P}_g, \overline{P}_g$	active power generation limits for g	[MW]
$P_n^{\text{D}}, Q_n^{\text{D}}$	demanded active and reactive power at n	[MW, MVAr]
$\widehat{P}_i^{\text{dis}}, \widehat{P}_j^{\text{cha}}$	sample points for the power discharged to and charged from the electric grid	[MW]
$\overline{P}^{\text{imp}}$	power import limits	[MWh]
$\widehat{P}_i^{\text{out}}, \widehat{P}_j^{\text{in}}$	sample points for power leaving and entering the battery cell	[MW]
$P_{n,t}^{\text{RES}}$	active power generated by the renewable resource at n during t	[MW]
$\underline{Q}_g, \overline{Q}_g$	reactive power limits for g	[MVAr]
$\overline{R}^{\text{up}}, \overline{R}^{\text{dw}}$	up and down reserve power limits	
RU_g, RD_g	ramp-up and ramp-down limits for g.	[MWh]
S_{base}	base value for the apparent power	[MVA]
$\widehat{SOC}_i, \widehat{SOC}_j$	state-of-charge sample points for the discharging and charging processes	
$\underline{V}_n, \overline{V}_n$	voltage limits at n	[p.u.]
$\Gamma_n^{\text{grid}}, \Gamma_n^{\text{RES}}$	binary indicator of connection to the main grid and the renewable resources at n	
Δ	duration of time step in hours	[h]
ϕ^{fuel}	fuel consumption costs of g	[€/MWh]
$\phi_g^{\text{su}}, \phi_g^{\text{sd}}$	costs related to g's start-up & shut-down	[€]

Model 10 Stochastic Distribution Unit Commitment [continued]

First-stage Variables:

K	total economic exchange with the grid	[€]
$p_t^{\text{imp}}, p_{t,}^{\text{exp}}$	imported and exported power committed day-ahead	[MW]
$r_t^{\text{up}}, r_t^{\text{dw}}$	allocated up/down reserve during t	[MWh]
$z_{g,t} \in \{0,1\}$	on/off status of generating unit g on t	
Φ	total scheduling costs of generators	[€]
Υ	total reserve allocation cost	[€]

Second-stage Variables:

$c_{nm,t,\omega}$	$\lvert V_{n,t,\omega}\rvert\lvert V_{m,t,\omega}\rvert \cos(\theta_{n,t,\omega} - \theta_{m,t,\omega})$	[p.u.]
$e_{t,\omega}, SOC_{t,\omega}$	Battery energy level (absolute and relative values)	[MWh, -]
$p_{g,t,\omega}, q_{g,t,\omega}$	generated active and reactive power	[MW, MVAr]
$p_{nm,t,\omega}, q_{nm,t,\omega}$	active and reactive power flow through line (n,m)	[MW, MVAr]
$p_{t,\omega}^{\text{batt}}$	Net battery power charged/discharge	[MW]
$p_{t,\omega}^{\text{dis}}, p_{t,\omega}^{\text{cha}}$	Discharging and charging power during t and scenario ω	[MW]
$p_{t,\omega}^{\text{grid}}$	net real-time power exchanged with the main grid	[MW]
$p_{t,\omega}^{\text{out}}, p_{t,\omega}^{\text{in}}$	Power outgoing and incoming at the battery cells	[MW]
$\hat{r}_{t,\omega}^{\text{up}}, \hat{r}_{t,\omega}^{\text{dw}}$	real-time deployed up/down reserves.	[MWh]
$s_{nm,t,\omega}$	$\lvert V_{n,t,\omega}\rvert\lvert V_{m,t,\omega}\rvert \sin(\theta_{n,t,\omega} - \theta_{m,t,\omega})$.	[p.u.]
$x_{j,t,\omega}, y_{k,t,\omega}$	Auxiliary variables for the sample sets $\mathcal{J}$ and $\mathcal{K}$	
W_ω	total operational costs of generators for scenario ω	[€]
$\phi_{g,t,\omega}^{\text{su}}, \phi_{g,t,\omega}^{\text{sd}}$	start-up and shut-down cost for g on t and scenario ω	[€]
Θ_ω	total real-time reserves deployment cost for scenario ω	[€]

Model 10 Stochastic Distribution Unit Commitment [continued]

Objective:

$$\text{min.} \quad K + \Upsilon + \Phi + \mathbb{E}[\Theta_\omega + W_\omega] \tag{B.1}$$

Constraints:

Costs:

$$\Phi = \sum_{g,t} \phi^{\text{su}}_{g,t} + \phi^{\text{sd}}_{g,t} \tag{B.2}$$

$$K = \Delta_t \cdot \sum_t \left[K^{\text{imp}}_{h(t)} p^{\text{imp}}_t + K^{\text{exp}}_{h(t)} p^{\text{exp}}_t \right] \tag{B.3}$$

$$\Upsilon = \Delta_t \cdot \sum_t \left(K^{\text{r,up}}_{h(t)} r^{\text{up}}_t + K^{\text{r,dw}}_{h(t)} r^{\text{dw}}_t \right), \tag{B.4}$$

$$W_\omega = \Delta_t \cdot \sum_{g,t} \left(\phi^{\text{fuel}}_g p_{g,t,\omega} \right), \qquad \forall \omega \tag{B.5}$$

$$\Theta_\omega = \Delta_t \cdot \sum_t \left[\hat{K}^{\text{r,up}}_{h(t)} \hat{r}^{\text{up}}_{t,\omega} + \hat{K}^{\text{r,dw}}_{h(t)} \hat{r}^{\text{dw}}_{t,\omega} \right], \qquad \forall \omega \tag{B.6}$$

Reserves:

$$p^{\text{grid}}_{t,\omega} = p^{\text{imp}}_t - p^{\text{exp}}_t + \hat{r}^{\text{up}}_{t,\omega} - \hat{r}^{\text{dw}}_{t,\omega}, \qquad \forall t, \omega \tag{B.7}$$

$$p^{\text{imp/exp}}_t = p^{\text{imp/exp}}_{t'}, \qquad \forall (t,t') \in h(t) \tag{B.8}$$

$$\overline{P}^{\text{imp}} \geq p^{\text{imp}}_t + r^{\text{up}}_t, \qquad \forall t \tag{B.9}$$

$$0 \leq p^{\text{imp}}_t - r^{\text{dw}}_t, \qquad \forall t \tag{B.10}$$

$$0 \leq r^{\text{up}}_t \leq \overline{R}^{\text{up}}, \qquad \forall t \tag{B.11}$$

$$0 \leq r^{\text{dw}}_t \leq \overline{R}^{\text{dw}}, \qquad \forall t \tag{B.12}$$

$$0 \leq \hat{r}^{\text{up}}_{t,\omega} \leq r^{\text{up}}_t, \qquad \forall t, \omega \tag{B.13}$$

$$0 \leq \hat{r}^{\text{dw}}_{t,\omega} \leq r^{\text{dw}}_t, \qquad \forall t, \omega \tag{B.14}$$

$$r^{\text{up/dw}}_t = r^{\text{up/dw}}_{t'} \qquad \forall (t,t') \in h(t) \tag{B.15}$$

Electric Flow:

$$P^{\text{D}}_{n,t,\omega} = \Gamma^{\text{grid}}_n \cdot p^{\text{grid}}_{t,\omega} + \sum_{g \in \mathcal{G}(n)} p_{g,t,\omega} + \sum_{s \in \mathcal{S}(n)} p^{\text{batt}}_{s,t,\omega} + \Gamma^{\text{RES}}_n \cdot P^{\text{RES}}_{n,t,\omega} - \sum_{m \in \mathcal{N}(n)} p_{nm,t,\omega}, \quad \forall n,t,\omega \tag{B.16}$$

$$Q^{\text{D}}_{n,t,\omega} = \sum_{g \in \mathcal{G}(n)} q_{g,t,\omega} - \sum_{m \in \mathcal{N}(n)} q_{nm,t,\omega}, \qquad \forall n,t,\omega \tag{B.17}$$

$$p_{nm,t,\omega} = S_{base} \left[G_{nm} c_{nn,t,\omega} - G_{nm} c_{nm,t,\omega} + B_{nm} s_{nm,t,\omega} \right], \qquad \forall (n,m) \in \mathcal{L}, t, \omega \tag{B.18}$$

$$q_{nm,t,\omega} = S_{base} \left[(B_{nm} - b^{\text{cha}}_{nm}) c_{nn,t,\omega} - G_{nm} s_{nm,t,\omega} - B_{nm} c_{nm,t,\omega} \right], \qquad \forall (n,m) \in \mathcal{L}, t, \omega \tag{B.19}$$

$$c^2_{nm,t,\omega} + s^2_{nm,t,\omega} + \left(\frac{c_{nn,t,\omega} - c_{mm,t,\omega}}{2} \right)^2 \leq \left(\frac{c_{nn,t,\omega} + c_{mm,t,\omega}}{2} \right)^2, \qquad \forall (n,m) \in \mathcal{L}, t, \omega \tag{B.20}$$

$$c_{nm,t,\omega} = \quad c_{mn,t,\omega}, \qquad \forall (n,m) \in \mathcal{L}, t, \omega \tag{B.21}$$

$$s_{nm,t,\omega} = -s_{mn,t,\omega}, \qquad \forall (n,m) \in \mathcal{L}, t, \omega \tag{B.22}$$

$$\underline{V}^2_n \leq c_{nn,t,\omega} \leq \overline{V}^2_n, \qquad \forall n,t,\omega \tag{B.23}$$

$$\overline{F}^2_l \geq (B^2_{nm} + G^2_{nm}) \cdot (c_{nn,t,\omega} - 2c_{nm,t,\omega} + c_{mm,t,\omega}), \qquad \forall (n,m) \in \mathcal{L}, t, \omega \tag{B.24}$$

Model 10 Stochastic Distribution Unit Commitment [continued]

Constraints:

Generation Units:

$$0 \leq \phi^{\text{su}}_{g,t} \geq \Phi^{\text{su}}_{g}\big[z_{g,t} - z_{g,t-1}\big], \qquad \forall g,t \quad \text{(B.25)}$$

$$0 \leq \phi^{\text{sd}}_{g,t} \geq \Phi^{\text{sd}}_{g}\big[z_{g,t-1} - z_{g,t}\big], \qquad \forall g,t \quad \text{(B.26)}$$

$$p_{g,t} \leq p_{g,t-1} + \Delta_t z_{g,t} RU_g, \qquad \forall g,t \quad \text{(B.27)}$$

$$p_{g,t} \geq p_{g,t-1} - \Delta_t z_{g,t} RD_g, \qquad \forall g,t \quad \text{(B.28)}$$

$$z_{g,t}\underline{P}_g \leq p_{g,t} \leq z_{g,t}\overline{P}_g, \qquad \forall g,t \quad \text{(B.29)}$$

$$z_{g,t}\underline{Q}_g \leq q_{g,t} \leq z_{g,t}\overline{Q}_g, \qquad \forall g,t \quad \text{(B.30)}$$

Energy Storage:

$$e_{t,\omega} = e_{t-1,\omega} + p^{\text{batt}}_{t-1,\omega}\Delta_t, \qquad \forall t,\omega \quad \text{(B.31)}$$

$$p^{\text{batt}}_{t,\omega} = p^{\text{in}}_{t,\omega} - p^{\text{out}}_{t,\omega}, \qquad \forall t,\omega \quad \text{(B.32)}$$

$$p^{\text{out}}_{t,\omega} = \sum_j \widehat{P}^{\text{out}}_j x_{j,t,\omega}, \qquad \forall t,\omega \quad \text{(B.33)}$$

$$p^{\text{dis}}_{t,\omega} = \sum_j \widehat{P}^{\text{dis}}_j x_{j,t,\omega}, \qquad \forall t,\omega \quad \text{(B.34)}$$

$$p^{\text{in}}_{t,\omega} = \sum_k \widehat{P}^{\text{in}}_k y_{k,t,\omega}, \qquad \forall t,\omega \quad \text{(B.35)}$$

$$p^{\text{cha}}_{t,\omega} = \sum_k \widehat{P}^{\text{cha}}_k y_{k,t,\omega}, \qquad \forall t,\omega \quad \text{(B.36)}$$

$$SOC_{t,\omega} = \sum_j \widehat{SOC}_j x_{j,t,\omega} + \sum_k \widehat{SOC}_k y_{k,t,\omega}, \qquad \forall t,\omega \quad \text{(B.37)}$$

$$SOC_{t,\omega} = e_{t,\omega}/\overline{E}, \qquad \forall t,\omega \quad \text{(B.38)}$$

$$1 = \sum_j x_{j,t,\omega}, \qquad \forall t,\omega \quad \text{(B.39)}$$

$$1 = \sum_k y_{k,t,\omega}, \qquad \forall t,\omega \quad \text{(B.40)}$$

$$0 \leq x_{j,t,\omega}, \qquad \forall j,t,\omega \quad \text{(B.41)}$$

$$0 \leq y_{k,t,\omega}, \qquad \forall k,t,\omega. \quad \text{(B.42)}$$

Appendix C

Expected Cost Derivation: Asymmetric Node-to-Node Balancing

This appendix presents the derivation of the expected generation costs under the asymmetric node-to-node balancing policy presented in Chapter 4. Generator i's cost can be expressed in terms of nodal directional imbalances by

$$c_i(\boldsymbol{p}_i) = c_{2,i}(\boldsymbol{p}_i)^2 + c_{1,i}(\boldsymbol{p}_i) + c_{0,i}, \qquad \forall i \tag{C.1}$$

where

$$\boldsymbol{p}_i = p_i - \sum_u \left(\alpha_{iu}^- \boldsymbol{\omega}_u^- + \alpha_{iu}^+ \boldsymbol{\omega}_u^+\right), \qquad \forall i. \tag{C.1a}$$

Let the vectors $A_i = \left[\alpha_{i1}^-, ..., \alpha_{i|U|}^-, \alpha_{i1}^+, ..., \alpha_{i|U|}^+\right]^\top$, $\boldsymbol{\Omega} = \left[\boldsymbol{\omega}_1^-, ..., \boldsymbol{\omega}_{|U|}^-, \boldsymbol{\omega}_1^+, ..., \boldsymbol{\omega}_{|U|}^+\right]$, then the expected generation costs can be calculated as:

$$\begin{aligned} \mathbb{E}[c_i(\boldsymbol{p}_i)] &= \mathbb{E}[c_i(p_i - \boldsymbol{\Omega} \cdot A_i)] \\ &= c_i(p_i) + \mathbb{E}[\boldsymbol{Y}_{1,i}] + \mathbb{E}[\boldsymbol{Y}_{2,i}], \qquad \forall i \end{aligned} \tag{C.2}$$

where

$$\boldsymbol{Y}_{1,i} = -(2c_{2,i}p_i + c_{1,i})\boldsymbol{X}_i, \qquad \forall i \tag{C.2a}$$

$$\boldsymbol{Y}_{2,i} = c_{2,i}(\boldsymbol{X}_i)^2, \qquad \forall i \tag{C.2b}$$

$$\boldsymbol{X}_i = \boldsymbol{\Omega} \cdot A_i, \qquad \forall i. \tag{C.2c}$$

Let $\mathbb{E}[\boldsymbol{\Omega}]{=}M$, and since for a random variable $\boldsymbol{Z}$, $\mathbb{E}\left[\boldsymbol{Z}^2\right]{=}\mathrm{Var}(\boldsymbol{Z}) + \mathbb{E}[\boldsymbol{Z}]^2$:

$$\mathbb{E}[\boldsymbol{Y}_{1,i}] = -(2c_{2,i}p_i + c_{1,i})(M \cdot A_i), \qquad \forall i \tag{C.3a}$$

$$\mathbb{E}[\boldsymbol{Y}_{2,i}] = c_{2,i}\big((M \cdot A_i)^2{+}\mathrm{var}[\boldsymbol{\Omega} \cdot A_i]\big), \qquad \forall i. \tag{C.3b}$$

The variance of a linear combination can be calculated by

$$\mathrm{var}\left[\sum_n (b_n \boldsymbol{Z}_n)\right] = \sum_{n,m}^{N} [b_n b_m \mathrm{cov}(\boldsymbol{Z}_n \boldsymbol{Z}_m)], \tag{C.4}$$

where b_n is a scalar and $\boldsymbol{Z}_n$ a random variable.

Let $\Sigma{=}\mathrm{Var}[\boldsymbol{\Omega}]$ be the non-trivial covariance matrix of the forecast errors, we can then rewrite (C.3b) using (C.4) as

$$\mathbb{E}[\boldsymbol{Y}_{2,i}] = c_{2,i}\left[(M \cdot A_i)^2{+}\left\|A_i\Sigma^{1/2}\right\|_2^2\right], \qquad \forall i. \tag{C.5}$$

Finally, by using expression (C.2) the expected costs are

$$\mathbb{E}[c_i(\boldsymbol{p}_i)] = c_i(p_i) - (2c_{2,i}p_i{+}c_{1,i})(M \cdot A_i) + c_{2,i}\left[(M{\cdot}A_i)^2{+}\left\|A_i\Sigma^{1/2}\right\|_2^2\right], \quad \forall i. \tag{C.6}$$

Bibliography

[1] Emil Hillberg, Antony Zegers, Barbara Herndler, Steven Wong, Jean Pompee, Jean-Yves Bourmaud, Sebastian Lehnhoff, Gianluigi Migliavacca, Kjetil Uhlen, Irina Oleinikova, Hjalmar Pihl, Markus Norström, Mattias Persson, Joni Rossi, and Giovanni Beccuti, "Flexibility needs in the future power system," International Smart Grid Action Network (ISGAN), Tech. Rep., Mar. 2019.

[2] ETIP SNET, "VISION 2050 - Integrating Smart Networks for the Energy Transition: Serving Society and Protecting the Environment," European Technology and Innovation Platform for Smart Networks for the Energy Transition (ETIP SNET), Tech. Rep., Jun. 2018.

[3] "Chair's Summary for IEA Clean Energy Transitions Summit - News," https://www.iea.org/news/chair-s-summary-for-iea-clean-energy-transitions-summit.

[4] IEA, "Projected Costs of Generating Electricity 2020," International Energy Agency (IEA), Paris, Tech. Rep., 2020.

[5] IEA, "Renewables 2020," International Energy Agency (IEA), Paris, Tech. Rep., 2020.

[6] IRENA, "Renewable capacity statistics 2021," International Renewable Energy Agency (IRENA), Abu Dhabi, Tech. Rep., 2021.

[7] International Energy Agency, *Empowering Variable Renewables – Options for Flexible Electricity Systems*. OECD, Oct. 2009.

[8] M. I. Alizadeh, M. Parsa Moghaddam, N. Amjady, P. Siano, and M. K. Sheikh-El-Eslami, "Flexibility in future power systems with high renewable penetration: A review," *Renewable and Sustainable Energy Reviews*, vol. 57, pp. 1186–1193, May 2016.

[9] G. Chicco, S. Riaz, A. Mazza, and P. Mancarella, "Flexibility From Distributed Multienergy Systems," *Proceedings of the IEEE*, vol. 108, no. 9, pp. 1496–1517, Sep. 2020.

[10] International Energy Agency, *Harnessing Variable Renewables: A Guide to the Balancing Challenge*. OECD, May 2011.

[11] R. Billinton and R. N. Allan, "Power-system reliability in perspective," *Electronics and Power*, vol. 30, no. 3, pp. 231–236, Mar. 1984.

[12] IRENA, "Innovation landscape brief: Flexibility in conventional power plants," International Renewable Energy Agency (IRENA), Abu Dhabi, Tech. Rep., 2019.

[13] NERC, "Flexibility Requirements and Metrics for Variable Generation: Implications for System Planning Studies," North American Electric Reliability Corporation (NERC), Princeton, NJ, Tech. Rep., Aug-2010.

[14] L. M. Abadie, "Operating flexibility at power plants: A market valuation," *International Journal of Electrical Power & Energy Systems*, vol. 64, pp. 41–49, Jan. 2015.

[15] M. F. Anjos and A. J. Conejo, "Unit Commitment in Electric Energy Systems," *Foundations and Trends in Electric Energy Systems*, vol. 1, no. 4, pp. 220–310, 2017.

[16] L. M. Abadie and J. M. Chamorro, "Valuing flexibility: The case of an Integrated Gasification Combined Cycle power plant," *Energy Economics*, vol. 30, no. 4, pp. 1850–1881, Jul. 2008.

[17] S. Rahm, J. Goldmeer, M. Moliere, and A. Eranki, "GER-4601- Addressing Gas Turbine Fuel Flexibility," in *POWER-GEN Middle East*, Manama, Bahrain, Feb. 2009, p. 14.

[18] E. Lannoye, D. Flynn, and M. O'Malley, "Evaluation of Power System Flexibility," *IEEE Transactions on Power Systems*, vol. 27, no. 2, pp. 922–931, May 2012.

[19] R. Wiltshire, *Advanced District Heating and Cooling (DHC) Systems*, 1st ed. Woodhead Publishing, 2016.

[20] P. D. Lund, J. Lindgren, J. Mikkola, and J. Salpakari, "Review of energy system flexibility measures to enable high levels of variable renewable electricity," *Renewable and Sustainable Energy Reviews*, vol. 45, pp. 785–807, 2015.

[21] K. Uddin, M. Dubarry, and M. B. Glick, "The viability of vehicle-to-grid operations from a battery technology and policy perspective," *Energy Policy*, vol. 113, no. August 2017, pp. 342–347, Feb. 2018.

[22] R. G. Junker, A. G. Azar, R. A. Lopes, K. B. Lindberg, G. Reynders, R. Relan, and H. Madsen, "Characterizing the energy flexibility of buildings and districts," *Applied Energy*, vol. 225, pp. 175–182, Sep. 2018.

[23] M. Tschampion, M. A. Bucher, A. Ulbig, and G. Andersson, "N-1 security assessment incorporating the flexibility offered by dynamic line rating," in *2016 Power Systems Computation Conference (PSCC)*, Jun. 2016, pp. 1–7.

[24] X.-P. Zhang, C. Rehtanz, and B. Pal, *Flexible AC Transmission Systems: Modelling and Control*, ser. Power Systems. Berlin, Heidelberg: Springer Berlin Heidelberg, 2012.

[25] K. W. Hedman, S. S. Oren, and R. P. O'Neill, "Flexible Transmission in the Smart Grid: Optimal Transmission Switching," in *Handbook of Networks in Power Systems I*, A. Sorokin, S. Rebennack, P. M. Pardalos, N. A. Iliadis, and M. V. F. Pereira, Eds. Berlin, Heidelberg: Springer Berlin Heidelberg, 2012, pp. 523–553.

[26] G. L. Doorman and R. van der Veen, "An analysis of design options for markets for cross-border balancing of electricity," *Utilities Policy*, vol. 27, pp. 39–48, Dec. 2013.

[27] "ENTSO-E Market report 2021," European association for the cooperation of transmission system operators (TSOs) for electricity (ENTSO-E), Tech. Rep., Jun. 2021.

[28] M. Geidl, G. Koeppel, P. Favre-Perrod, B. Klockl, G. Andersson, and K. Frohlich, "Energy hubs for the future," *IEEE Power and Energy Magazine*, vol. 5, no. 1, pp. 24–30, Jan. 2007.

[29] A. Vandermeulen, B. van der Heijde, and L. Helsen, "Controlling district heating and cooling networks to unlock flexibility: A review," *Energy*, vol. 151, pp. 103–115, May 2018.

[30] S. Clegg and P. Mancarella, "Storing renewables in the gas network: Modelling of power-to-gas seasonal storage flexibility in low-carbon power systems," *Transmission Distribution IET Generation*, vol. 10, no. 3, pp. 566–575, 2016.

[31] M. Farrokhifar, Y. Nie, and D. Pozo, "Energy systems planning: A survey on models for integrated power and natural gas networks coordination," *Applied Energy*, vol. 262, p. 114567, Mar. 2020.

[32] H. Blanco, W. Nijs, J. Ruf, and A. Faaij, "Potential for hydrogen and Power-to-Liquid in a low-carbon EU energy system using cost optimization," *Applied Energy*, vol. 232, pp. 617–639, Dec. 2018.

[33] IRENA, "Innovation landscape brief: Redesigning capacity markets," International Renewable Energy Agency (IRENA), Abu Dhabi, Tech. Rep., 2019.

[34] X. Zhang, J.-X. Wang, Z. Cao, S. Shen, S. Meng, and J.-L. Fan, "What is driving the remarkable decline of wind and solar power curtailment in China? evidence from China and four typical provinces," *Renewable Energy*, vol. 174, pp. 31–42, Aug. 2021.

[35] Y. V. Makarov, C. Loutan, J. Ma, and P. de Mello, "Operational Impacts of Wind Generation on California Power Systems," *IEEE Transactions on Power Systems*, vol. 24, no. 2, pp. 1039–1050, May 2009.

[36] A. Ulbig and G. Andersson, "Analyzing operational flexibility of electric power systems," *International Journal of Electrical Power & Energy Systems*, vol. 72, pp. 155–164, Nov. 2015.

[37] F. Wu and S. Kumagai, "Steady-State Security Regions of Power Systems," *IEEE Transactions on Circuits and Systems*, vol. 29, no. 11, pp. 703–711, Nov. 1982.

[38] A. A. Khodadoost Arani, G. B. Gharehpetian, and M. Abedi, "Review on Energy Storage Systems Control Methods in Microgrids," *International Journal of Electrical Power & Energy Systems*, vol. 107, pp. 745–757, May 2019.

[39] A. Dehghani-Sanij, E. Tharumalingam, M. Dusseault, and R. Fraser, "Study of energy storage systems and environmental challenges of batteries," *Renewable and Sustainable Energy Reviews*, vol. 104, pp. 192–208, Apr. 2019.

[40] D. Álvaro, R. Arranz, and J. A. Aguado, "Sizing and operation of hybrid energy storage systems to perform ramp-rate control in PV power plants," *International Journal of Electrical Power & Energy Systems*, vol. 107, pp. 589–596, May 2019.

[41] C. Jayamaha, A. Costabeber, A. Williams, and M. Sumner, "An independently controlled energy storage to support short term frequency fluctuations in weak electrical grids," *International Journal of Electrical Power & Energy Systems*, vol. 103, pp. 562–576, Dec. 2018.

[42] H. Yang, Y. Zhang, Y. Ma, M. Zhou, and X. Yang, "Reliability evaluation of power systems in the presence of energy storage system as demand management resource," *International Journal of Electrical Power & Energy Systems*, vol. 110, pp. 1–10, Sep. 2019.

[43] T. Dragicevic, X. Lu, J. C. Vasquez, and J. M. Guerrero, "DC Microgrids—Part II: A Review of Power Architectures, Applications, and Standardization Issues," *IEEE Transactions on Power Electronics*, vol. 31, no. 5, pp. 3528–3549, May 2016.

[44] A. Escalera, M. Prodanović, and E. D. Castronuovo, "Analytical methodology for reliability assessment of distribution networks with energy storage in islanded and emergency-tie restoration modes," *International Journal of Electrical Power & Energy Systems*, vol. 107, pp. 735–744, May 2019.

[45] Y. Zhang, X. Han, B. Xu, M. Wang, P. Ye, and Y. Pei, "Risk–Based Admissibility Analysis of Wind Power Integration into Power System With Energy Storage System," *IEEE Access*, vol. 6, pp. 57 400–57 413, 2018.

[46] W. J. Cole and A. Frazier, "Cost Projections for Utility-Scale Battery Storage," National Renewable Energy Laboratory, Golden, CO, Tech. Rep. NREL/TP-6A20-73222, 1529218, Jun. 2019.

[47] A. Azzuni and C. Breyer, "Energy security and energy storage technologies," *Energy Procedia*, vol. 155, pp. 237–258, Nov. 2018.

[48] A. Sakti, K. G. Gallagher, N. Sepulveda, C. Uckun, C. Vergara, F. J. de Sisternes, D. W. Dees, and A. Botterud, "Enhanced representations of lithium-ion batteries in power systems models and their effect on the valuation of energy arbitrage applications," *Journal of Power Sources*, vol. 342, pp. 279–291, 2017.

[49] P. Mancarella, "MES (multi-energy systems): An overview of concepts and evaluation models," *Energy*, vol. 65, pp. 1–17, Feb. 2014.

[50] H. Averfalk, P. Ingvarsson, U. Persson, M. Gong, and S. Werner, "Large heat pumps in Swedish district heating systems," *Renewable and Sustainable Energy Reviews*, vol. 79, pp. 1275–1284, Nov. 2017.

[51] E. Guelpa, A. Bischi, V. Verda, M. Chertkov, and H. Lund, "Towards future infrastructures for sustainable multi-energy systems: A review," *Energy*, vol. 184, pp. 2–21, Oct. 2019.

[52] E. Guelpa, G. Barbero, A. Sciacovelli, and V. Verda, "Peak-shaving in district heating systems through optimal management of the thermal request of buildings," *Energy*, vol. 137, pp. 706–714, Oct. 2017.

[53] L. Mitridati, J. Kazempour, and P. Pinson, "Heat and electricity market coordination: A scalable complementarity approach," *European Journal of Operational Research*, vol. 283, no. 3, pp. 1107–1123, Jun. 2020.

[54] Y. Cao, W. Wei, L. Wu, S. Mei, M. Shahidehpour, and Z. Li, "Decentralized Operation of Interdependent Power Distribution Network and District Heating Network: A Market-Driven Approach," *IEEE Transactions on Smart Grid*, vol. 10, no. 5, pp. 5374–5385, Sep. 2019.

[55] Y. Chen, W. Wei, F. Liu, E. E. Sauma, and S. Mei, "Energy Trading and Market Equilibrium in Integrated Heat-Power Distribution Systems," *IEEE Transactions on Smart Grid*, vol. 10, no. 4, pp. 4080–4094, Jul. 2019.

[56] A. Schwele, A. Arrigo, C. Vervaeren, J. Kazempour, and F. Vallée, "Coordination of Electricity, Heat, and Natural Gas Systems Accounting for Network Flexibility," in *Proceedings of Power Systems Computation Conference*, 2020.

[57] L. Deng, Z. Li, H. Sun, Q. Guo, Y. Xu, R. Chen, J. Wang, and Y. Guo, "Generalized Locational Marginal Pricing in a Heat-and-Electricity-Integrated Market," *IEEE Transactions on Smart Grid*, vol. 10, no. 6, pp. 6414–6425, Nov. 2019.

[58] N. Nikmehr, "Distributed robust operational optimization of networked microgrids embedded interconnected energy hubs," *Energy*, vol. 199, p. 117440, May 2020.

[59] S.-L. Cheng, C.-T. Chang, and D. Jiang, "A game-theory based optimization strategy to configure inter-plant heat integration schemes," *Chemical Engineering Science*, vol. 118, pp. 60–73, Oct. 2014.

[60] C. Chang, Y. Wang, J. Ma, X. Chen, and X. Feng, "An energy hub approach for direct interplant heat integration," *Energy*, vol. 159, pp. 878–890, Sep. 2018.

[61] H. Bütün, I. Kantor, and F. Maréchal, "Incorporating Location Aspects in Process Integration Methodology," *Energies*, vol. 12, no. 17, p. 3338, Aug. 2019.

[62] Y. Dvorkin, D. S. Kirschen, and M. A. Ortega-Vazquez, "Assessing flexibility requirements in power systems," *IET Generation, Transmission & Distribution*, vol. 8, no. 11, pp. 1820–1830, Nov. 2014.

[63] J. Arroyo and F. Galiana, "Energy and reserve pricing in security and network-constrained electricity markets," *IEEE Transactions on Power Systems*, vol. 20, no. 2, pp. 634–643, May 2005.

[64] Giorgia Oggioni and Cristian Lanfranconi, "Empirics of Intraday and Real-time Markets in Europe: Italy," DIW - Deutsches Institut für Wirtschaftsforschung, Berlin, Germany, Tech. Rep., 2015.

[65] Management National Dispatch Centre, Operation Planning Directorate, and XM, "Requirements for the Provision of the Secondary Frequency Regulation Service - AGC," Management National Dispatch Centre, Tech. Rep., Jul. 2010.

[66] B. A. Frew, M. Milligan, G. Brinkman, A. Bloom, K. Clark, and P. Denholm, "Revenue Sufficiency and Reliability in a Zero Marginal Cost Future," in *15th International Workshop on Large-Scale Integration of Wind Power into Power Systems as Well as on Transmission Networks for Offshore Wind Power Plants*, Vienna, Austria, Nov. 2016.

[67] A. Papavasiliou, S. S. Oren, and R. P. O'Neill, "Reserve requirements for wind power integration: A scenario-based stochastic programming framework," *IEEE Trans. Pwr. Sys.*, vol. 26, no. 4, pp. 2197–2206, 2011.

[68] H. Ye, Y. Ge, M. Shahidehpour, and Z. Li, "Uncertainty marginal price, transmission reserve, and day-ahead market clearing with robust unit commitment," *IEEE Trans. Pwr. Sys.*, vol. 32, no. 3, pp. 1782–1795, 2017.

[69] Y. Dvorkin, "A Chance-Constrained Stochastic Electricity Market," *IEEE Transactions on Power Systems*, vol. 35, no. 4, pp. 2993–3003, Jul. 2020.

[70] D. Bienstock, M. Chertkov, and S. Harnett, "Chance-Constrained Optimal Power Flow: Risk-Aware Network Control under Uncertainty," *SIAM Review*, vol. 56, no. 3, pp. 461–495, Jan. 2014.

[71] M. Lubin and I. Dunning, "Computing in Operations Research Using Julia," *INFORMS Journal on Computing*, vol. 27, no. 2, pp. 238–248, Apr. 2015.

[72] Y. Dvorkin, M. Lubin, S. Backhaus, and M. Chertkov, "Uncertainty Sets for Wind Power Generation," *IEEE Transactions on Power Systems*, vol. 31, no. 4, pp. 3326–3327, Jul. 2016.

[73] S. E. Haupt, M. Garcia Casado, M. Davidson, J. Dobschinski, P. Du, M. Lange, T. Miller, C. Mohrlen, A. Motley, R. Pestana, and J. Zack, "The Use of Probabilistic Forecasts: Applying Them in Theory and Practice," *IEEE Power and Energy Magazine*, vol. 17, no. 6, pp. 46–57, Nov. 2019.

[74] A. Gonzalez-Castellanos, D. Pozo, and A. Bischi, "Non-Ideal Linear Operation Model for Li-Ion Batteries," *IEEE Transactions on Power Systems*, vol. 35, no. 1, pp. 672–682, Jan. 2020.

[75] A. González-Castellanos, D. Pozo, and A. Bischi, "Distribution System Operation with Energy Storage and Renewable Generation Uncertainty," in *Handbook of Optimization in Electric Power Distribution Systems*, M. Resener, S. Rebennack, P. M. Pardalos, and S. Haffner, Eds. Cham: Springer International Publishing, 2020, pp. 183–218.

[76] A. Berrueta, A. Urtasun, A. Ursúa, and P. Sanchis, "A comprehensive model for lithium-ion batteries: From the physical principles to an electrical model," *Energy*, vol. 144, pp. 286–300, 2018.

[77] D. Pozo, J. Contreras, and E. Sauma, "Unit Commitment With Ideal and Generic Energy Storage Units," *IEEE Transactions on Power Systems*, vol. 29, no. 6, pp. 2974–2984, Nov. 2014.

[78] M. Schimpe, M. Naumann, N. Truong, H. C. Hesse, S. Santhanagopalan, A. Saxon, and A. Jossen, "Energy efficiency evaluation of a stationary lithium-ion battery container storage system via electro-thermal modeling and detailed component analysis," *Applied Energy*, vol. 210, no. October 2017, pp. 211–229, 2018.

[79] Terna S.p.A., "Public report year 2016: Pilot projects and testing of energy storage on energy-intensive batteries," Terna S.p.A., Tech. Rep., Jul. 2017.

[80] H. Lund, P. A. Østergaard, D. Connolly, I. Ridjan, B. V. Mathiesen, F. Hvelplund, J. Z. Thellufsen, and P. Sorknæs, "Energy storage and smart energy systems," *International Journal of Sustainable Energy Planning and Management*, vol. 11, pp. 3–14, 2016.

[81] R. L. Fares and M. E. Webber, "A flexible model for economic operational management of grid battery energy storage," *Energy*, vol. 78, pp. 768–776, 2014.

[82] N. Günter and A. Marinopoulos, "Energy storage for grid services and applications : Classification , market review , metrics , and methodology for evaluation of deployment cases," *Journal of Energy Storage*, vol. 8, pp. 226–234, 2016.

[83] R. D. Rappaport and J. Miles, "Cloud energy storage for grid scale applications in the UK," *Energy Policy*, vol. 109, pp. 609–622, Oct. 2017.

[84] A. Rodríguez and G. L. Plett, "Controls-oriented models of lithium-ion cells having blend electrodes. Part 2: Physics-based reduced-order models," *Journal of Energy Storage*, vol. 11, pp. 219–236, Jun. 2017.

[85] D. Ali, S. Mukhopadhyay, H. Rehman, and A. Khurram, "UAS based Li-ion battery model parameters estimation," *Control Engineering Practice*, vol. 66, pp. 126–145, Sep. 2017.

[86] S. I. Vagropoulos and A. G. Bakirtzis, "Optimal Bidding Strategy for Electric Vehicle Aggregators in Electricity Markets," *IEEE Transactions on Power Systems*, vol. 28, no. 4, pp. 4031–4041, Nov. 2013.

[87] H. Pandžić and V. Bobanac, "An Accurate Charging Model of Battery Energy Storage," *IEEE Transactions on Power Systems*, vol. 34, no. 2, pp. 1416–1426, Mar. 2019.

[88] Y. Wang, X. Lin, and M. Pedram, "A Near-Optimal Model-Based Control Algorithm for Households Equipped With Residential Photovoltaic Power Generation and Energy Storage Systems," *IEEE Transactions on Sustainable Energy*, vol. 7, no. 1, pp. 77–86, Jan. 2016.

[89] T. Morstyn, B. Hredzak, R. P. Aguilera, and V. G. Agelidis, "Model Predictive Control for Distributed Microgrid Battery Energy Storage Systems," *IEEE Transactions on Control Systems Technology*, vol. 26, no. 3, pp. 1107–1114, May 2018.

[90] M. Rampazzo, M. Luvisotto, N. Tomasone, I. Fastelli, and M. Schiavetti, "Modelling and simulation of a Li-ion energy storage system: Case study from the island of Ventotene in the Tyrrhenian Sea," *Journal of Energy Storage*, vol. 15, pp. 57–68, 2018.

[91] M. Astaneh, R. Dufo-López, R. Roshandel, F. Golzar, and J. L. Bernal-Agustín, "A computationally efficient Li-ion electrochemical battery model for long-term analysis of stand-alone renewable energy systems," *Journal of Energy Storage*, vol. 17, pp. 93–101, Jun. 2018.

[92] T. Dong, P. Peng, and F. Jiang, "Numerical modeling and analysis of the thermal behavior of NCM lithium-ion batteries subjected to very high C-rate discharge/charge operations," *International Journal of Heat and Mass Transfer*, vol. 117, pp. 261–272, Feb. 2018.

[93] C. D'Ambrosio, A. Lodi, and S. Martello, "Piecewise linear approximation of functions of two variables in MILP models," *Operations Research Letters*, vol. 38, no. 1, pp. 39–46, Jan. 2010.

[94] Probability Methods Subcommittee, "IEEE reliability test system," *IEEE Transactions on Power Apparatus and Systems*, vol. PAS-98, no. 6, pp. 2047–2054, Nov. 1979.

[95] A. Gonzalez-Castellanos, D. Pozo, and A. Bischi, "Data for: A detailed Li-ion battery operation model," Oct. 2018.

[96] Red Eléctrica de España, "Electricity demand tracking in real time, associated generation mix and CO2 emissions for 06/20/2018," https://demanda.ree.es/visiona/peninsula/demanda/total/2018-06-20.

[97] Bezanson, J., Edelman, A., Karpinski, S., and Shah, V.B., "Julia: A Fresh Approach to Numerical Computing," *SIAM Review*, vol. 59, no. 1, pp. 65–98, Jan. 2017.

[98] Gurobi Optimization Inc., "Gurobi Optimization: The state-of-the-art mathematical programming solver," http://www.gurobi.com/.

[99] A. Wächter and L. T. Biegler, "On the implementation of an interior-point filter line-search algorithm," *Math. Prog.*, vol. 106, no. 1, 2006.

[100] M. Baran and F. Wu, "Network reconfiguration in distribution systems for loss reduction and load balancing," *IEEE Transactions on Power Delivery*, vol. 4, no. 2, pp. 1401–1407, Apr. 1989.

[101] A. Gonzalez-Castellanos, D. Pozo, and A. Bischi, "Online appendix for book chapter: Distribution System Operation with Energy Storage and Renewable Generation Uncertainty," *Zenodo*, Jan. 2019.

[102] NOAA Earth System Research Laboratory, "ESRL Global Monitoring Division - GRAD - Surface Radiation Budget Network (SURFRAD)," https://www.esrl.noaa.gov/gmd/grad/surfrad/dataplot.html.

[103] K. Antoniadou-Plytaria, D. Steen, L. A. Tuan, O. Carlson, and M. A. F. Ghazvini, "Market-Based Energy Management Model of a Building Microgrid Considering Battery Degradation," *IEEE Transactions on Smart Grid*, vol. 12, no. 2, pp. 1794–1804, Mar. 2021.

[104] H. Lund, S. Werner, R. Wiltshire, S. Svendsen, J. E. Thorsen, F. Hvelplund, and B. V. Mathiesen, "4th Generation District Heating (4GDH): Integrating smart thermal grids into future sustainable energy systems," *Energy*, vol. 68, pp. 1–11, Apr. 2014.

[105] A. Sandoff and J. Williamsson, "Business models for district heating," in *Advanced District Heating and Cooling (DHC) Systems*. Elsevier, 2016, pp. 293–317.

[106] M. Ancona, L. Branchini, A. De Pascale, and F. Melino, "Smart District Heating: Distributed Generation Systems' Effects on the Network," *Energy Procedia*, vol. 75, pp. 1208–1213, Aug. 2015.

[107] A. Maroufmashat, A. Elkamel, M. Fowler, S. Sattari, R. Roshandel, A. Hajimiragha, S. Walker, and E. Entchev, "Modeling and optimization of a network of energy hubs to improve economic and emission considerations," *Energy*, vol. 93, pp. 2546–2558, Dec. 2015.

[108] S. T. Taqvi, A. Maroufmashat, M. Fowler, A. Elkamel, and S. S. Khavas, "Optimal Design, Operation, and Planning of Distributed Energy Systems Through the Multi-Energy Hub Network Approach," in *Operation, Planning, and Analysis of Energy Storage Systems in Smart Energy Hubs*, B. Mohammadi-Ivatloo and F. Jabari, Eds. Cham: Springer International Publishing, 2018, pp. 365–389.

[109] C. Zhang, M. Ahmad, and Y. Wang, "ADMM Based Privacy-Preserving Decentralized Optimization," *IEEE Transactions on Information Forensics and Security*, vol. 14, no. 3, pp. 565–580, Mar. 2019.

[110] C. Lin, W. Wu, B. Zhang, and Y. Sun, "Decentralized Solution for Combined Heat and Power Dispatch Through Benders Decomposition," *IEEE Transactions on Sustainable Energy*, vol. 8, no. 4, pp. 1361–1372, Oct. 2017.

[111] T. Lu, Q. Ai, and Z. Wang, "Interactive game vector: A stochastic operation-based pricing mechanism for smart energy systems with coupled-microgrids," *Applied Energy*, vol. 212, pp. 1462–1475, Feb. 2018.

[112] T. Liu, X. Tan, B. Sun, Y. Wu, and D. H. Tsang, "Energy management of cooperative microgrids: A distributed optimization approach," *International Journal of Electrical Power & Energy Systems*, vol. 96, pp. 335–346, Mar. 2018.

[113] A. Fernandez Pales, J. Dulac, K. West, and M. LaFrance, *Linking Heat and Electricity Systems*. Paris: International Energy Agency, 2014.

[114] R. Sioshansi and A. J. Conejo, *Optimization in Engineering*, ser. Springer Optimization and Its Applications. Cham: Springer International Publishing, 2017, vol. 120.

[115] B. van der Heijde, A. Aertgeerts, and L. Helsen, "Modelling steady-state thermal behaviour of double thermal network pipes," *International Journal of Thermal Sciences*, vol. 117, pp. 316–327, Jul. 2017.

[116] S. Boyd, "Distributed Optimization and Statistical Learning via the Alternating Direction Method of Multipliers," *Foundations and Trends in Machine Learning*, vol. 3, no. 1, pp. 1–122, 2010.

[117] R. Glowinski and A. Marroco, "Sur l'approximation, par éléments finis d'ordre un, et la résolution, par pénalisation-dualité d'une classe de problèmes de Dirichlet non linéaires," *ESAIM: Mathematical Modelling and Numerical Analysis - Modélisation Mathématique et Analyse Numérique*, vol. 9, no. R2, pp. 41–76, 1975.

[118] D. Gabay and B. Mercier, "A dual algorithm for the solution of nonlinear variational problems via finite element approximation," *Computers & Mathematics with Applications*, vol. 2, no. 1, pp. 17–40, 1976.

[119] C. Chen, B. He, Y. Ye, and X. Yuan, "The direct extension of ADMM for multi-block convex minimization problems is not necessarily convergent," *Mathematical Programming*, vol. 155, no. 1-2, pp. 57–79, Jan. 2016.

[120] W. Deng, M.-J. Lai, Z. Peng, and W. Yin, "Parallel Multi-Block ADMM with o(1 / k) Convergence," *Journal of Scientific Computing*, vol. 71, no. 2, pp. 712–736, May 2017.

[121] T. Guo, M. I. Henwood, and M. van Ooijen, "An algorithm for combined heat and power economic dispatch," *IEEE Transactions on Power Systems*, vol. 11, no. 4, pp. 1778–1784, Nov. 1996.

[122] A. Rabiee and M. Moradi-dalvand, "Combined Heat and Power System Operation Cost Minimization using Frog Leaping Based Intelligent Search Algorithm," *Journal of Energy Management and Technology*, vol. 1, no. 3, Dec. 2017.

[123] J. Bezanson, A. Edelman, S. Karpinski, and V. B. Shah, "Julia: A Fresh Approach to Numerical Computing," *SIAM Review*, vol. 59, no. 1, pp. 65–98, Jan. 2017.

[124] I. Dunning, J. Huchette, and M. Lubin, "JuMP: A Modeling Language for Mathematical Optimization," *SIAM Review*, vol. 59, no. 2, pp. 295–320, Jan. 2017.

[125] B. F. Hobbs and S. S. Oren, "Three waves of U.S. reforms: Following the path of wholesale electricity market restructuring," *IEEE Power and Energy Magazine*, vol. 17, no. 1, pp. 73–81, Jan. 2019.

[126] M. Lubin, Y. Dvorkin, and S. Backhaus, "A robust approach to chance constrained optimal power flow with renewable generation," *IEEE Trans. Pwr. Sys.*, vol. 31, no. 5, pp. 3840–3849, 2016.

[127] S. Wong and J. D. Fuller, "Pricing energy and reserves using stochastic optimization in an alternative electricity market," *IEEE Trans. Pwr. Sys.*, vol. 22, no. 2, pp. 631–638, 2007.

[128] G. Pritchard, G. Zakeri, and A. Philpott, "A single-settlement, energy-only electric power market for unpredictable and intermittent participants," *Operations research*, vol. 58, no. 4-part-2, pp. 1210–1219, 2010.

[129] J. M. Morales, A. J. Conejo, K. Liu, and J. Zhong, "Pricing electricity in pools with wind producers," *IEEE Trans. Pwr. Sys.*, vol. 27, no. 3, pp. 1366–1376, 2012.

[130] J. Kazempour, P. Pinson, and B. F. Hobbs, "A stochastic market design with revenue adequacy and cost recovery by scenario: Benefits and costs," *IEEE Trans. Pwr. Sys.*, vol. 33, no. 4, pp. 3531–3545, 2018.

[131] X. Kuang, Y. Dvorkin, A. J. Lamadrid, M. A. Ortega-Vazquez, and L. F. Zuluaga, "Pricing Chance Constraints in Electricity Markets," *IEEE Transactions on Power Systems*, vol. 33, no. 4, pp. 4634–4636, Jul. 2018.

[132] Y. Dvorkin, "A chance-constrained stochastic electricity market," *IEEE Transactions on Power Systems*, vol. 35, no. 4, pp. 2993–3003, 2019.

[133] R. Mieth and Y. Dvorkin, "Distribution Electricity Pricing under Uncertainty," *IEEE Transactions on Power Systems*, vol. 35, no. 3, pp. 2325–2338, May 2020.

[134] R. Mieth, J. Kim, and Y. Dvorkin, "Risk- and variance-aware electricity pricing," *Electric Power Systems Research*, vol. 189, p. 106804, Dec. 2020.

[135] A. Ratha, J. Kazempour, A. Virag, and P. Pinson, "Exploring market properties of policy-based reserve procurement for power systems," in *58th IEEE Conference on Decision and Control*. IEEE, 2019.

[136] D. S. Kirschen and G. Strbac, *Fundamentals of Power System Economics*, 2nd ed. Hoboken: Wiley, Jul. 2018.

[137] A. J. Conejo, M. Carrión, J. M. Morales *et al.*, *Decision Making under Uncertainty in Electricity Markets*. Springer, 2010, vol. 1.

[138] L. Roald, F. Oldewurtel, T. Krause, and G. Andersson, "Analytical reformulation of security constrained optimal power flow with probabilistic constraints," in *2013 IEEE Grenoble Conference*. IEEE, 2013, pp. 1–6.

[139] W. Xie and S. Ahmed, "Distributionally Robust Chance Constrained Optimal Power Flow with Renewables: A Conic Reformulation," *IEEE Transactions on Power Systems*, vol. 33, no. 2, pp. 1860–1867, Mar. 2018.

[140] L. Roald, S. Misra, T. Krause, and G. Andersson, "Corrective Control to Handle Forecast Uncertainty: A Chance Constrained Optimal Power Flow," *IEEE Transactions on Power Systems*, vol. 32, no. 2, pp. 1626–1637, Mar. 2017.

[141] X. Fang, B.-M. Hodge, E. Du, C. Kang, and F. Li, "Introducing Uncertainty Components in Locational Marginal Prices for Pricing Wind Power and Load Uncertainties," *IEEE Transactions on Power Systems*, vol. 34, no. 3, pp. 2013–2024, May 2019.

[142] M. Chertkov and Y. Dvorkin, "Chance constrained optimal power flow with primary frequency response," in *2017 IEEE 56th Annual Conference on Decision and Control (CDC)*. IEEE, 2017, pp. 4484–4489.

[143] D. Bienstock and A. Shukla, "Variance-Aware Optimal Power Flow," in *2018 Power Systems Computation Conference (PSCC)*. Dublin, Ireland: IEEE, Jun. 2018, pp. 1–8.

[144] MOSEK ApS, "Mosek.jl," https://github.com/MOSEK/Mosek.jl, 2021.

[145] Anton Hinneck, "Code Supplement - ReservePricing," https://github.com/antonhinneck/ReservePricing, Mar. 2021.

[146] "Generation Forecasts for Wind and Solar," https://transparency.entsoe.eu/, 2021.

[147] A. Gonzalez-Castellanos, D. Pozo, and A. Bischi, "Stochastic Unit Commitment of a Distribution Network with Non-ideal Energy Storage," in *2019 International Conference on Smart Energy Systems and Technologies (SEST)*. Porto, Portugal: IEEE, Sep. 2019, pp. 1–6.